Technical University of Denmark

DTU

Coupled Photonic Crystal Cavity Array Laser

Schubert, Martin; Yvind, Kresten; Hvam, Jørn Marcher; Frandsen, Lars Hagedorn

Publication date:
2011

Document Version
Publisher's PDF, also known as Version of record

Link back to DTU Orbit

Citation (APA):
Schubert, M., Yvind, K., Hvam, J. M., & Frandsen, L. H. (2011). Coupled Photonic Crystal Cavity Array Laser. Kgs. Lyngby, Denmark: Technical University of Denmark (DTU).

DTU Library
Technical Information Center of Denmark

Coupled Photonic Crystal Cavity Array Laser

A dissertation
submitted to the Department of Photonics Engineering
at the Technical University of Denmark

Martin Schubert
September 2010

Acknowledgements

I hope that she will read this at some point and understand what her father has been doing all this time in Denmark.

Finally I would like to thank my girlfriend Elaine, who is as smart as she is beautiful, for all her support and love.

Publications

The following publications have been authored or coauthored during the course of the Ph.d. project:

Journal Publications

- Martin Schubert, Troels Suhr, Sara Ek, Elizaveta S. Semenova, Jørn M. Hvam, and Kresten Yvind, *Lambda shifted photonic crystal cavity laser*, Accepted by Applied Physics Letters

Conference proceedings

- Martin Schubert, Henri Nielsen Thyrrestrup, Lars Hagedorn Frandsen, Toke Lund-Hansen, Jeppe Johansen, Peter Lodahl, Kresten Yvind, Hvam, Jørn Märcher, *Fabrication and measurements on coupled photonic crystal cavities*, DOPS Årsmøde, 2008, Nyborg, Denmark

- Martin Schubert, Lars H. Frandsen, Troels Suhr, Toke Lund-Hansen, Henri Thyrrestrup, Max Bichler, Jonathan J. Finley, Peter Lodahl, Jørn M. Hvam, and Kresten Yvind, *Sub-threshold investigation of two coupled photonic crystal cavities*, CLEO, 2009, Baltimore, USA

- M. Schubert, L. H. Frandsen, T. Suhr, T. Lund-Hansen, H. Thyrrestrup, P. Lodahl, J. M. Hvam, K. Yvind, *Sub-threshold wavelength splitting in coupled photonic crystal cavity arrays*, PECS, 2009, Sydney, Australia

- Troels Suhr, Philip Trøst Kristensen, Lars Hagedorn Frandsen, Martin Schubert, Niels Gregersen, Jesper Mørk, *Nonlinear dynamics in photonic crystal nanocavity lasers*, CLEO/Europe, 2009, Munich, Germany

- Martin Schubert, Sara Ek, Troels Suhr, Elizaveta Semenova, Jørn M. Hvam, Kresten Yvind, *Quarter-lambda-shifted photonic crystal lasers*, ISLC, 2010, Kyoto, Japan

- Sara Ek, Martin Schubert, Kresten Yvind and Jesper Mørk, *Enhanced Amplified Spontaneous Emission in III-V Semiconductor Photonic Crystal Waveguide*, IPR, 2010, Santa Barbara, USA

Abstract

This thesis describes the design, fabrication and characterization of photonic crystal slab lasers. The main focus is on coupled photonic crystal cavity lasers which are examined in great detail. The cavity type which is mainly explored consists of a defect formed by a single missing hole in the quadratic lattice.

Processing techniques are developed and optimized in order fabricate photonic crystals membranes in gallium arsenide with quantum dots as gain medium and in indium gallium arsenide phosphide with quantum wells as gain medium.

Several key issues in process to ensure good quality are identified such as the size and material for the carrier wafer in the III-V etch and the importance of removing all remains of the e-beam lithography mask after the etch of the hard mask.

Detailed simulations are shown for a simple system with two coupled cavities in different coupling directions. The results are in good agreement with standard coupled mode theory. Also a novel type of photonic crystal structure is proposed called lambda shifted cavity which is a two-dimensional photonic crystal laser analog of a VCSEL laser.

Detailed measurements of the coupled modes in the photonic crystals with quantum dots are carried out. In agreement with a simple gain model the structures do not show stimulated emission. The spectral splitting due to the coupling between single cavities as well as arrays of

cavities is studied theoretically and experimentally.

Lasing is observed for photonic crystal cavity structures with quantum wells. A detailed Analysis is conducted on single cavities, two coupled cavities and arrays of coupled cavities. The lasing threshold is determined by measuring the photoluminescence intensity depending on the excitation power. Changes in the linewidth and peak position for different powers confirm the results. While large arrays of coupled cavities exhibit lasing at a single frequency, multimode lasing is demonstrated in structures with only a few coupled cavities. Moreover, lasing is also observed in the lambda shifted cavities. Simulations are shown to determine the theoretical Q factors and mode volumes of these novel structures.

Resumé

Denne afhandling beskriver design, fabrikation og karakterisering af fotoniske krystal membranlaserer. Hovedvægten er lagt på fotoniske krystal kavitetslaserer, som er undersøgt i stor detalje. Kavitetstypen som primært er blevet undersøgt består af en defekt dannet af et manglende hul i det kvadratiske gitter.

Forskellige processeringstekniker er blevet udviklet for at kunne fabrikere fotoniske krystaller kvante i Gallium-arsenid med kvantepunkter som forstærkningsmedium og i Indium-gallium-arsenid-phosfid med kvantebrønde som forstærkningsmedium.

Der er identificeret adskillige punkter der er afgørende for at sikre god en kvalitet af de fotoniske krystaller, såsom størrelsen og materialet af bærewaferen vedi III-V ætsningen samt vigtigheden af at fjerne alle rester fra elektronstrålelitografimasken efter ætsningen af hårdmasken.

Der er udført detaljerede simuleringer for et simpelt system med to koblede kaviteter i forskellige koblingsretninger. Resultaterne er i god overensstemmelse med standardteori for koblede tilstande. Herudover er en ny type af fotoniske krystalstrukturer foreslået - kaldet en lambda-skiftet kavitet, hvilet er en to-dimensionel fotonisk krystal analog til en VCSEL laser.

Detaljerede målinger af den koblede tilstande i fotoniske krystaller med kvantepunkter er blevet udført. I overensstemmelse med en simpel model er det vist at strukturerne ikke udviser stimuleret lysudsendelsee-

mission. Den spektrale opsplitning der opstår på grund af koblingen mellem enkelte kaviteter såvel som mellem arrays af kaviteter er studeret teoretisk og eksperimentelt.

Laseropførsel er observeret på for fotoniske krystalkavitetsstrukturer med kvantebrønde. En detaljeret analyse er blevet udført på enkelte kaviteter, på to koblede kaviteter samt på arrays af koblede kaviteter. Lasertæsklen er bestemt ved at måle fotoluminisense intensitetens afhængigt af excitationseffekten. Ændringer i liniebredden og centerpositionen for forskellige excitationseffekter bekræfter resultatet. Mens store arrays af koblede kaviteter udviser laseropførsel ved en enkelt frekvent, er laseropførsel ved mange samtidige bølgelængder demonstreret i strukturer med kun få koblede kaviteter. Herudover er laseropførsel også blevet observeret i de forudsagte lambda-skiftede kaviteter. Simuleringer er udført for at bestemme de teoretiske Q-faktorer og modevolumner af disse nye strukturer.

Contents

Chapter 1

Introduction

"Good students want to be challenged. Otherwise they might be bright but lazy!" - Professor at DTU Fotonik

In the last twenty years the rise of the internet has resulted in an ever increasing need for bandwidth in our optical communication systems. There seems to be no end in this demand as video stream services are slowly starting to replace traditional channels of video distribution and TV broadcasting. Connectivity is not limited to the home anymore as more and more consumers demand ubiquitous access to the net in the form of smartphones and other portable internet devices. Fibre based optical systems are the unseen backbone of this communication infrastructure that transmit data in huge quantities across the globe. Processing and routing of this data has to be done electrically due to a lack of components which are able to do this optically. Replacing these electrical data processing components with optical components would reap huge benefits and has fueled the research of all-optical network solutions in the past decade. Replacing electrical components might not only increase bandwidth and speed but would also save energy which is wasted in converting optical signals into electrical signals and vice versa.

Photonic crystals (PhCs) have played a major role in the field of photonics research as they offer a great deal control of optical modes on an extremely small scale allowing for on chip optical processing offering functionalities like wavelength (de-)multiplexing, dispersion control, increased light-matter interaction and optical buffering.

Especially the increased light-matter interaction is interesting for the fabrication of PhC lasers as it allows the gain material to couple more strongly with the optical mode and allows for an ultra-low threshold. Besides being an interesting device in itself the PhC lasers also represent the next logical step in expanding the functionality of all optical networks by integrating the sources on the chip and directly modulating them.

This thesis was mainly carried out in the scope of the "Coupled photonic crystal array laser" (CORAL) project. Towards the end of the thesis support was also provided by the "Nanophotonics for Terabit Communications" (NATEC) project. The initial idea of the CORAL project was to carefully examine a type of exciting new structure which carries the same name as the project. This type of device first demonstrated by Altug *et al.* [1] sought to increase the output of a single PhC quantum-well nanolaser from a few nW to a more useful level by coupling a large number of cavities while maintaining the advantages of a nanolaser, namely the ultra-low threshold, allowing for ultra-fast modulation. Results suggesting that this is possible where published only shortly after indicating that this might be a viable route in the engineering of a new type of high speed directly modulated laser that could be used for telecommunication purposes [2].

The main task of the PhD project was therefore to examine and understand coupled PhC cavity structures and to try to determine whether coupled PhC cavity lasers are promising candidates in the fabrication of ultra-fast lasers for applications in telecommunication systems. The PhD project started out as mainly fabrication oriented but required also optical characterization including the build up of a completely new micro

photoluminescence setup and some modeling of the structures. The fabrication of PhC in gallium arsenide (GaAs) and indium phosphide (InP) was a major challenge and an achievement of this thesis was to develop the fabrication techniques necessary to fabricate PhC structures with sufficient quality to allow for lasing. Apart from examining coupled cavity structures similar to the ones shown by Altug *et al.* [3] another kind of PhC cavity with a possible application in on chip-light manipulation was examined.

The thesis is split into four main chapters excluding conclusion and introduction and four appendices. Chapter 2 provides the theoretical basis introducing PhCs, coupled PhCs and PhC lasers. Simulations of the structures experimentally examined later in the thesis are shown. Rate equations for PhC lasers are introduced and a simple gain model is presented to analyze the requirements for lasing in PhC cavities. Chapter 3 explains how to fabricate PhCs in GaAs and InGaAsP in a methane-hydrogen (CH_4/H_2) plasma using a conventional reactive ion chamber. Chapter 4 and 5 present the measurement results on the fabricated structures. Measurements were done in two different material systems. PhC cavities in GaAs membranes with QDs as gain medium are presented in chapter 4. The cavities did not exhibit lasing but proved to be very useful in probing the mode structure of the coupled cavity systems. The spectral splitting between two coupled cavities is measured and compared to 3D finite difference time domain (FDTD) simulations. Larger arrays of coupled cavities are also presented but direct comparison to simulations is difficult due to the large number of modes. Chapter 5 shows PhC lasers fabricated in indium gallium arsenide phosphide (InGaAsP) membranes with quantum wells as a gain medium using the similar patterns as in chapter 4. Lasing is observed on single cavities and coupled cavity systems. The appendices A and B focus on various technical aspects of the fabrication procedure to make sure the techniques developed in the course of this thesis are well documented. A full recipe list can be found

in appendix C. A list of used abbreviations and the bibliography can be found after the appendices.

Chapter 2

Theory of photonic crystal lasers

"And if the Japanese can't engineer it better, then you know that you have reached some sort of fundamental limit." - Professor at DTU Fotonik

This chapter provides the theoretical foundation for the experiments presented in this thesis. An introduction to PhCs in general is given in section 2.1.1. Section 2.1.2 introduces the concept of PhC slabs which are an excellent substitute for "true" 3D PhC. Two types of cavities in PhC slabs, single hole missing defects (H1) in the quadratic lattice and so called lambda shifted cavities are described in detail in section 2.1.4 and 2.1.5, respectively.

After the introduction of single H1 defects, coupled H1 defects are discussed in section 2.2. Simulations of two coupled cavities are presented in section 2.2.1 and larger coupled arrays are discussed in section 2.2.2. The last section, section 2.3 is concerned with the inclusion of gain media in PhC. Section 2.3.1 discusses lasing in PhCs and section 2.3.2 shows a very simple estimation for the gain provided and the gain needed to reach threshold for the PhC cavities presented in chapter 4.

2.1   Photonic crystals

2.1.1   Introduction to photonic crystals

PhCs, first introduced by Yablonvitch [4] and John [5] in 1987, are defined as low loss dielectric materials with periodic regions of high and low refractive index. A good general overview of the field of PhC research can be found in the textbook "Molding the Flow of Light" [6].

The behavior of photons in PhCs is usually described in close analogy to the behavior of electrons in solids with crystalline structure. In a crystalline structure electrons are scattered by the periodic potential of the atoms. The scattering can cause that the propagation of electrons with certain energies in certain directions to be inhibited and the forbidden energy regions are usually referred to as bandgaps. Similar to how electrons are scattered by the periodic potential of the atoms in a crystal, photons are scattered by the periodic potential of the dielectric function in a PhC. And also in a similar way the propagation of photons in PhCs is inhibited in certain directions due to Bragg reflection. This effect is both dependent on frequency and propagation direction of the light and it also depends on the polarization of the light.

It should be mentioned though that the concept of using alternating layers of dielectric materials in order to reflect the light, in so called Bragg reflector, is much older than the general description of PhCs in two and three dimensions and was first explained by Lord Rayleigh in 1887. Bragg reflectors are a standard optical component and have found widespread application in for example DFB lasers or dielectric mirrors.

The forbidden energy regions in a PhC are called photonic bandgaps analog to their electronic counterparts. A complete photonic bandgap denotes an omnidirectional bandgap in which the effect is not dependent on the propagation direction of the wave. PhC structures differ depending on in how many dimensions light is to be confined. Figure 2.1 shows example of PhC structures to confine light in one, two and three dimen-

1D   **2D**   **3D**
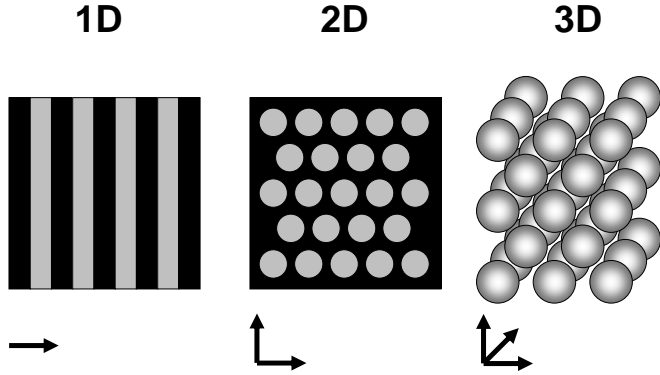
Figure 2.1: Examples of one, two and three dimensional PhCs. Showing alternating layers of dielectric materials (Bragg grating), a triangular lattice of holes (2D PhC pattern) and a stack of spheres ordered in a fcc lattice (3D PhC pattern), respectively

sions. Apart from the periodicity there is another important condition for the confinement of light in PhC crystal which is implied by the effect being based on Bragg reflection. The periodicity of the structures has to be on the order of the wavelength of the confined light. It is therefore hardly surprising that initial successes in the fabrication of PhCs with complete bandgaps were made in the microwave regime [7]. Later followed by structures operating in the NIR [8].

Unfortunately, the design and fabrication of "true" 3D PhCs, which is a PhC that confines light in all three dimensions using the photonic bandgap effect and therefore has a complete bandgap, is very challenging [6]. A good substitute for "true" 3D PhCs are so called PhC slabs [9], which are described in more detail in section 2.1.2. Light in PhC slabs is confined by a combination of total internal reflection and the Bragg reflection from the PhC pattern.

The PhC structures discussed so far could be called bulk PhCs since they are free of defects. By introducing defects into a PhC it is possible to create cavities that can confine light in a very small volume on the order

of a cubic wavelength [10]. This makes it possible to strongly couple light and matter inside such a cavity. PhCs can also be used to control the spontaneous emission from emitters embedded in the crystal [11]. It is possible to inhibit emission [12] as well as increase it by placing an emitter in a cavity. The emission is increased due to the so called Purcell enhancement [13], which is caused by the overlap between the emitter and the optical density of states of the cavity structure. By inhibiting emission at wavelengths other than the cavity resonance the radiation rate into the cavity mode is greatly enhanced.

Furthermore, PhCs can be used to fabricate waveguides (WGs) by introducing rows of defects which are especially interesting in the context of controlling the dispersion of the light inside the WG. By tailoring the dispersion it is possible to slow light down and create components like delay lines and optical buffers as well as increasing the light-matter interaction in the WG [14]. PhCs are very flexible and therefore it is quite easy to couple WGs and cavities which has fostered the idea of using PhCs to create optical circuits [6].

Although PhCs have proven to be an excellent scientific tool, apart from Bragg gratings no widespread commercial applications have emerged yet despite a lot of research effort. PhC lasers have been fabricated for many different cavity types, but a major obstacle for applications, apart from the low output power (a few nW), is that still no way has been found to efficiently electrically pump these lasers. There are a few example of electrical driven PhC lasers, but their fabrication is extremely challenging [15] and their performance is rather poor compared to conventional diode lasers. One of the main problems in electrically driven PhC lasers is the fact that most of the electric current is lost in the PhC surrounding the cavity due to the high amount of losses at the hole interfaces [16, 17].

2.1.2 Photonic crystals slabs

A PhC slab is usually a thin slab of dielectric material clad in a lower index material. Confinement of light in plane is reached by patterning the slab using a 2D PhC design while light confinement out of plane is reached by total internal reflection. A common type of PhC slab is a thin membrane with holes arranged in a PhC pattern. The lower index material in that case is the air surrounding the membrane and filling the holes. Confinement of light in a PhC slab is limited by the critical angle of the total internal reflection (TIR) [9].

Like in an index guided WG, k vectors, which are too large, will couple to lossy radiation modes through the evanescent tails of the PhC modes with the air regions. These modes lie inside the lightcone which is defined as:

$$\omega \geqq \frac{c_{vac}}{n} |k| \tag{2.1}$$

$$|k| = \sqrt{k_x^2 + k_y^2 + k_z^2} \tag{2.2}$$

with c_{vac} = the speed of light in vacuum and n = refractive index of the high index medium.

Although modes in a PhC slab inherently couple to lossy radiation modes [6], they have been used to fabricate optical cavities in silicon with very high quality factors (Qs) of around 10^6 [18]. The Qs of cavities fabricated in III-V semiconductors are slightly lower than in silicon with state of the art cavities showing Qs of around 10^5 [19, 20].

A central part in the design of a PhC slab is the 2D PhC pattern that is used to confine the light in plane. In 2D PhC modes can be classified as either transverse electric (TE) or transverse magnetic (TM) modes depending on the polarization of the mode. TE means the magnetic field component is polarized perpendicular to the slab and the electric field is polarized in the transverse direction while in TM modes the electric field is perpendicularly polarized and the magnetic field is polarized in the transverse direction.
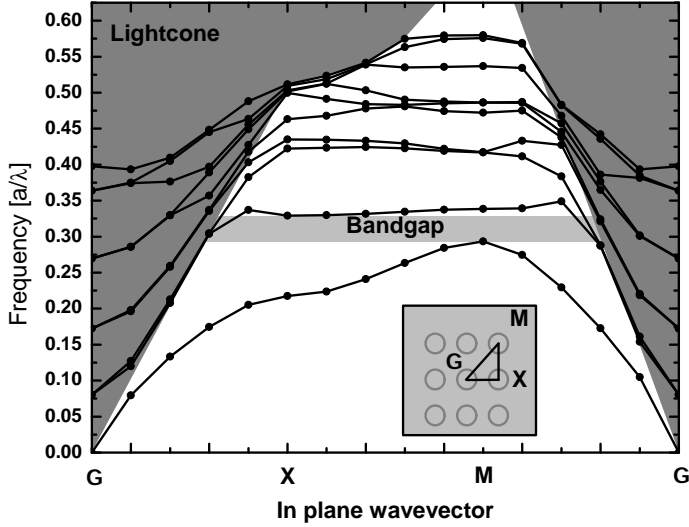
Figure 2.2: Dispersion diagram of a PhC slab with slab thickness $d = 0.75\,a$ and hole radius $r = 0.4\,a$ (a = lattice pitch of the PhC)

Figure 2.2 shows the band diagram for quasi transverse electric (TE) polarized modes of a PhC slab patterned with holes arranged in 2D projection of the simple cubic lattice (scc) [21]. The pattern is indicated in the small inset in figure 2.2. The bands are plotted over the k vectors along the direction of the high symmetry points of the irreducible Brillouin zone of the scc which is an isosceles triangle. Both the symmetry points and the irreducible Brillouin zone are indicated in the inset.

Due to the scalability of Maxwell laws it is possible to normalize the structure to its lattice pitch [6]. Slab thickness and radius of the holes are given as dimensionless fractions of the lattice pitch a and the frequency is plotted in units of $\frac{a}{\lambda}$ (λ = wavelength). The structure shown in figure 2.2 has a hole size $r = 0.4\,a$ and a slab thickness $d = 0.75\,a$.

The band diagram was simulated using the MIT Photonic-Bands
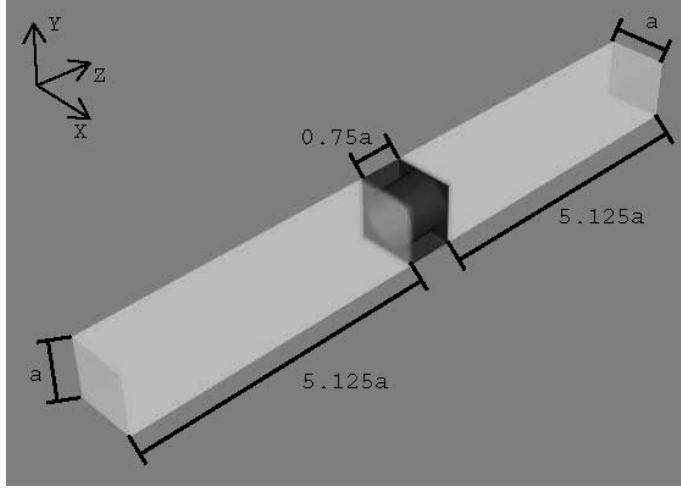
Figure 2.3: Supercell used to calculate the dispersion diagram of a PhC slab.

(MPB) package [22] which is a calculation software using the plane wave expansion method . The boundary conditions in MPB are periodic in all directions. Since the PhC is not periodic in the direction perpendicular to the slab, the unit cell is enlarged to ten lattice pitches perpendicular to the slab to make sure the modes, confined in the slab, do not couple to the next supercells above or below the slab. A resolution of twenty points per unit cell are used. In plane the supercell consists of a single hole. A scalar cut through the supercell is depicted in figure 2.3.

Apart from the quadratic lattice the triangular lattice is commonly used to confine light in PhC slabs. The triangular lattice is the projection of the face centered cubic (fcc) lattice [21] and has been shown to have a larger bandgap than the quadratic lattice. The reason for using the quadratic lattice is somewhat arbitrary and connected to the specific defect modes described in the following section. There is no fundamental reason though why similar results for coupled modes as presented in section 2.2 could not have been obtained in the triangular lattice.

2.1.3   Basic definitions for cavities in photonic crystal slabs

Before discussing specific PhC cavities it is useful to introduce a few basic concepts to characterize cavities in PhC slabs.

Quality factor (Q)

The Q is a measure of the energy that is lost for every round-trip of the photons in the cavity [23] and is linked to the average photon lifetime τ_p in the cavity. The higher the Q is the longer the average lifetime becomes. The photon lifetime can be estimated to be:

$$\tau_p = \frac{Q}{\omega_c} \tag{2.3}$$

with ω_c being the resonance frequency of the cavity. The Q is determined by the reflectivity of the "mirrors" surrounding the cavity. A high reflectivity means that less light is lost from the cavity due to the evanescent tails of the mode. The "mirrors" in a PhC are the rows of holes around the defect. By adding additional rows of holes the reflectivity can be increased and thereby the Q factor [24]. In a PhC slab though light does not only escape in plane but also out of plane due to k vectors that lie inside the light cone. Disregarding any additional losses from absorption or imperfections the Q of a cavity in PhC slab can be split in an out of plane loss part ($Q_\perp$) and an in plane loss part ($Q_\parallel$):

$$\frac{1}{Q} = \frac{1}{Q_\perp} + \frac{1}{Q_\parallel} \tag{2.4}$$

By increasing the number of rows of holes surrounding the cavity the Q factor becomes dominated by $Q_\perp$ and adding additional rows of holes will not significantly improve the Q anymore [24].

Assuming a Lorentzian lineshape for the cavity the Q of a resonant mode can be measured using the linewidth:

$$Q = \frac{\omega_c}{\omega_{\text{FWHM}}} \tag{2.5}$$

with the resonance frequency of the mode ω_c and the full width half maximum of the mode ω_{FWHM}.

Mode volume (V_{mode})

The mode volume is a measure of how tightly the mode is localized to the PhC cavity. PhCs allow very strong localization of modes and mode volumes close to a single cubic wavelength have been realized [25]. Determining the mode volume for a PhC cavity is difficult though due to the complex structure of the modes in the PhC and usually requires to simulate the structure and extract a mode profile. The mode volume can then be determined with the dielectric function $\epsilon(\overrightarrow{r})$ and the electric field function $E_{mode}(\overrightarrow{r})$ of the mode profile:

$$V_{mode} = \frac{\int d^3r \epsilon(\overrightarrow{r})|E_{mode}(\overrightarrow{r})|^2}{max\{\epsilon(\overrightarrow{r})|E_{mode}(\overrightarrow{r})|^2\}} \, (V_{mode} \text{in units of} \frac{\lambda}{2n}^3) \qquad (2.6)$$

PhC slabs do support strongly localized modes but there seems to be a trade off between localization and Q. The stronger localized a mode is the more difficult it becomes to keep the radiation losses low [6]. There is no general recipe on how to fabricate cavities with a high Q and ultrasmall mode volumes but it has been shown that by slightly shifting holes to reduce the overlap between the mode and the air regions it is possible to reduce radiation losses while keeping a small mode volume ("...light should be confined gently in order to be confined strongly.") [26].

Purcell enhancement factor(F)

The Purcell enhancement factor F is a measure of the enhanced light-matter interaction in a PhC. The more tightly the mode confined is and the higher the Q the large is the enhancement factor. It can be written as:

$$F = \frac{6}{\pi^2} \frac{Q}{V_{mode}} \qquad (2.7)$$
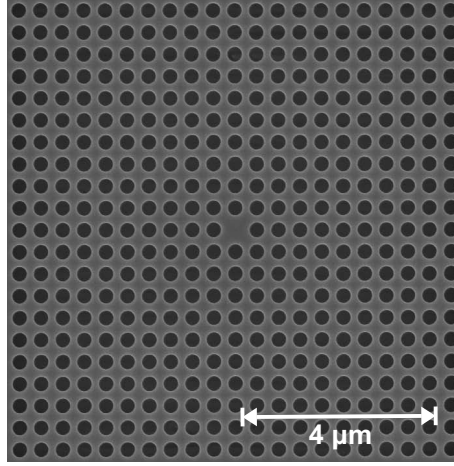
Figure 2.4: SEM image of a H1 PhC cavity in the quadratic lattice

2.1.4   H1 defect in the quadratic lattice

There is no standardized nomenclature for PhC defects, but there are some definitions which are commonly used and will be used throughout the thesis. A defect named with the letter H followed by a number n is usually a defect created by removing a single hole and the $(n - 1)$ neighboring holes around that hole. A H1 defect is therefore created by removing a single hole. A H2 defect is created by removing a hole and all the holes surrounding that hole. In a H3 defect a central hole and all of the two next neighboring holes are removed and so on. Cavities are also sometimes named H0 cavities which means that no holes are removed and the cavity is created only by shifting holes. Furthermore cavities are additionally called "modified", e.g. "a modified H1 cavity", which indicates that apart from a hole being removed other holes might have been shifted in position or modified in size.

The type of defect which is central to this thesis is the H1 defect in the quadratic lattice. All of the coupled cavities described are coupled H1 defects. It is therefore important to understand the mode structure

(a) Quadrupole   (b) x dipole   (c) y dipole
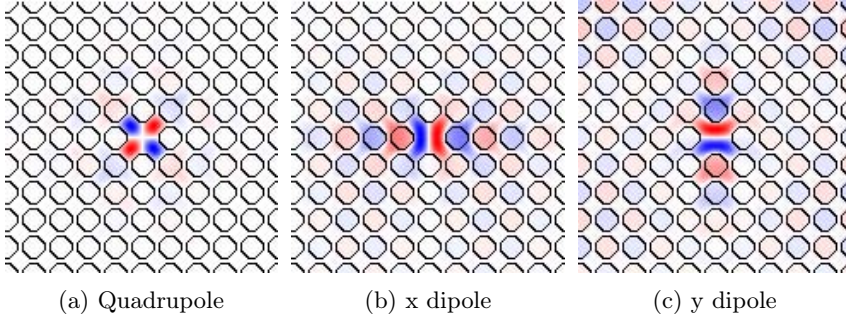
Figure 2.5: Mode profiles of the x-dipole, y-dipole and quadrupole mode in the H1 cavity in the quadratic lattice

of this PhC cavity in order to interpret the coupled cavities. A SEM image of a H1 cavity is depicted in figure 2.4.

There are two prominent TE polarized modes in the H1 cavity which we will focus on, a dipole mode and a quadrupole mode [2]. The dipole mode is degenerate resulting in two dipoles with different polarizations that we will refer to as x and y dipole. The magnetic field component perpendicular to the PhC slab of all three modes is shown in figure 2.5.

The H1 cavity in the quadratic lattice is calculated using MIT Electromagnetic Equation Propagation (MEEP) a FDTD solver [27]. The parameters used to calculate the modes are given in table 2.1. As in MPB the parameters can be normalized to the pitch a but instead of periodic boundary conditions MEEP can also use perfectly matched layers. An actual value for the pitch is chosen in order to calculate the resonance wavelength $\lambda_{res} = \frac{a}{\omega_{\text{MEEP}}}$ (with $\omega_{\text{MEEP}} = \omega_{res}\frac{a}{c}$ the normalized resonance frequency calculated by MEEP and $\omega_{res} = \frac{c_{vac}}{\lambda_{res}}$). Figure 2.6 shows the resonance wavelength and the Q factor of the quadrupole and of the degenerate dipole. The modes were calculated in a full 3D simulation and the parameters used are similar to the parameters of the PhC shown in chapter 4. The dipole has a much lower theoretical Q fac-

Parameter	Value
pitch a	280 [nm]
radius r	106 [nm] ($\frac{r}{a} = 0.38$)
slab thickness d	165 [nm] ($\frac{d}{a} = 0.59$)
resolution	20 [points per a]
number of holes around cavity	6
refractive index n	3.5
cell size perpendicular to slab (including perfectly matched layers)	8 [a] total

Table 2.1: MEEP parameters used to calculate H1 single and coupled cavities in the quadratic lattice

tor of around 350 compared to the theoretical Q factor of around 30000 of the quadrupole mode. The two modes are separated by around 50nm spectrally and the quadrupole mode has a higher energy than the dipole mode.

2.1.5   Lambda shifted defect

The design presented in this section shows a simple and yet intuitive way of trying to achieve a moderate Q and low mode volume through shifting all the holes in the lattice by a fraction of the desired emission wavelength. In Fig. 2.7 the design principle is demonstrated. A sketch of an unperturbed square PhC lattice is shown in Fig. 2.7(a). Arrows are indicating the shift directions of the holes. All the holes are radially shifted by the same amount from the center point of the cavity. Though the total amount of shift in the radial direction is always the same the actual horizontal and vertical shifts depend on the position of the hole.

By moving the holes in this fashion a phase shift is introduced between the different sides of the cavity "mirrors". The cavity resonance is designed by picking a target wavelength and using quarter lambda shifts
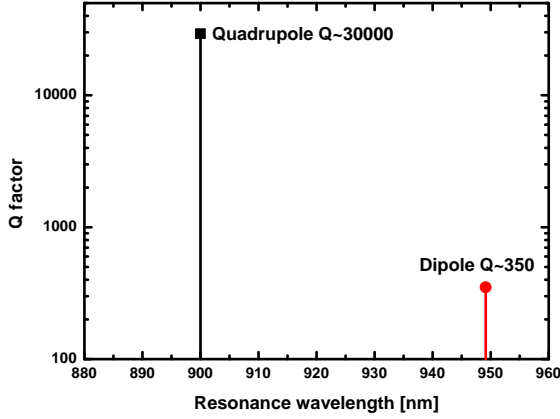
Figure 2.6: Resonance wavelength of the dipole and quadrupole mode of a H1 cavity in the quadratic lattice calculated using MEEP.

of this wavelength so that either a peak or a node is formed at the center of the cavity by distributed feedback (DFB) similar as in a conventional DFB laser. To ensure a small penetration into the PhC and thereby a high Q factor the Bloch mode in the center of the bandgap of the PhC needs to be excited. The hole size and pitch of the PhC are therefore chosen so that the bandgap of the unperturbed PhC pattern is centered on the target wavelength of the cavity.

As an example, a SEM image of a 5/4 lambda shifted cavity is shown in Fig. 2.7b. In the center of the structure, the cavity can be clearly seen by comparing the diagonal distance between the holes in the center and at the edge of the picture. Designs similar to the one presented here in Fig. 2.7 are those of vertical cavity surface emitting lasers (VCSELs) and nanocavity lasers using so called circular Bragg cavities [28], which have been shown to achieve extremely low mode volumes. Our design aims for similar low mode volumes while maintaining the structure of a PhC.
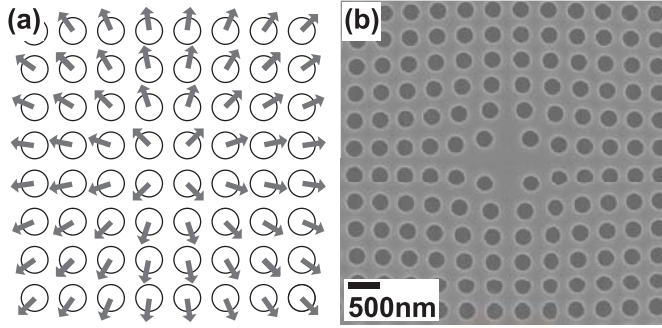
Figure 2.7: a) Stylized unperturbed PhC lattice with arrows indicating shift direction b) SEM image of a 5/4 lambda shifted cavity

It should be pointed out that our design approach differs from the usual PhC cavity design approach in so far that the defect introduced to the structure is specifically designed to allow for a certain resonance from the beginning rather than introducing a defect and then modifying and tuning the crystal to obtain a desired resonance. However, as the PhC bandgap originates from the regularity of the crystal, shifting all holes in this fashion also breaks the regularity of the unperturbed lattice which will affect the properties of the underlying PhC bandgap. This is important because one of the advantages of the design is the possibility to combine it with, for example, common PhC WGs. It is therefore important to use a small shift in order to minimize the disturbance to the PhC pattern. Due to this we believe the 1/4 shifted cavity to be the most interesting one. Furthermore, larger shifts are expected to give larger mode volumes.

The design is based on a square PhC lattice, but it could also be realized in a triangular lattice in the same way which might be advantageous due to the larger bandgap in the triangular lattice [6]. The design is well suited to be coupled to standard PhC WGs and is a promising candidate for ultra-fast switching application [29].
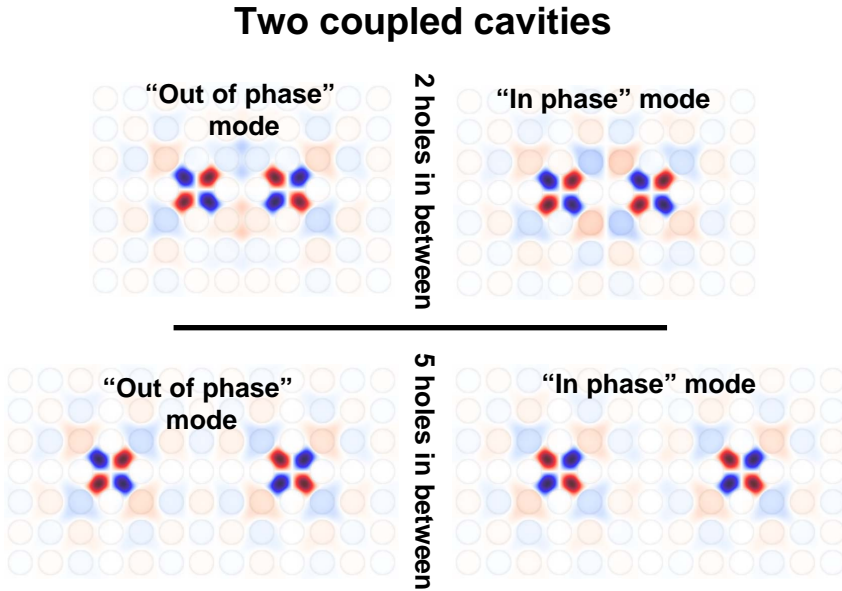
Figure 2.8: Mode patterns for two coupled H1 cavities in the quadratic lattice.

2.2   Coupled photonic crystal cavities

Coupled PhC cavities can be described using a tight binding formalism [30, 31]. The individual cavities couple to each other due to the evanescent tails of the bloch modes. In the weak coupling regime the coupled eigenmodes are essentially the same as the eigenmodes of the individual cavities. Before describing arrays of coupled cavities it is useful to start with only two coupled cavities.

2.2.1   Two coupled H1 cavities in the quadratic lattice system

In this section the simulation results of two coupled H1 cavities in the quadratic lattice with different intrahole distances are shown. As for the
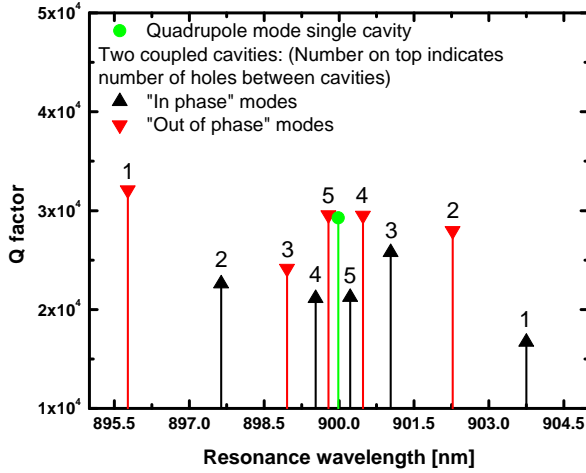
Figure 2.9: Calculated resonance frequencies and Q factors for two cou-
pled H1 PhC cavities in the quadratic lattice.

single cavities in section 2.1.4 the coupled cavities are simulated using
MEEP [27]. The calculations are done in 3D and the same parameters
are used as for the single cavity which are shown in table 2.1. Figure 2.8
shows the structure as well as the mode profile of two coupled cavities
with intrahole spacings of two and five holes. As can be expected from
coupled mode theory two different modes can be seen. An "in phase"
mode and an "out of phase" mode which can be distinguished by com-
paring the mode profiles in both cavities. The "in phase" mode is even
under point symmetry from the center point between both cavities while
the "out of phase" mode is odd. The cavities are coupled along the Γ-
X direction, calculations were also done for the Γ-M direction and are
compared to experimental results in chapter 4.

    Figure 2.9 shows the resonance wavelength of the coupled quadrupole
mode for hole separations of one to five holes. The number of holes
between the two cavities changes the coupling strength between both
modes as can be seen by the difference in resonance wavelength between
the "in phase" and the "out of phase" mode. For large separations the

resonance wavelength of both modes is almost identical to the resonance wavelength of the single cavity. Depending on whether the number of holes between cavities is odd or even, the "in phase" mode has either a higher or lower energy than the "out of phase" mode. The reason for this is that depending on the number of holes the field between cavities will be distributed differently causing either the "in phase" mode or "out of phase" mode to overlap more strongly with the holes [32].

2.2.2 Arrays of coupled H1 cavities in the quadratic lattice system

The problem in calculating coupled cavity arrays is usually the size of the array as well as the large number of modes that need to be calculated. Calculating more than two coupled cavities in 3D using MEEP requires long calculation times and becomes at some point unfeasible. In order to show that also for more than two coupled cavities the arrays behave as can be expected from coupled mode theory, small arrays with two by two coupled cavities were calculated in 2D using MPB.

Due to the periodic boundary conditions it is necessary to use 10 rows of holes surrounding the cavities to get a good approximation of the modes by calculating the quasi eigenmodes of the coupled cavity structure. To calculate the actual eigenmodes of the system it would be necessary to expand the PhC surrounding the cavities to infinity. The modes are calculated at the Γ point to get an impression of the mode patterns and their position in the bandgap relative to each other. Using MPB in this way will not yield "useful" results when attempting to calculate dispersion relations though because instead of calculating the dispersion between the coupled cavities inside the supercell it will calculate the dispersion between the supercells. This is not an issue when calculating bulk PhCs since the structure itself shows the same periodicity as is used in the calculations.

Figure 2.10 shows the mode profile of two by two H1 coupled cavities
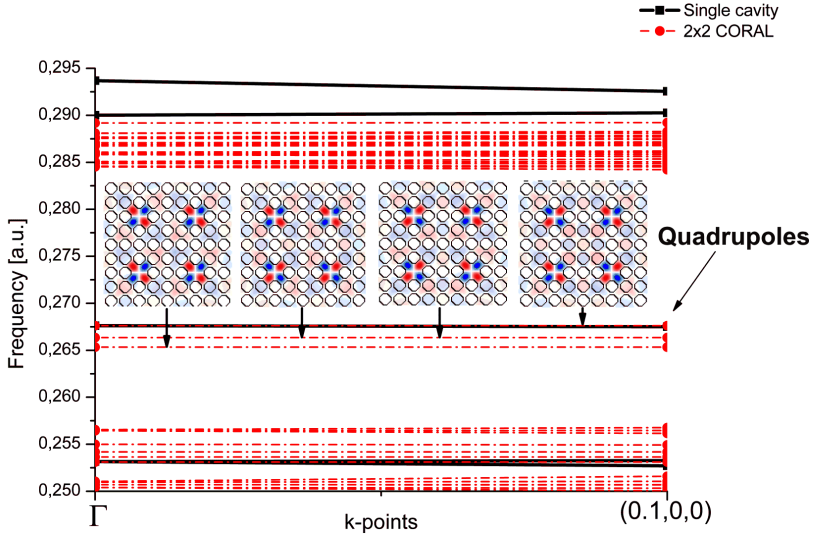
Figure 2.10: Mode patterns of 2x2 coupled H1 cavities in the quadratic lattice. Spectral splitting of the modes can be seen as well as the mode patterns. Dispersion relation can be disregarded and modes are only plotted for two k points to make them better visible.

in the quadratic lattice with two holes intercavity spacing. The modes are calculated at the Γ point. Four different combinations of "in-phase" and "out-of-phase" mode patterns can be seen. The center mode is degenerate due to symmetry reasons since the structure is invariant to rotations of 90 degrees around the center and the two outer modes are evenly spaced with the center modes.

Large arrays of coupled cavities can also be described using the dispersion relation of the coupled mode bands. An 2D MPB calculation showing the dispersion relation of the quadrupole and dipole mode is shown in figure 2.11 [33]. By changing the number of holes surrounding the cavity in the supercell the coupling can be varied due to the periodic boundary condition. As can be expected from the FDTD calculations
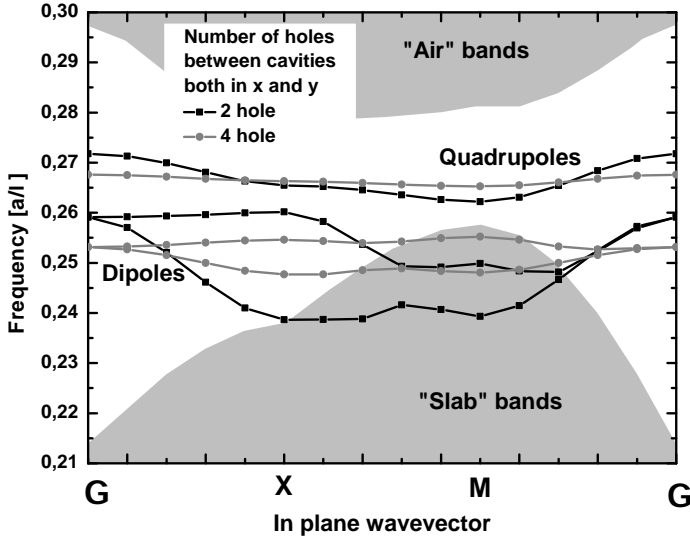
Figure 2.11: Dispersion relation of a two dimensional coupled PhC cavity array of H1 cavities in the quadratic lattice. Cavities are separated by two and by four holes.

done for the two coupled cavities in section 2.2.1 decreasing the amount of coupling between the cavities decreases the bending of the bands.

Calculating the band structure of the coupled modes in this way in MPB corresponds to calculating an infinite number of coupled cavities which results in an infinite number of closely spaced modes that form the coupled band. Different k points in the band diagram correspond to different phase relations between cavities. The mode at the Γ point for the coupled cavities with two holes intracavity spacing for example corresponds to the out phase mode of coupled cavity structure in the FDTD calculation.

2.3   Gain media inside of photonic crystals

The PhC cavities which were fabricated and characterized in this thesis were all grown in the III-V material system and used quantum wells (QWs) or quantum dots (QDs) as gain medium. The epitaxial structure of the wafers are described in section 3.3. QWs and QDs are well known as gain medium in semiconductor lasers [34, 35, 36].

2.3.1   Lasing in photonic crystal cavities

PhC lasers have been realized using a large number of different designs. The aim is usually as was discussed before to achieve a combination of high Q and low mode volume to achieve high β and large Purcell enhancement factors. Common designs are based on the removal of holes [37], changing the size [38] and/or shifting of the surrounding holes [39]. Cavities based on the shift of only a few holes, the so called H0 cavities, have also been realized [40] and recently cavities shifting a large numbers of holes have been theoretically proposed [41].

   PhC lasers are treated theoretically as diode lasers and most of the theory of lasing in PhCs is often directly derived from standard diode laser theory. According to Coldren and Corzine [34] the rate equations of a diode laser can be described by two coupled differential equations one for the photon density S and another for the carrier density N:

$$\frac{dN}{dt} = R_p - \frac{N}{\tau_{sp}} - \frac{N}{\tau_{nr}} - v_g g S \qquad (2.8)$$

$$\frac{dS}{dt} = \Gamma(v_g g S + \beta \frac{N}{\tau_{sp}}) - \frac{S}{\tau_c} \qquad (2.9)$$

R_p is the pump rate into the active layer and v_g the group velocity of the mode. $\frac{1}{\tau_{nr}}$ and $\frac{1}{\tau_{sp}}$ are the non-radiative and spontaneous recombination rate, respectively. In order to take into account that only a fraction of the optical mode overlaps with the gain medium the confinement factor Γ is introduced which is defined as the fraction of the volume occupied

by the mode over the volume occupied by the gain medium. g is defined as the modal gain and can be evaluated using a simple linear model:

$$g \sim \frac{\partial g}{\partial N}|_{N=N_{tr}}(N - N_{tr}) \qquad (2.10)$$

with N_{tr} being the transparency carrier density and $\frac{\partial g}{\partial N}$ being the differential gain. A linear approximation of the gain will not fit for high pump powers due to saturation effects.

β is the spontaneous emission factor obtained from the density of optical modes per unit volume per frequency. It is a measure of the amount of spontaneous emission that couples directly to the lasing mode compared to the emission into all other modes. The β of a regular diode laser is usually in the range of 10^{-3}-10^{-5}[34].

The output power curve of a laser plotted over the pump power is usually characterized by a notable kink which marks the lasing threshold. The kink becomes less pronounced the higher the beta factor becomes because a larger ratio of the spontaneous emission is directly emitted into the lasing mode. This also lowers the threshold of the laser [37]. Theoretically, a laser with a beta of unity will not show any kink in the output power curve and is therefore called a threshold less laser. The term "threshold less" might be misleading since although the kink disappears there is still a transition between spontaneous emission and stimulated emission in the cavity. This transition can be measured for example by determining the photon statistics using the g^2 function [19].

A threshold less laser has so far not been realized, but PhC cavities have been used to fabricate lasers that claim to show beta factors of up to 0.85 [19]. There is no doubt that PhC lasers do have beta factors which are orders of magnitudes higher then that of conventional edge emitting laser diodes, but there is an ongoing debate on the limitations of using the L-L curve to determine the beta factor. A large amount of parameters need to be used to fit the curve L-L curve and there are also
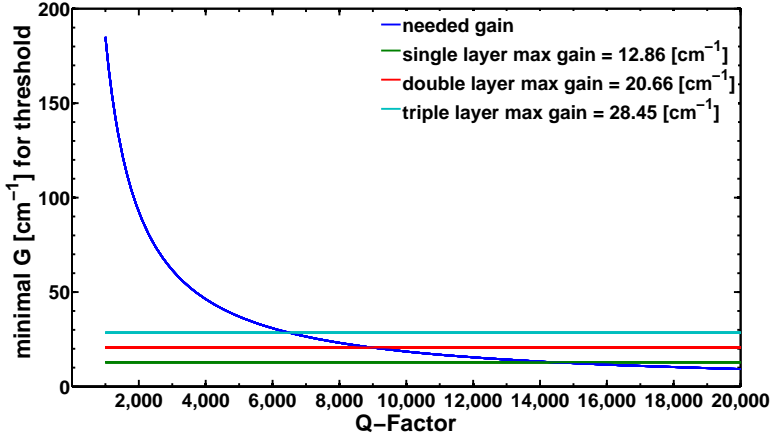
Figure 2.12: Threshold gain of a simplified small nanocavity and gain estimation of several layers of quantum dots.

some results showing that the pumping scheme might play an important role [42].

Despite the problems mentioned there have been some recent attempts to modify the standard diode laser theory in order to take better into account the effects from the large Purcell enhancement and high beta factors in PhC lasers [2, 43, 44]. A high beta factor and a high Purcell enhancement factor should make it possible to modulate lasers at a very high speed [45] which would make PhC cavity lasers a good candidate for directly modulated high speed lasers.

As already said in the introduction Altug et al. have claimed direct modulation speeds in PhC cavity lasers of up to 100 GHz [2] which is significantly higher than what has been demonstrated in conventional diode lasers. They claim the reason for this improvement is the high beta factor ($\sim$0.1) and the high purcell enhancement factor ($\sim$76) of the PhC cavities compared to conventional lasers. These result have been heavily criticized though and largely attributed to gain effects due to the optical pumping scheme used to pump the cavities [44]. Especially

the large enhancement of the modulation bandwidth in nanocavity lasers and nano light emitting diodes is being debated due to saturation of the Purcell enhancement under high pump conditions [44, 43].

2.3.2 Gain approximation for quantum dots and quantum wells

The threshold gain for an in-plane laser can be estimated using the photon lifetime of the cavity and the group velocity of the mode by neglecting spontaneous emission and evaluating the laser rate equations at steady state: [34]

$$0 = \Gamma v_g g S - \frac{S}{\tau_p} \tag{2.11}$$

$$\Rightarrow \Gamma g = \frac{1}{v_g \tau_p} \tag{2.12}$$

$$v_g = \frac{c_{vac}}{n_{eff} + \omega_c \frac{dn_{eff}}{d\omega}} \tag{2.13}$$

n_{eff} is the effective refractive index of the mode and ω_c the resonance frequency of the lasing mode. The QD gain G is estimated using a model proposed by Blood[46] that incorporates the confinement factor:

$$G = \frac{\delta_{dot} N_{dot}}{w_{mod}}, (\Gamma g = G) \tag{2.14}$$

N_{dot} is the dot density, δ_{dot} the effective cross section of the dot and w_{mod} the effective mode width.

Figure 2.12 shows the estimated threshold gain and the gain provided by one, two and three layers of QDs using the simple model described above for a nanocavity laser similar as the one described in chapter 4 including the wafer TUM01D the structures were fabricated on. The parameters which were used are given in table 2.2.

The resonance frequency used is around 900nm in wavelength. The group velocity of the mode is estimated using the refractive index of bulk

Parameter	Value
n_{GaAs}	~ 3.51(at 900nm)
ω_c	$1.8837 * 10^{15}[Hz]$
v_g	$1.0178 * 10^8[\frac{m}{s}]$
δ_{dot}	$4.5 * 10^{-19}[m^2]$
N_{dot}	$10 * 10^{14}[m^2]$
w_{mod}	$0.35 * 10^{-6}[m]$

Table 2.2: Parameters used for the simple threshold gain model

GaAs n_{GaAs} instead of the actual effective mode index n_{eff} of a specific PhC mode.

Taking into account that when using several QD layers not all of the layers will be located in the center it was assumed the mode will have a gaussian distribution across the PhC slab. The width of the gaussian was chosen so that 95 % of the area of the gaussian was inside a 160 nm thick membrane.

The positions of the QD layers matched those described in section 3.3 for wafer TUM01D. The effective gain of each layer was estimated by multiplying the gain with the intensity of the normalized gaussian corresponding to the position of the layers in the membrane.

The parameters used are only rough estimations and the value of the model should not be overrated. The n_{eff} is dependant on the PhC mode as is the overlap of the gain material with the QDs. Quantum effects like Purcell enhancement are also not taken into account which might play a role especially for large Qs and low V_{mode}. Despite this the model offers some explanation of why the nanocavities in chapter 4 did not exhibit lasing.

Chapter 3

Fabrication of photonic crystal structures in III-V semiconductors

"You can measure all you want, you will just find out what everybody already knows. Methane is a shit gas." - Senior Process Specialist at DANCHIP

3.1 Process overview

The aim of this section is to provide an overview of the processes used to fabricate the PhC slabs that are characterized in this thesis and to explain how these processes were developed in order to overcome the specific challenges of making PhCs.

All of the processing was done at Danchip which is the cleanroom facility at the Technical University of Denmark (DTU). Many of the challenges in the fabrication process are related to the equipment that was available at Danchip at the time of processing. Some of the indi-

vidual process steps will be explained in greater detail in the following sections.

Before starting to make a PhC slab it is necessary to design, define and fabricate an appropriate wafer structure. The wafer structures used for the optical experiments in this thesis are designed for two different wavelength region. The first are designed for wavelengths slightly below 1 micron and are epitaxially grown on a GaAs substrate. The second are designed for structures in the telecommunication wavelength around 1.5 microns and are epitaxially grown on an InP substrate.

The epitaxial structures of the wafers including the active layer of the membranes are described in section 3.3. The active material used are QWs and QDs. Because of the different wafer structures there are strictly speaking two almost identical processes being described here. One for the structures based in the GaAs system and one for the others in the InP system.

In order to not unnecessary lengthen the description of the fabrication process they are presented together and the differences between them are pointed out where appropriate in the text. A schematic overview of the process can be found in figure 3.1 and the complete process in a compact form can be found below:

1. The process starts by depositing a hard mask (silicon dioxide or silicon nitride (SiO_2 or Si_3N_4)) on top of the wafer in a PECVD reactor (200nm of Si_3N_4 in the final recipe).

2. On top of the hard mask 400-500 nm of ZEP 520A e-beam resist is spun. The thickness of both masks is important in the etch in order to achieve vertical sidewalls in the PhC as shown in section 3.4.1.

3. PhC patterns are defined in the e-beam resist by using a 100kV JEOL JBX-9300FS electron beam (e-beam) lithography system.
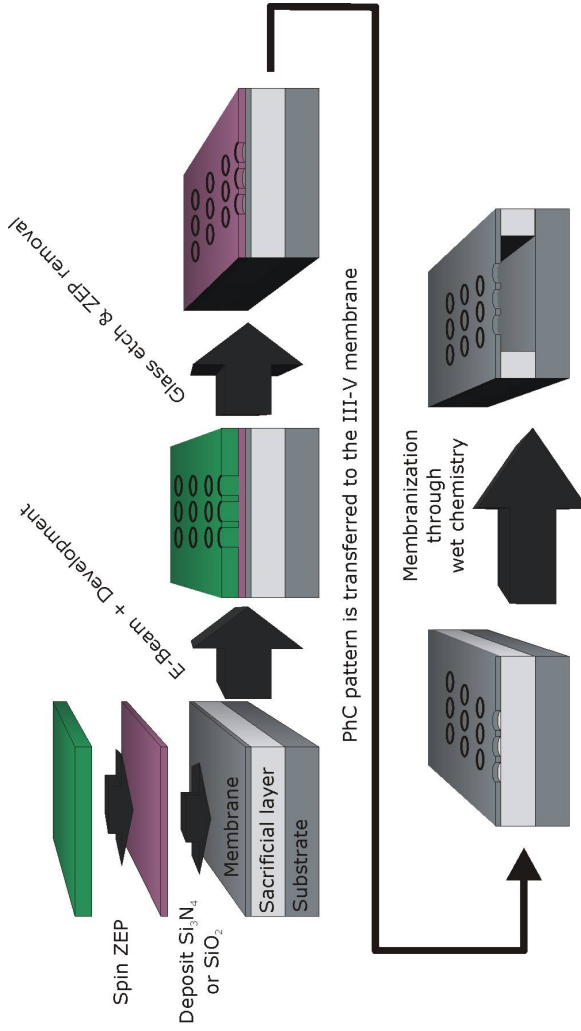
Figure 3.1: Schematic overview of the process to fabricate PhC slabs in GaAs/InGaAsP.

4. After the pattern has been written the wafer is developed in ZED N50 developer for two minutes. The sample is slightly shaken during development to ensure that the resist is removed all the way to the bottom in the holes. Typically the wafer is cleaved into smaller pieces for further processing at this point.

5. The next step is to transfer the pattern from the ZEP to the hard mask. This is done by reactive ion etching (RIE) using a freon/oxygen (CHF_3/O_2) plasma. Afterwards the rest of the e-beam resist is removed by placing the sample for 2 hours in heated Microposit 1165 Remover with a low level of ultrasound. This process step is critical because there is a risk that part of the ZEP will remain and stick to the sample. This is further discussed in section 3.4.1.

6. After the transfer to the hard mask the pattern is etched into the III-V material that will later form the membrane. This is done using a cyclic dry etch in the RIE with a methane/hydrogen (CH_4/H_2) plasma during the etch step and an O_2 plasma cleaning step in between etch cycle. The optimization of the etch process including the specific etch rates and etch times for GaAs and InGaAsP are described in section 3.5.1.

7. (optional) Depending on whether Si_3N_4 was used as a hard mask it might be necessary to remove the rest of the mask after the III-V etch by doing another dry etch using a CHF_3/O_2 plasma with low power and low pressure in order to avoid damage to the sample surface. The reasons for this extra mask removal in the case of using aluminum gallium arsenide (AlGaAs) as sacrificial layer can be found in section 3.6.1.

8. The final step is to release the membrane by wet etch. This is either done by using hydrofluoric acid (HF) in case the sacrificial layer is

AlGaAs or hydrochloric acid (HCl) in case the sacrificial layer is InP and/or indium aluminium arsenide (InAlAs). Both processes are described in section 3.6.1 and section 3.6.2 respectively.

The weak link in the fabrication process as whole is the RIE that is used to etch the glass as well as the III-V semiconductor. State of the art for etching of PhC is achieved using an inductively coupled plasma (ICP) etcher instead of a conventional RIE. ICP etchers have shown excellent results in etching PhCs with smooth sidewalls and high aspect ratios [47, 48, 49, 20].

A conventional RIE was used, based on the fact that no other machine was available at Danchip. There was also a strong interest in determining how much of the fabrication could be done in house to ensure a short fabrication cycle. While the results on InP/InGaAsP after optimization were acceptable, the results on GaAs did not reach state of the art. Furthermore, even for InP/InGaAsP we observed a minimum hole size which could be reproducibly fabricated. Because of this a new ICP etcher for III-V materials using chlorinated gases was installed at Danchip during the completion of this thesis which will probably be used for future processing.

3.2 Reactive ion etching

RIE is standard technique for anisotropic etching of semiconductors. The term is usually very loosely used and refers to several kinds of plasma assisted etching techniques. It is also used to refer to either the technique or the machine used for the etching.

This section will give a short introduction to RIE introduce a few basic principles that are important when fabricating PhCs. RIE and plasma etching in semiconductor fabrication is a standard method that is described in several textbooks. A good article on the general principles can be found here [50]. RIE is strictly speaking a misnomer since high
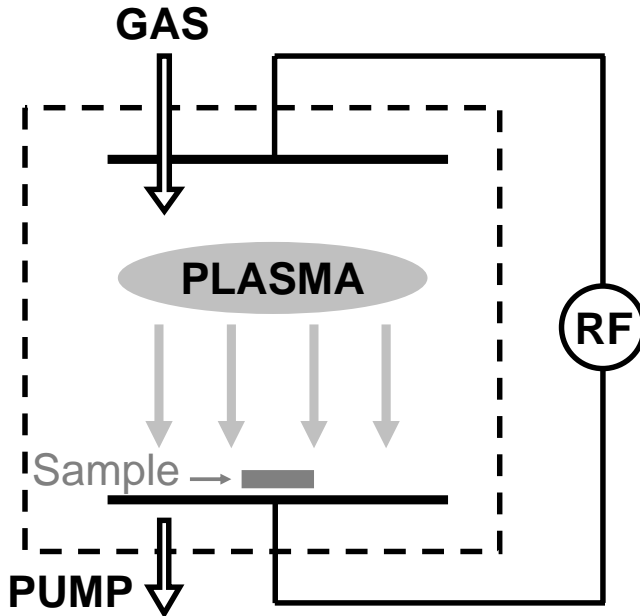
Figure 3.2: Sketch outlining the basic operating principle of RIE

etch rates can be achieved regardless of the chemical nature of the ions themselves.

In Figure 3.2 a sketch can be seen outlining the basic principle of an RIE chamber. A plasma is created in the chamber by applying a strong radio frequency field (RF-field). Interactions in the plasma are usually very complex and specific to the chemistry in the reactor. The plasma provides positive charged ions which are accelerated towards the surface due a difference in voltage between the plasma and the bottom plate.

Ideally in RIE the etching process only takes place on surfaces which the ions can actually directly reach. A mask can then be used to define structures by partially shielding the surface from the ions. The quality of the mask is usually defined by the selectivity between the masking material and the material to be etched. Usually the mask has a finite

etch rate due to sputtering by the ions. The higher the selectivity the longer a sample can be etched before the mask is etched away.

The plasma also creates a large amount of free radicals that can be adsorbed by the surface. There are usually around a thousand times more radicals then ions in RIE. In chemical etching radicals are used to directly remove surface atoms. Compared to RIE this process is isotropic and usually undercuts the mask [50].

There are several different processes that lead to anisotropic etching in RIE. Ions can either damage the surface and provide activation sites for free radicals to remove surface atom or the ions can directly remove adsorbed surface products. It is also possible for neutrals to form an adsorbed layer that inhibit the etching process. In this case the ions can sputter away the adsorbed layer and open access for radicals to etch the surface. In all three cases the anisotropy of the etch is caused by the high directionality of the ion bombardment.

Anisotropic etching can be caused by only one of the processes described above or any combination of them. The specifics are totally dependent on the chemistry used for etching.

The neutrals can not only undergo reactions in the plasma sheet but also on the sample surface, the carrier or even the chamber walls. Especially reactions with chamber walls can be problematic since etchant species can be absorbed. This usually then requires to somehow precondition the chamber prior to etching as in the case of etching InP in a CH_4/H_2 plasma [51].

The RIE used for the fabrication of the samples presented in this thesis is a parallel plate system from PLASSYS. Instead of specifying this every time when talking about the machine it will be referred to as PLASSYS from now on. It is what would be called a conventional RIE. The plates create a RF field with a frequency of 13.56 MHz which excites a plasma sheet in the center of the chamber. The bottom electrode is the lower part of the chamber while the lid is the top electrode. Ions are

accelerated perpendicular to the chamber surface and are bombarded onto the sample, which rests on a quartz plate on the bottom of the chamber.

The gases that form the plasma flow into the chamber through a small inlet in the center of the chamber lid. Pressure is regulated using a throttle valve before the turbo pump at the back end of the chamber. The quartz plate in the PLASSYS is water cooled at approximately 20 degrees Celsius. The chamber is roughly 30 cm in diameter and has a volume of circa 7 liters. The PLASSYS does not have a vacuum load lock making the use of chlorinated gases unfeasible due to their highly corrosive and toxic nature.

One of the challenges of designing an etch process in a RIE is, as with many fabrication processes, the fact that one does not have direct control over the critical process parameter. Some of these parameters for example are:

1. Density of etchants on the surface

2. Energy of impinging ions

3. Directionality of ions

4. Removal of etch byproducts

5. Temperature of the surface

This can be compared with the process parameters that can be set with the PLASSYS and their influence on the critical parameters

1. **Composition and flow of gases:** Critical for creating the etchants in the plasma. Composition of the gases influences the density of the etchants on the surface. A high flow ensures a short residence time which can lower loading effects. Composition of the gases can also lead to the creation of unwanted byproducts in the etch.

2. **Pressure in the chamber:** Due to gases having different pumping efficiencies the composition of gases in the chamber and also the density of the etchants can be influenced by the pressure. It also strongly influences the directionality and power of the ions. The lower the pressure the more energy the ions have and also the directionality improves as there will be less collisions in the plasma sheath [52].

3. **Power to the RF-field:** Influences the reactions in the plasma by providing energy. Creation of ions, radicals and neutrals is driven by the RF-field and therefore influences the density of etchants and ions in the chamber. Also mainly determines the energy of the ions and influences the directionality [52]. Ions can sputter away unwanted byproducts which is the only way of removing them if they are inert to the etching chemistry [50].

4. **Temperature of the bottom electrode:** Influences the surface temperature and can therefor strongly influence the reactions on the surface depending on the materials used. For example in the case of InP the etching with chlorine (Cl_2) can be greatly enhanced by alleviated temperatures (150-200 degrees Celsius). [53]

In an electron cyclotron resonance (ECR) RIE or ICP RIE much higher ion densities then in a conventional RIE can be reached which improves the etching and are more commonly used in fabrication of state of the art PhCs. But conventional RIE and ICP/ECR RIE are not the only etching techniques which can be used to fabricate PhCs. High quality PhC have also been fabricated using reactive ion beam etching (RIBE) [54] and chemical assisted ion beam etching (CAIBE) [55].

3.2.1   Metal organic reactive ion etching (MORIE) using methane and hydrogen

In 1986 Niggebrügge et al. reported for the first time etching of InP using a mixture of CH_4/H_2 [56]. At that time one of the major problems in etching InP was the low volatility of In in Cl_2 based etches and the highly corrosive nature of the chlorinated etch. The etch process was believed to be mostly chemical in nature due to the fact that a mixture of argon (Ar) and H_2 showed significantly lower etch rates then the CH_4/H_2 mixture although Ar is known to be an excellent sputterer.

Additional advantages of a CH_4/H_2 based etch, being reported, included smooth sidewalls, less surface roughness compared to chlorinated etches and the formation of a resistant film on the mask that enhanced the selectivity of the etch. Using less toxic etch gases is of course generally an advantage due to environmental concerns.

Niggebrügge et al. originally reported that a resistant film on the mask will also form on the InP and inhibit the etching process when the ratio of CH_4 in the gas mixture is larger then 15% [56]. Later reports by Hayes *et al.* showed that etch rates can remain stable until up to 25% of CH_4 in the gas mixture [51].

The etch process was studied in depth by Hayes et al. [51] and afterwards by Feurpier *et al.* [57, 58]. They identified methyl radicals CH_3 and hydrogen H as the most likely etchant species by identifying organic-indium species $In(CH_3)_x$ and phosphine $(PH)_3$ in the gas discharge. The most important reactions in the chamber are the following:

$$e^- + CH_4 \rightarrow CH_3 + H + e^- \tag{3.1}$$

$$3(CH_3) + In \rightarrow In(CH_3)_3 \tag{3.2}$$

$$3C_2H_5 + In \rightarrow In(C_2H_5)_3 \tag{3.3}$$

$$3H_2 + 2P \rightarrow 2PH_3 \tag{3.4}$$
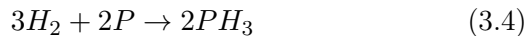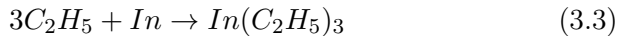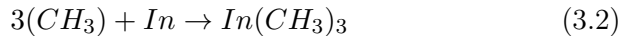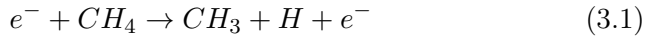
The resistant film was later identified to be some sort of polymer consisting of hydrogenated amorphous carbon (a-C:H). Earlier report

had already indicated that it was carbon rich and could be removed by oxygen indicating it to be organic [59]. During the etch the polymer layer can continually build up and cause the etch process to stop, when the it is not efficiently removed during the etch [51, 60, 50]. It can also build up on the mask and cause the pattern to become distorted [61].

The process therefore needs to be cyclic consisting of an etch step using a CH_4/H_2 plasma and a cleaning step using an O2 plasma. Ideally the cycles are independent of each other and all polymer on the sample is removed during the cleaning step.

Methyl radicals do not only play a role in the etch but also in the formation of the polymer film. The formation of hydrogenated amorphous carbon (a-C:H) films has been studied by Morrison et al. for CH_4 plasma in ECR RIE. The precursors for the film growth in the plasma were identified to be H^+, C^+, CH^+, CH_2, CH_3^+ and C_2 [62]. There seems to be a complex interplay between the polymer film on the surface and the etch process since the same radical which is necessary for etching also causes the build up of the polymer.

The etch process is dependant on the concentration of methyl radicals but needs ion assistance for etching. At low concentrations of CH_4 the surfaces show signs of severe phosphine depletion and formation of droplets of In indicating that the etch rate is limited by diffusion of methyl radicals to the surface. It is not limited by the ion energy flux since larger concentrations of CH_4 will decrease the ion energy flux but increase the etch rate [58]. The removal of P is dependant on the density of hydrogen and the energy of the impinging ions which is usually not the limiting factor in the etch.

Little work has been done to study the reactions for GaAs etching in a CH_4/H_2. Henry *et al.* have speculated that also in this case methyl radicals are most likely the etchants species [63]. Generally the CH_4/H_2 chemistry is difficult to work with and a poor choice for etching GaAs due to low etch rates [56]. This will be further outlined in section 3.5.

A far more favorable chemistry for etching GaAs are chlorinated gases which can also be used for etching InP [53].

Another issue with using CH_4/H_2 is that the etch rates are very low for compounds containing Aluminium [63]. It is therefor extremely difficult to etch for example InAlAs or AlGaAs. Both compounds are used as sacrificial layer in different wafers presented here. The problems of not being able to etch into the sacrificial layer when releasing the membrane will be further explained in section 3.6.1 and 3.6.2.

3.2.2   Etch quality

The goal of RIE is an anisotropic etching of a given structure. The quality of an etch can therefore be measured by looking at the angle of the sidewalls in the etched structures. The more vertical the sidewalls are the more anisotropic the etch is.

It becomes harder to achieve vertical sidewalls the higher the aspect ratio becomes. The aspect ratio is defined as the ratio of the depth of the etch to the size of the opening of the structure that was etched. For example for a hole this would be the depth of the hole over the diameter of the hole.

Another important factor is the quality of the sidewalls. For applications in photonics especially when fabricating PhC or WGs it is very important to have smooth sidewalls. Rough sidewalls lead to higher losses and are generally detrimental to the optical properties of the device [64, 65].

Etching PhC membranes usually does not require very high aspect ratios since the thickness of the membrane is usually comparable to the hole size in order to achieve confinement of the order of the wavelength in all directions which puts the aspect ratio close to one. It might be advantageous though to etch into the sacrificial layer underneath the membrane requiring higher aspect ratios which will be further outlined in section 3.6.1 and 3.6.2.

For etching PhC membranes it is therefore mostly important to make sure that the side walls are smooth and vertical. An angle close to 90 degree is usually required when etching PhC. It has been shown theoretically that non vertical sidewalls lead to higher loses due to out of plane scattering and scattering from TE to TM modes [66].

The additional losses due to non-straight sidewalls are expected to be below 3 dB/mm if the inclination angle remains less then 4 degrees different from 90 degrees. This result was obtained for calculations on PhC WGs [66]. These results cannot be directly transferred to PhC cavities but show the importance of straight sidewalls in PhC.

As will be seen in section 3.5.1 the sidewalls in the GaAs are not perfectly straight which presents a source of extra losses and possibly limits the Q factors that can be achieved.

3.2.3   RIE Lag

A more important aspects of RIE of PhC is RIE lag. RIE lag is the name for several mechanism which all cause a drop in etch rate with increase in aspect ratio. The aspect ratio increases during the etch as the etch depth increases.

Mechanism proposed to cause RIE lag include ion shadowing, neutral shadowing, differential charging and Knudsen neutral transport [67]. Which mechanism causes RIE lag is largely dependent on the etch chemistry used and the processes taking place in the etching chamber.

Earlier works on etching trenches and pillar on the same RIE machine have identified ion shadowing as a possible limiting factor in the etch rate with high aspect ratios [61].

Ion shadowing is caused by the fact that not all ions travel perfectly perpendicular to the surface. From simple geometric considerations this leads to a rather simple conclusion which is depicted in figure 3.3.

The less obstructed the access to the surface is the higher the etch
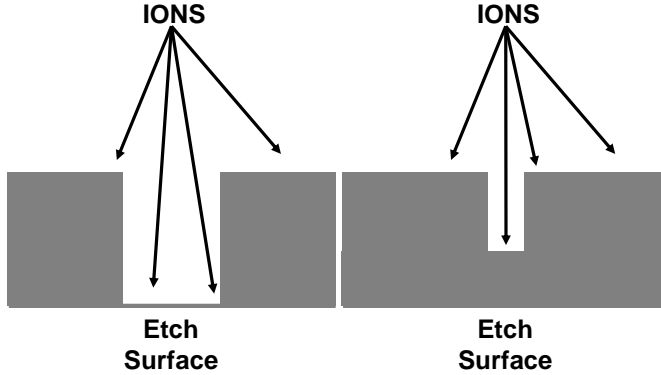
Figure 3.3: Simple representation of the effect of ion shadowing in etching small feature sizes

rate is. When going to higher aspect ratios the etch will at some point become very slow due to the fact that more and more ions are blocked.

The energy and angular distribution of the ions (IED and IAD, respectively) of an argon plasma have been measured by Liu et al. for various pressures and biases [52]. Hardly surprising the lower the pressure and the higher the power the more narrow the IAD becomes and the more peaked.

For a pressure of 10 mTorr and a peak-to-peak voltage of 130 V the distribution angle is around 13 degree. Assuming a hole with a diameter of 150 nm that would mean that the center of the hole would see a significant ion shadowing effect at an etch depth of around 660 nm

$$\frac{d_{hole}}{2\tan\frac{IAD}{2}} = \frac{75}{\tan 6.5°} \approx 660\,nm \qquad (3.5)$$

This actually indicates that ion shadowing is not the reason for RIE lag in the PhC structures described here. Etching PhC holes in GaAs smaller then 150 nm was very challenging due to a drop in etch rate. The holes successfully etched are 160 nm deep with 200 nm of Si_3N_4 on top as a mask. The maximum distance between the top and the bottom

of the hole would therefore be 360 nm. This is a significantly shorter distance then the 660 nm calculated for the ion shadowing effect which means that the holes would not suffer significantly from ion shadowing even when taking into account that the actual IAD in a CH_4/H_2 plasma might differ from an Ar plasma. The voltage between the plasma and the bottom electrode is around 500 V for the optimized process described later which means that the IAD should actually be better then .

Since the etchants in the MORIE etch are neutral methyl radicals, neutral shadowing could be the cause. Neutral shadowing is similar to ion shadowing but since the atoms are neutral they are not accelerated to the surface and have a much wider spread of angels.

This can become especially a problem in enclosed structures like narrow trenches or small holes. The smaller the structure the more difficult it becomes for the etchants to diffuse to the surfaces that need to be etched which would explain why the problem is more severe for etching holes then open trenches.

Two different studies have been carried out on comparing systematically the effect of RIE lag in etching InP based PhC between a conventional RIE using $CH_4/H_2/Ar$ and a CAIBE using Cl_2/Ar. The first study by Mulot *et al.* concluded that deep etching of PhCs is not possible using RIE with $CH_4/H_2/Ar$ but sufficient to etch thin membranes as is the case here [55]. They showed that RIE lag was still affecting even the largest holes they measured on with diameters of 490nm.

A second more quantitative study by Berrier et al. showed that the critical aspect ratio for etching PhC is 20-25 times larger when using a CAIBE using Cl_2/Ar compared to a RIE using $CH_4/H_2/Ar$ [68]. Both studies concluded that a CAIBE is to be preferred when etching PhCs.

This underlines the importance of paying close attention to the aspect ratio when etching PhCs. Optimization of the etch process was therefor done on small holes to ensure that the process would work on all PhC independent of the filling factor chosen. All of the etch rates presented

in this thesis were measured on PhC patterns with holes with a diameter of 160-200nm.

3.3   Wafer description

All the wafers used for the fabrication of PhC slabs presented in this thesis were grown epitaxially. In order to investigate the properties of PhC cavities with QDs as active material, GaAs membranes with InAs/GaAs QDs were grown by molecular beam epitaxy (MBE) using the Stranski-Krastanov (SK) growth method. The dots used were emitting at around $\sim 1\ \mu$m. Table 3.2 and 3.3 shows the layer structure of the wafers NBI187 and TUM01, respectively. Both wafers were used in the fabrication of the PhC presented in chapter 4. Al_xGaAs was used as sacrificial layer with an aluminium content of $x = 0.65$ and $x = 0.7$ percent, respectively. InAs/GaAs QDs were chosen since their fabrication is fairly standard nowadays [36] and there is a lack of QDs with high optical quality at long wavelengths in the InP system. Only a handful of research groups have managed at all to fabricate InAs QDs on InP with an emission wavelength of $\lambda \sim 1.55$ at room temperature [69, 70].

For the telecommunication wavelength region ($\sim 1.5\ \mu$m) wafers were grown by metal organic vapor phase epitaxy (MOVPE) on InP substrate. Table 3.1 shows the layer structure of the wafers used for carrying out the optical experiments in the long wavelength region. The InP cap layer is used to avoid surface damage during the fabrication process. It is removed during membranization together with the sacrificial layer. The membrane consist of InGaAsP ($Q = 1.15$) lattice matched to InP with ten InGaAsP QWs ($\lambda = 1.52$) embedded as active material for optical pumping. The sacrificial layer consists of InP and InAlAs with InGaAs underneath as an etch stop layer. The need for the multilayer structure of the sacrificial layer is explained in section 3.6.2. The structures in the InP system were grown on a (100) InP substrate in a vertical low-pressure

Layer	Component	Thickness [μm]	Notes
cap	InP	0.02	to be etched away
membrane (top)	In$_x$GaAs$_y$P	0.097	$x = 0.77$ $y = 0.503$
barrier	In$_x$GaAs$_y$P	0.0043	$x = 0.49$ $y = 0.86$ 10 times
QW	In$_x$GaAs$_y$P	0.006	$x = 0.75$ $y = 0.86$ 10 times
barrier	In$_x$GaAs$_y$P	0.0043	$x = 0.49$ $y = 0.86$ 10 times
membrane (bottom)	In$_x$GaAs$_y$P	0.097	$x = 0.77$ $y = 0.503$
sacrificial	InP	0.1	
sacrificial	InAlAs	0.1	
sacrificial	InP	0.8	
etch stop	InGaAs	0.05	
buffer	InP	0.5	
substrate	InP	350	

Table 3.1: Layer structure of wafer D211: 340nm thick InGaAsP membrane (Q=1.15) with 10 QWs (λ =1.52) and 1 μm sacrificial layer. Grown in a MOVPE reactor at DTU Danchip.

MOVPE system using hydrogen as a carrier gas at a work pressure of 60 Torr. Standard trimethyl precursors for the group III elements and arsine, phosphine and tertiarybutylphospine for the group V elements were used.

MOVPE and MBE are standard processes in modern semiconductor fabrication and well documented in the literature. They allow to grow materials with high optical and crystalline quality. Thicknesses of individual epitaxial layers can be controlled with a precision of single

Layer	Component	Thickness [μm]	Notes
membrane (top) (top)	GaAs	0.08	
dots	InAs	2.13 monolayers	30sec growth interrupt
membrane (bottom)	GaAs	0.08	
sacrificial	Al$_x$GaAs	1	$x = 0.706$
buffer	InP	0.1	
substrate	InP	500	

Table 3.2: Layer structure of wafer NBI187: 160nm thick GaAs membrane with 1 layer of InAs QDs (250 dots per μm^{-2} [71]) and 1 μm AlGaAs sacrificial layer. Grown in a MBE reactor at the Copenhagen University.

monolayers. An important design choice is the thickness of the layer that will later in the process become the membrane since it is an important parameter in creating a bandgap in a PhC. Bandgap calculations can be found in section 2.1.2.

3.4 Masking methods

3.4.1 Optimization of SiO$_2$ and Si$_3$N$_4$ as a hard mask

The first step in optimizing the hard mask is to decide on its thickness. Depending on the thickness of the hard mask the thickness of the e-beam resist needs to be adapted. As outlined in section 3.2 the mask should ideally be as thin as possible to minimize effects like RIE lag. On the other hand the mask needs to be sufficiently thick to not erode during the etch which would otherwise spoil the pattern. RIE of Si$_3$N$_4$ and

Layer	Component	Thickness [μm]	Notes
membrane	GaAs	0.04	
dots	InGaAs	7 monolayers	5sec growth interrupt
membrane	GaAs	0.04	
dots	InGaAs	7 monolayers	5sec growth interrupt
membrane	GaAs	0.04	
dots	InGaAs	7 monolayers	5sec growth interrupt
membrane	GaAs	0.04	
sacrificial	Al$_x$GaAs	1	$x = 0.65$
substrate	GaAs	500	

Table 3.3: Layer structure of wafer TUM01: 160nm thick GaAs membrane with 3 layers of InGaAs QDs (high density) and 1 μm AlGaAs sacrificial layer. Grown in a MBE reactor at the Technical University of Munich.

SiO_2 is a well known process that is described in almost any standard textbook. Etch rates for RIE of SiO_2 and Si_3N_4 in a CHF3/O2 plasma can be found here [72].

Different mask thicknesses of 100nm of SiO_2, 100nm of Si_3N_4 and 200nm of Si_3N_4 were used to optimize the fabrication process. The effects of these different thicknesses and materials are evaluated in section 3.5.1. The reason for the spinning a thick layer of ZEP is explained below.

ZEP 520A which is commercially available, was used as e-beam resist. ZEP 520A can be spun in various thicknesses. The thickness of the layer is dependant on the parameters of the spinning (spin speed, acceleration and spin duration) and the viscosity of ZEP 520A. Anisol (methoxybenzene) can be used to dilute ZEP and decrease its viscosity. Wafers were routinely baked after the spinning for two minutes at 130 degree Celsius to dry the resist which increases resolution as well as makes the resist stick better to the surface [73].

The development process has influence on the final hole sizes. Since the development is not the only factor influencing this but also both the etch of the hard mask and the III-V etch, the effects are separately evaluated in Appendix A.

The reason for using SiO_2 or Si_3N_4 as a hard mask instead of directly etching the GaAs/InP becomes apparent when looking at figure 3.4. As can be seen the ZEP is strongly deformed during the III-V etch spoiling the PhC pattern.

It is therefore necessary to use a different masking material to etch the GaAs since it cannot be directly etched using ZEP as a mask. SiO_2 and Si_3N_4 are both grown by PECVD. Thicknesses were measured by using an elipsometer and fitting the curves using a cauchy model. The calculated refractive index of the Si_3N_4 was around 2.

Figure 3.5 shows an example of a bad SiO_2 etch. It shows several of the challenges of etching glass with ZEP as a mask material using CHF_3 and O_2.
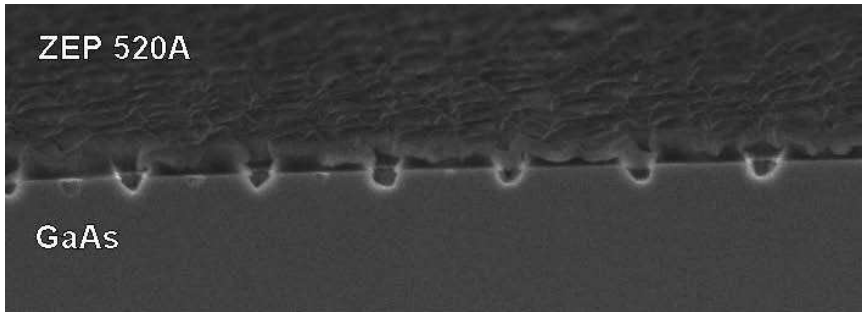
Figure 3.4: Cleaved side view of holes etched into GaAs using only ZEP 520 A as mask. GaAs was etched using CH_4 and H_2.

The top part of the ZEP looks burned or for a lack of a better word "foamy". The foam is far more difficult to remove than standard ZEP and seems to be chemically mostly inert. The structures in the figure 3.5 are PhCs. Even though the pattern is not very well visible due to the foaming it can be seen from the top view that the foam has formed little rings with the approximate same size as the patterned holes. This indicates that the reaction is strongest at the edges of the pattern were more of the resist is directly exposed to the ion bombardment from the plasma.

Between the foam and the glass unburned ZEP still remains. This is important later when trying to remove the resist. The holes in the SiO_2 shown in figure 3.5b are of poor quality. The sidewalls have an inclination of almost 45 degrees and are far away from being vertical. This is only of minor interest here since the picture merely serves to show the problem arising from severe erosion of the ZEP. It is also clear that the mask erosion will degrade the quality of the etch.

The foam partly covers areas which are supposed to be exposed to the plasma. While this probably does not completely stop the etch it is obvious that it will introduce irregularities to the hole shape. For best possible performances disorders in PhC needs to be kept to a minimum.
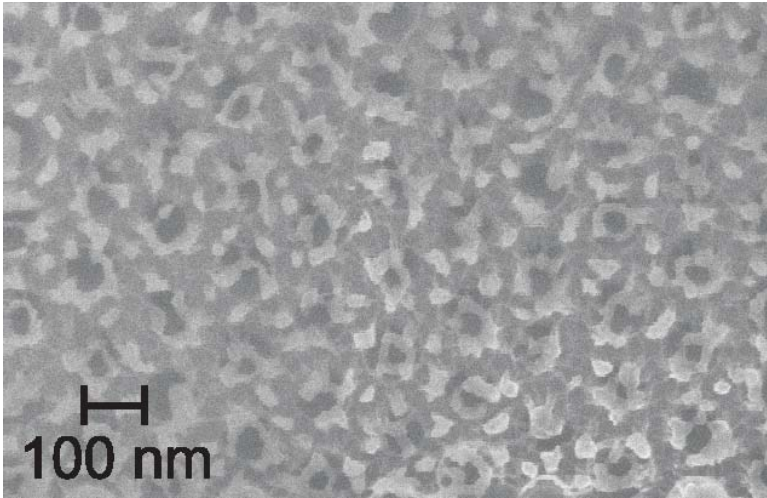
(a) Top
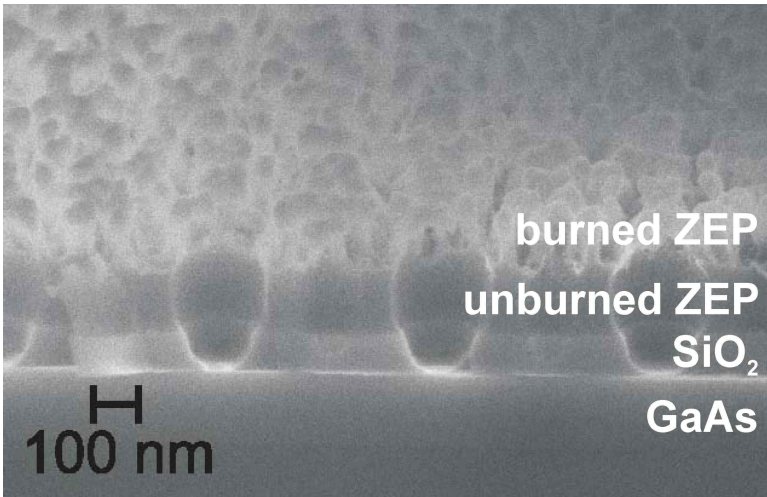
(b) Cleaved side

Figure 3.5: PhC pattern etched in SiO$_2$ for 3:32 min with high O$_2$ ratio (2 sccm O$_2$/ 16 sccm CHF$_3$) and high power (60 Watt)
.
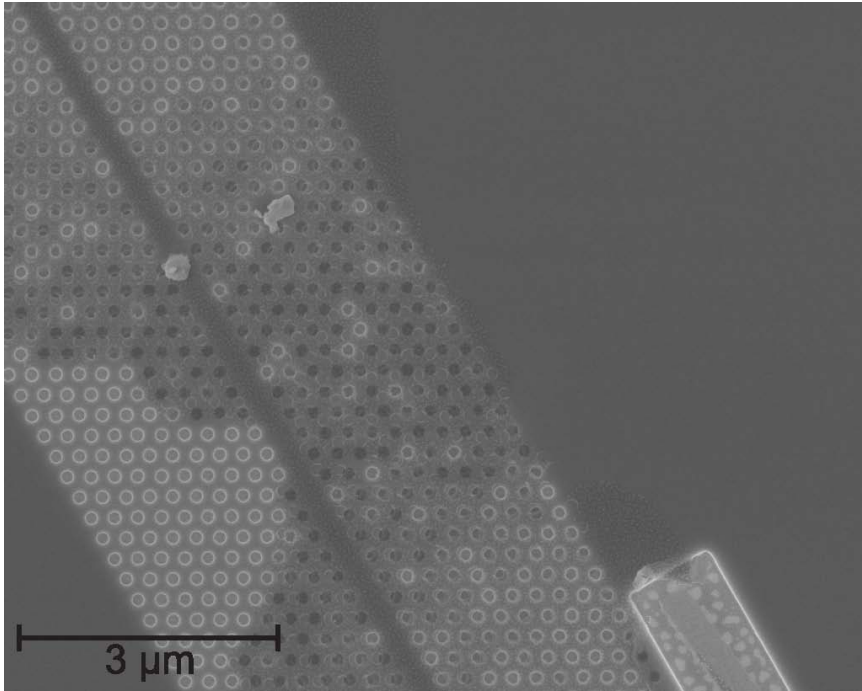
Figure 3.6: ZEP sticking to the SiO$_2$ hard mask surface of a PhC WG pattern.

The foam makes it difficult to define an exact selectivity between glass and ZEP. Since the foam is unwanted, hard to remove and not isotropic it will be treated as a different material in this regard. This means that the selectivity is defined as the ratio of the thicknesses between the unburned ZEP and the glass. This is not very accurate because it is hard to tell where to exactly draw the line between burned and unburned ZEP since there is no clear separation. As already mentioned the foam is hard to remove and it is therefor important to make sure it doesn't touch the glass.

It is standard when calculating the etch time for a structure to use a sufficient thick layer of resist. The selectivity can be used as a guide
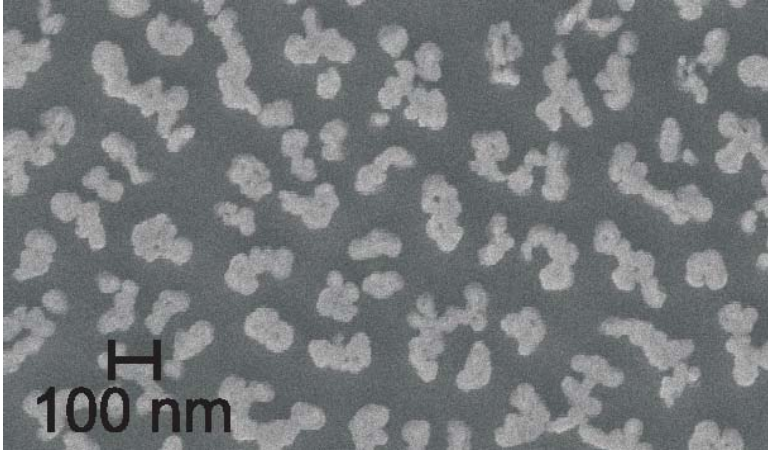
Figure 3.7: Attempted ZEP removal by first placing the sample in heated Remover 1165 (70 degree C) and then using a high power oxgyen plasma (100 W) for several minutes. Burned remains of the ZEP still present (white crumbles).

for this. Due to the problem with the foam it should be mentioned that it is advisable to leave a certain error margin of around 50nm of ZEP to make sure that the foam is sufficiently separated from the glass surface. Otherwise it might happen that it will stick to the surface. An example of this can be seen in figure 3.6.

After the etch the left over ZEP is stripped using microposit remover 1165. It is crucial to make sure that the sample is in a vertical position when removing the resist because otherwise the burned ZEP will stick to the surface. Unfortunately no chemical way of removing the burned ZEP was found. In order to show how hard it is to remove ZEP after it sticks to the surface a sample was placed flat in heated remover 1165 (70 degree C water bath with low ultrasound) for two hours and treated afterwards with a high power oxygen plasma (100 W) for several minutes in the Plassys . Despite this intense cleaning remains of the ZEP mask

are still visible as can be seen in figure 3.7. Unburned ZEP though can be efficiently removed in an oxygen plasma.

As a reminder it is useful to sum up the requirements regarding the mask etch that have been described so far:

1. ZEP deforms in the III-V etch and needs to be removed before etching can continue.

2. Sidewalls in the mask need to be straight to provide the best possible mask in the next etch step.

3. Foaming needs to be kept to minimum to ensure good pattern transfer.

4. Foam should not touch the surface so that it can be efficiently removed.

In order to find optimal etch parameters for the glass etch, several etches were done and compared to each other. The parameters varied are listed below.

1. Partial Flow CHF_3 (constant at 17 sccm)

2. Partial Flow O_2 (1.6-2 sccm)

3. Pressure (10-30 mTorr)

4. Power (60-90 W)

In a first round all etches were done for 2 minutes on a GaAs wafer with a 100nm thick SiO_2 layer and 400nm ZEP 520A e-beam resist. The sample was prepared in the same way as described in the beginning of the GaAs membrane recipe in appendix C. The pattern written by the e-beam consisted of a PhC with small holes designed to be 120nm in diameter. It was cleaved afterwards and inspected in the SEM. The first round was used to measure the etch rate of each parameter set. In a

Sample	CHF$_3$/O$_2$ [sccm]	Pressure [mTorr]	RF Power [W]	ZEP left [nm]	Etch rate $[\frac{nm}{min}]$	Selectivity	Angle [deg.]	Etch time [s]
1	17/1.6	10	60	223	29	0.3	67	233
2	17/1.8	20	75	191	32	0.3	68	212
3	17/2	30	90	156	37	0.3	62	186
4	17/2	10	60	207	31	0.3	62	220
5	17/2	30	60	193	28	0.3	60	241
6	17/2	10	90	189	37	0.3	71	185
7	17/1.6	30	90	177	32	0.3	66	215
8	17/1.6	30	60	211	28	0.3	70	242
9	17/1.6	10	90	176	35	0.3	65	195

Table 3.4: Selectivity, verticality and etch rate of a SiO$_2$ PhC hole etched in a RIE using a CHF$_3$/O$_2$ plasma for various process parameters

second round the same parameters were used to etch an identical set of samples but the etch time was adjusted to etch through the SiO$_2$ layer. The results of all etches are summarized in Table 3.4.

Looking at Table 3.4, it is apparent that the selectivity of the etch does not change significantly with varying parameters. Both the SiO$_2$ as well as the ZEP are effected equally by the changes in the parameters in terms of etch rates.

Also the overall change in sidewall inclination is not very large. Comparing the two best results sample number 6 and number 8 show two completely opposite sets of parameters in terms of amount of oxygen, power and pressure.

SEM pictures of both samples are shown in figure 3.8. Since both selectivity and sidewall inclination are almost identical for both samples,
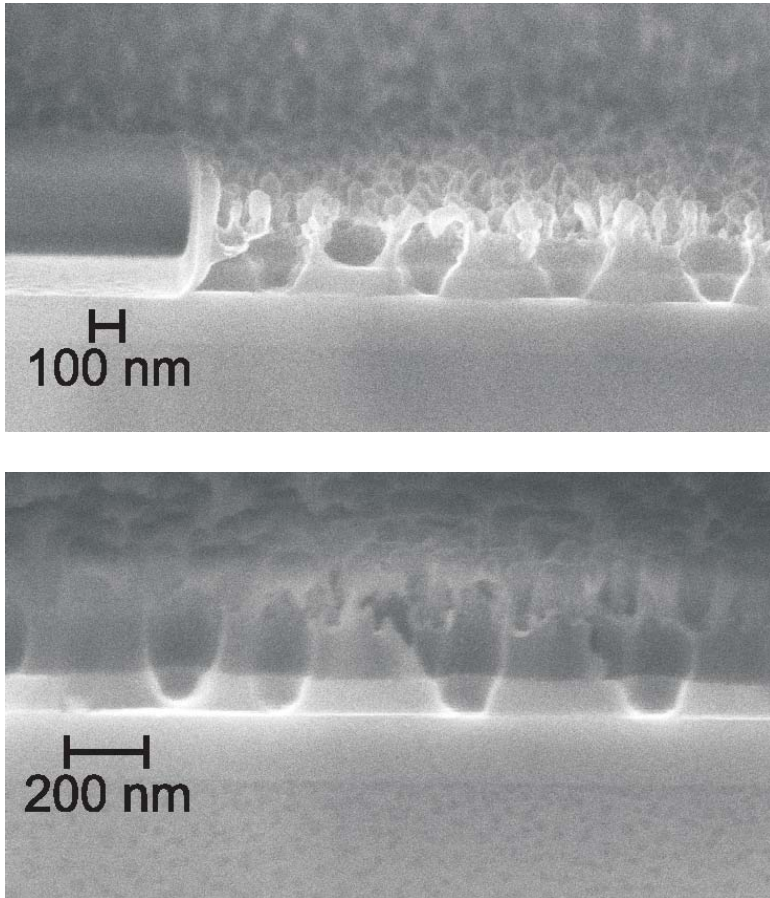
Figure 3.8: Side view of PhC pattern etched in SiO_2 Top: High power and high O2 ratio - Bottom: Low power and low O2 ratio.

the quality of the ZEP layer becomes the decisive factor for determining the optimal etch parameters.

As was outlined before it is important to keep the amount of burned ZEP to a minimum. The two etches shown in figure 3.8 represent two extremes in the parameter space. On the left hand side an etch with a high amount of oxygen and a large bias is shown while on the right hand side an etch with a low amount of oxygen and a low bias is shown. The effect is apparent. The ZEP layer of the sample on the left hand side is more burnt then the ZEP layer of the sample on the right hand side, leading most likely to a larger distortion of the pattern.

This shows clearly that the ZEP becomes more burnt with increasing power and oxygen content. It would have been interesting to test how much the oxygen content could have been lowered further before the etch stops. Unfortunately, due to technical constraints of the machine used, reproducible flows could only be achieved until around 1 sccm. Using no oxygen in the chemistry completely stopped the etch.

So far only results using SiO_2 have been shown. As already mentioned in the beginning of the chapter not only SiO_2 was used as a hard mask but also Si_3N_4. The main problem in etching SiO_2 was identified to be the deformation of the ZEP layer. This effect is of course independent of the layer underneath and therefor not the same amount of etches have been done using Si_3N_4 instead of SiO_2. Table 3.5 shows the result of two different Si_3N_4 etches.

First of all Si_3N_4 has a better selectivity then SiO_2 towards ZEP in this etch. This allows for thicker masking layers to be used in the next etch step. Sample number 1 in table 3.5 presents the best etch found and was included in the standard process to fabricate the PhC presented in this thesis. The result can be seen in figure 3.9. The sample was slightly overetched to improve the verticality of the sidewalls.

Sample	CHF$_3$ [sccm]	O$_2$ [sccm]	Pressure [mTorr]	RF Power [W]	ZEP left [nm]	Etch rate rate $[\frac{nm}{min}]$	Selec- tivity
1	15	1	10	13	266	17	0.9
2	15	1	10	30	186	33	0.6

Table 3.5: Selectivity and etch rate of a Si$_3$N$_4$ PhC hole etched in a RIE using a CHF$_3$/O$_2$ plasma for two different sets of process parameters

In conclusion, it was shown that when etching ZEP in an conventional RIE, using CHF$_3$ and O$_2$, foaming is an issue which can be best avoided by using a low flow of oxygen and low power. An optimal recipe for etching Si$_3$N$_4$ was found.

3.5 Optimization of RIE etching III-V semiconductors using CH$_4$ and H$_2$

3.5.1 Cyclic CH$_4$/H$_2$ etch with O$_2$ cleaning steps

As mentioned before CH$_4$/H$_2$ is a poor chemistry to etch GaAs and difficult to work with. It works better when etching InP and can also be used for etching all tertiary or quaternary alloys containing In, Ga, As and P. The etch rate decreases with higher amounts of Ga and increases with higher amounts of In [51, 59].

As mentioned before the chamber needs to be cleaned during etching to avoid the build of polymer. The etch step and the cleaning step are unfortunately not independent from each other. The main problem in optimizing the etch therefore are the large number of parameters that can be varied, which are listed below.

1. Ratio CH$_4$:H$_2$

2. Total flow (CH$_4$ H$_2$)
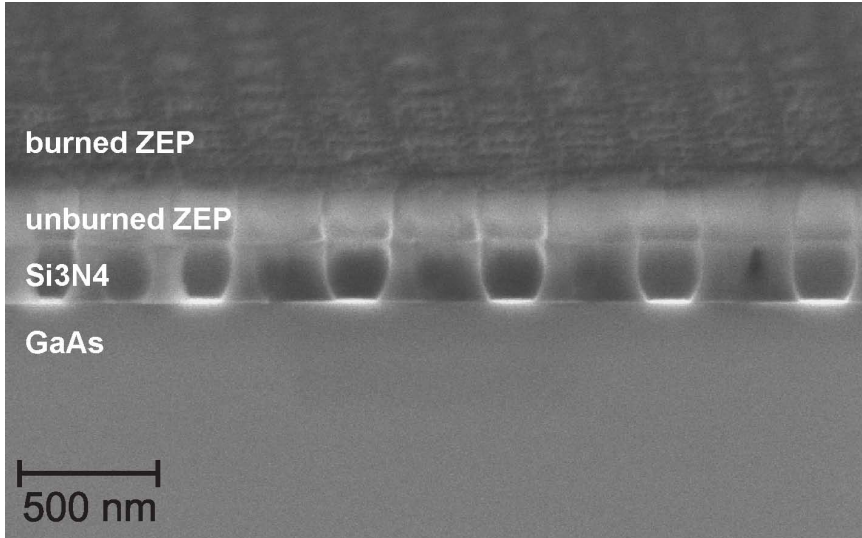
Figure 3.9: Cleaved side view of holes etched into 200nm of Si_3N_4 using an optimized etch recipe with low power low O2 ratio for 16 minutes.

3. Pressure during etch step

4. RF power during etch step

5. Etch time per cycle

6. Pressure during cleaning step

7. RF power during cleaning step

8. Cleaning time per cycle

9. Preconditioning of the chamber

10. Thickness and choice of masking material

Due to the formation of polymer during the etch it is very important to precondition the chamber prior to using it for etching [51]. The

chamber walls will absorb etchant species and without preconditioning the etch rate will be greatly inhibited. This problem is not specific to the CH_4/H_2 chemistry. For all the etches presented in this thesis a separate recipe was used to precondition. It uses the same chemistry as in the etch step but without the cleaning steps in between and runs for 10 minutes.

Due to the large number of parameters it is difficult to present all the results obtained during the optimization. Instead the factors that contributed most in optimizing the etch will be presented here in the following order: CH_4/H_2 ratio, oxygen plasma cleaning step, choice of carrier, mask thickness and pressure. Another problem due to the large parameter space is to find a global optimum. Although a lot of parameters were varied the optimum presented here is likely not the global optimum. The main goal was to find a recipe that is able to fabricate PhC of sufficient quality for optical experiments.

CH_4/H_2 ratio

As was discussed in section 3.2 the ratio of CH_4 to H_2 has a large influence on the etch rate [51, 59, 60]. Figure 3.10 shows that with increasing amount of CH_4 the etch rate increases.

Oxygen plasma cleaning step

Cleaning the samples in between etch steps also cleans the chamber walls. Excessive cleaning steps can therefor also inhibit the etch rate if the amount of polymer removed from the chamber walls leads to too much absorption of radicals during the etch steps. Another effect is that the oxygen plasma can also damage the Si_3N_4 mask due to sputtering by ions reducing the selectivity of the etch. This effect is shown in table 3.6. All other etch parameters are identical but "cyc b" has a more aggressive (higher RF power and lower pressure lead to larger chamber bias) and longer cleaning step. As a result the etch rate drops since the polymer is removed from the chamber walls during the etch.
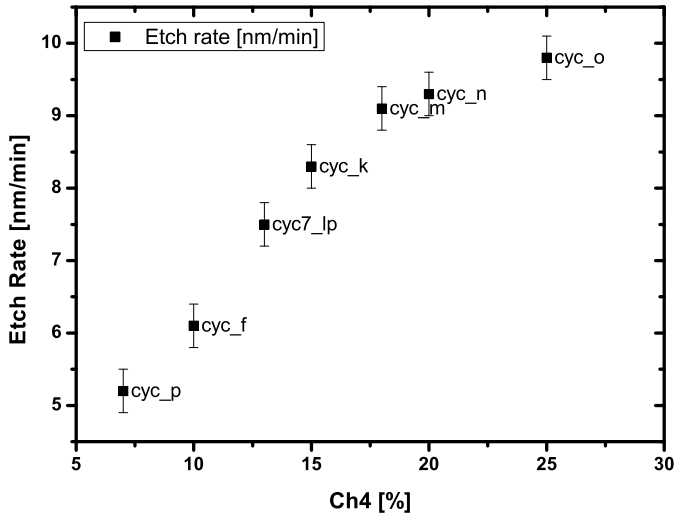
Figure 3.10: Etch rate vs. CH$_4$ ratio for low pressure etches with p=20 mTorr. All other process parameters can be found in appendix C. Etch rates were measured on PhC patterns in GaAs.

Choice of carrier

An interesting result which was obtained when etching GaAs was that the choice and size of carrier material underneath the sample can have a large influence on the etch rate. Usually the carrier should be passive during the etch. In this case the etch rate of GaAs could be increased by using a quarter of a two inch InP wafer. Table 3.7 shows the etch rate for different carriers. The same recipe was used for all four etches.

A drastic example for this behavior can be seen in figure 3.11 showing an etch attempt in which the sample was placed directly on the quartz plate of the chamber. The picture shows an unsuccessful etch of a PhC

recipe name	duration per cycle (cleaning) [min]	RF power (cleaning) [W]	pressure (cleaning) [mTorr]	etch rate (GaAs) $[\frac{nm}{min}]$
cyc a	0:30	20	150	2.9
cyc b	1:00	60	50	0.7

Table 3.6: Changes in etch rate using different parameters for the cleaning step in the MORIE

Carrier	etch rate (GaAs) $[\frac{nm}{min}]$	[CH$_4$ of total flow] [%]
no carrier(Quartz plate)	none (see figure 3.11)	13
2 inch GaAs wafer	6.1	13
2 inch GaAs wafer	2.9	5
2 inch InP wafer	7.5	13
2 inch InP wafer	5.8	6
1/4 2 inch InP wafer	8.9	13

Table 3.7: Changes in etch rate using different sizes and materials of carriers in the MORIE

pattern. On the top the remains of the SiO2 mask can be seen with the GaAs membrane (light grey) and the AlGaAs sacrificial layer (dark grey) underneath. Instead of holes in the GaAs the openings in the mask are filled with left over polymer created during the etch process (dark grey).

Placing material underneath the wafer that consumes etchants should actually result in a drop of etch rate. In this case it causes the opposite as can be seen from table 3.7. It is even more surprising that by using a wafer with a material different from the one being etched in the chamber the etch rate can be further increased. The reason is most likely the complex interplay between etching and polymer formation in the etch.

As was discussed in section 3.2 CH_3 plays a pivotal role in the etch and also participates in the polymer formation. Placing the wafer underneath probably shifts the ratio of CH_3 radicals to ions in the plasma and leads to a decrease in polymer formation without decreasing the etch rate in the same way.

This effect is different from lowering the total ratio of CH_4 as can also be seen in table 3.7 by comparing samples etched on the same carrier with different amount of CH_4 in the etch chemistry with each other.

There is a limit to the size of the carrier that is useful though. At some point load effects set in and the etch becomes limited by the amount of radicals available and not the formation of polymer. By reducing the size of the carrier from a full 2 inch to a quarter of that, the etch rate can be further increased. The exact size needed for the optimal etch rate is hard to determine since it probably depends on the amount of material etched during the process. The size of all samples shown in table 3.7 is roughly 1x1 cm in size with similar patterns being etched. A quantitative study would be needed but in this case it was sufficient to use the values obtained as a rough guideline since the size didn't differ much from sample to sample.

Mask thickness

As outlined in section 3.4.1 Si_3N_4 was chosen as masking material for the
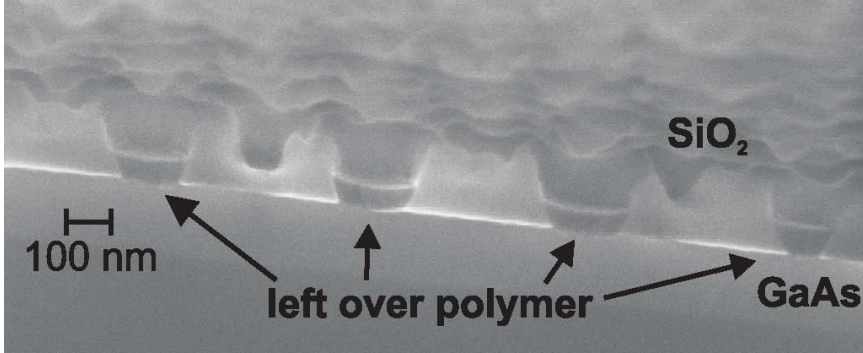
Figure 3.11: MORIE etch of a PhC pattern in GaAs using a SiO2 hard mask. Sample was placed without carrier directly on the quartz plate of the RIE

recipe name	mask thickness [nm]	sidewall inclination [degree]
cyc 8	100	95
cyc 8	200	92

Table 3.8: Verticality of PhC holes etched in GaAs using different mask thicknesses

etch since it had a better selectivity then SiO_2. Masks with two different thicknesses were tested using Si_3N_4 as masking material. Increasing the mask thickness improved sidewall inclination as can be seen in table 3.8. The etch rate of the mask during the cyc8 program was ~1.3 $\frac{nm}{min}$. The mask close to the patterns gets etched much faster though and the photonic crystal pattern will be spoiled due to the mask giving way around the rim of the holes long before it is completely etched away. The maximum etch time is therefor around 40 minutes (16 cycles for 2.5 min each).

Pressure

Considerable amount of time was used to try to improve the verticality of the sidewalls in the etch by lowering the pressure. Although etch rates and sidewall inclinations comparable to those at higher pressure were achieved as can be seen in appendix C there was no improvement. This might be linked to the fact that the etch rate is mostly limited by the CH_3 flux to the surface and not the ion energy flux as outlined in section 3.2. Reducing the pressure will cause the IAD to be smaller and increase the ion energy flux to the surface. It will also indirectly affect the density of CH_3 in several ways (modification of gas flow and gas composition in the chamber) but not necessarily in a beneficial way.

This doesn't indicate that any adverse effects will result from lowering the pressure. It rather indicates that the pressure might not be as important in this process as in many others when it comes to the verticality of the side walls in the etch.

Conclusion

The results obtained so far are summarized below. The examples shown here represent the changes that had the largest impact on improving the etch apart from the change in pressure which is still interesting by itself. Previous works on the same chamber had already resulted in showing that the optimal power for the etch is around 60 Watt [61].

1. The etch should have a moderate ratio of CH_4/H_2 ($\sim 20\%$)

2. The cleaning step needs to be long enough to remove the polymer build up on the sample but not too long

3. The choice of carrier material can influence the etch rate.

4. Due to the low selectivity between the etch material and mask material increasing the mask thickness is beneficial to sidewall inclination.

The recipe giving the best results for etching GaAs had the following parameters:

1. Carrier: quarter of a 2 inch InP piece

2. Etch step: 2:30min / 60W RF power / 50 mTorr chamber pressure / 33.6 sccm H_2 / 8.4 sccm CH_4

3. Cleaning step: 0:30min / 20W RF power /150 mTorr chamber pressure / 50 sccm Oxgyen

4. Etch rate: 9 $\frac{nm}{min}$ (GaAs) / 22 $\frac{nm}{min}$ (InGaAsP) / 30 $\frac{nm}{min}$ (InP)

As mentioned in section 3.2 RIE lag can severely influence the etch rates during RIE. The etch rates presented for various recipes in this chapter were measured on large PhC patterns with holes between 120-250nm in diameter. Using the same processes to etch for example trenches or large openings will yield higher etch rates.

There is a limit to how small the holes can be made. Both the etch rate in the mask etch and in the MORIE will start dropping significantly when holes become smaller then 150nm in diameter. Unfortunately there is no sharp drop off as the etch rate will start to vary from hole to hole resulting in an irregular pattern.

All the different recipes that were used in trying to optimize the etch can be found in appendix C. Another important, issue not mentioned so far, is general cleanliness and reproducibility when optimizing a process. Memory effects are well known in RIE and it cannot be stressed enough how pivotal it is to always prepare the chamber in the same way before trying a new recipe. Therefor before doing a new etch the chamber was cleaned and preconditioned every time prior to etching.

Most of the optimization was done on etching GaAs. This happened purely for historical reasons because the first samples that could be obtained for optical experiments were InAs dots in a GaAs membrane. Probably the optimized etch would have been slightly different when

the process would have been optimized on InGaAsP or InP. Fortunately the same process also worked very well on these materials and could be used without further optimization. A summary of the results for the optimized recipe can be found in the following section 3.5.2.

3.5.2   Results for photonic crystal patterns in GaAs and In-GaAsP

In the previous section the optimization of the etch procedure was explained in detail. The following chapter will show the results of using the optimized recipes to etch PhCs in GaAs and InGaAsP.

The RIE etch rate of GaAs using a CH_4/H_2 plasma was estimated to be around 9 nm per minute. The left hand side of figure 3.12 shows the result of the optimized GaAs etch.

The etch rate of InGaAsP was significantly higher with 22 nm per minute and an etch rate of 30 nm per minute in InP. A picture of the optimized InGaAsP etch can be seen on the right hand side in figure 3.12. The membrane etched in the picture is 220 nm and slightly thinner then the 340 nm thick membrane used for the optical measurements.

Due to the RIE lag effect etch rates reported on bulk structures are significantly higher then the ones measured for the PhC samples described here. Etch rates of 70 $\frac{nm}{min}$ for InP, 50 $\frac{nm}{min}$ for InGaAsP and 30 $\frac{nm}{min}$) for GaAs have been measured by Henry et al. [63] using a similar RIE and similar parameters.

Etch rates of PhC in InP reported by other groups are closer to the ones measured here. Berrier *et al.* reported etch rates of around 10 nm per minute using a $CH_4/H_2/Ar$ plasma [68]. A hole with a diameter of 300nm was used to determine the etch rate.

It should be noted though that it is in general difficult to compare etch rates between different machines, due to the technical differences (volume of the chamber, geometry of the chamber, etc.). There are no
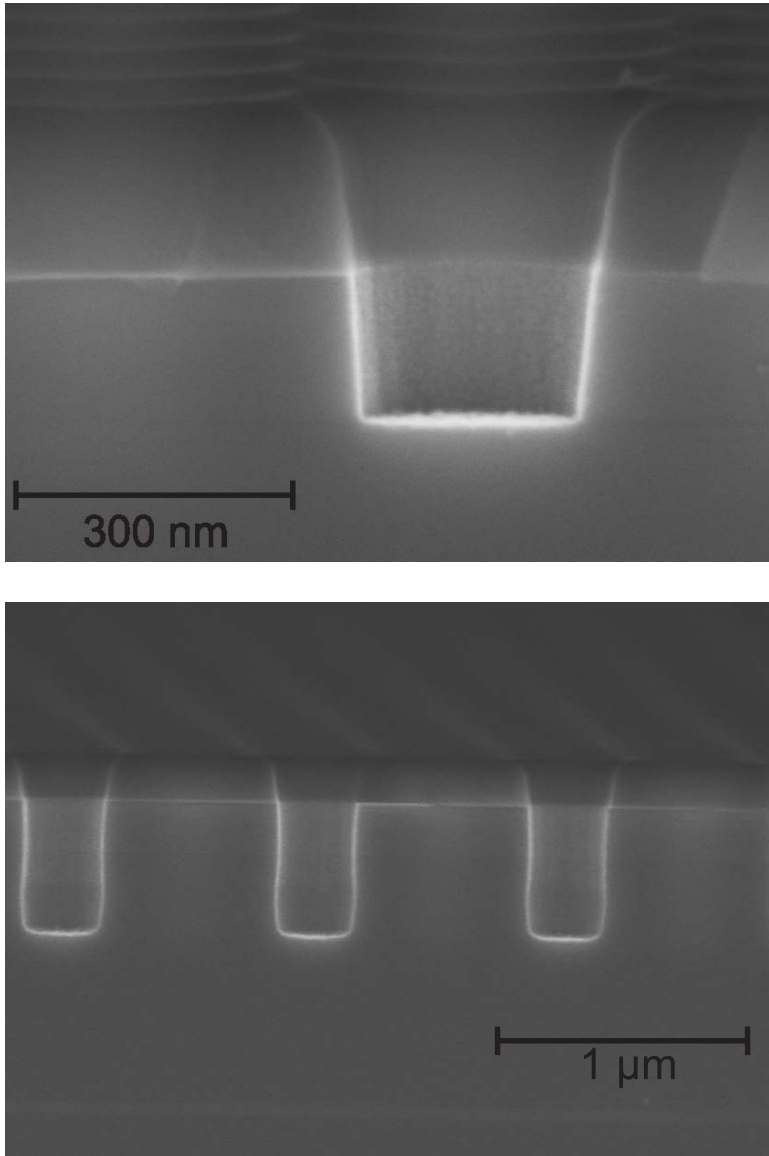
Figure 3.12: Top: Optimized etch MORIE on GaAs membrane structure - Bottom: Optimized MORIE on a InGaAsP membrane structure
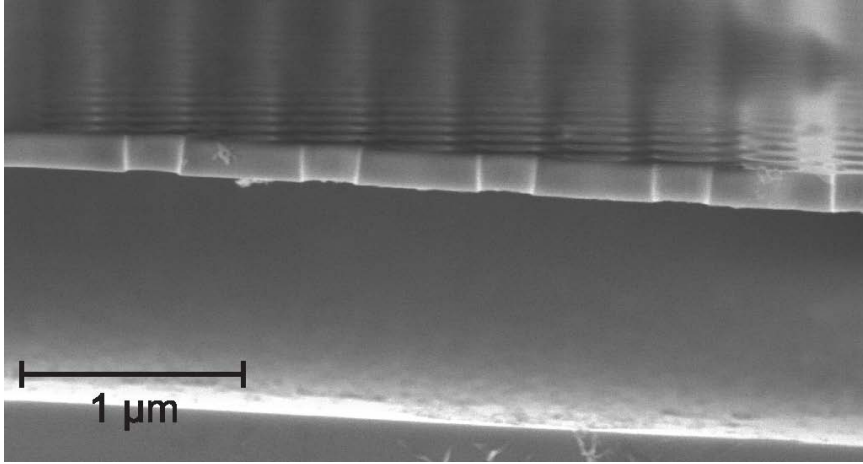
Figure 3.13: Cleaved side view of a fully released GaAs PhC membrane. Pattern was etched using the optimized MORIE recipe.

reports of MORIE of PhC in GaAs that the results presented here could be compared with.

3.6 Membranization of III-V photonic crystals

3.6.1 GaAs membranes using AlGaAs as sacrificial layer

Fabricating GaAs membranes is a straightforward process. $Al_xGa_{1-x}As$ etches rapidly in HF for Al fractions $x > 0.5$ while GaAs virtually does not etch in HF [74].

$Al_{0.65}GaAs$ was used as sacrifical layer and etched in 40% HF. Due to the high etch rate an etch time of ten seconds was sufficient to fully membranize the PhC. A fully released PhC membrane can be seen in figure 3.13

The debris on the bottom are probably remains of the wet etch. Khankhoje et al. have reported that they could remove this debris by a short (150s) wet etch using potassium hydroxide (KOH) [75].

In order to ensure the membranes are fully released the samples can be inspected in an optical microscope. Released membranes show circular discolorations due to the thin membranes slightly bending after release.

For the membranes that were etched using a 200nm layer of Si_3N_4 as hard mask it was necessary to remove the remains of the mask before doing the wet etch in HF. The membranes tend to disintegrate when the AlGaAs is removed at the same time as the Si_3N_4. This problem does not occur when using a thinner mask of 100nm.

Si_3N_4 is know to have a lot of internal stress which is a likely cause for this behavior. In order to only remove the mask and not etch the AlGaAs or GaAs the remains of the mask are removed using the PLASSYS. The recipe for removal of the mask is similar to the one used for etching the Si_3N_4 maks but the pressure is increased to 60 mTorr and the power reduced to 20W in order to avoid surface damage on the GaAs from ions.

3.6.2 InGaAsP membranes using InP/InAlAs as sacrificial layer

The layer structure of the wafer InGaAsP membrane wafer D211 used can be found in Table 3.1. PhC using InGaAsP membranes are commonly used for the fabrication of active PhC slabs emitting at the telecommunication wavelength region [1, 40, 76]. Using InP as a sacrificial layer is common due to the high selectivity between InP and InGaAsP using wet etching chemistry based on HCl.

HCl wet etch of InP is highly anisotropic [77]. Due to that it is necessary to be careful when under-etching PhC membranes that the membrane is fully released. Figure 3.14 shows the a failed attempt to fully release the membrane. Underneath the PhC holes small v-shaped openings along the $\bar{1}00$ can be seen revealing the crystal faces on which the etch stopped. In order for the etch to progress and fully release the
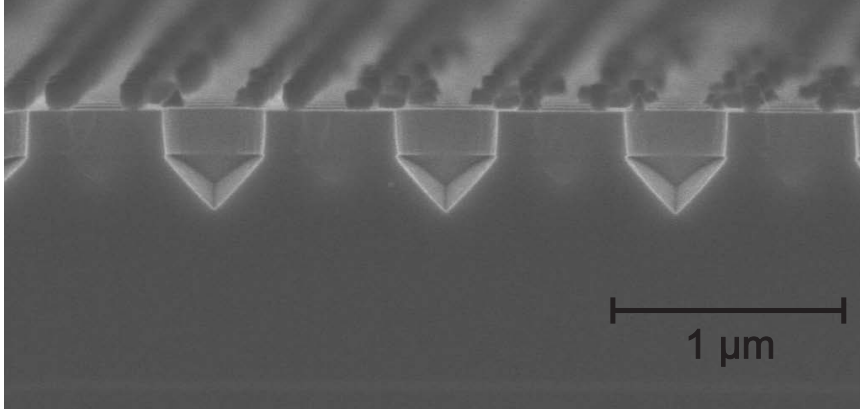
Figure 3.14: InGaAsP membrane structure with a pure InP sacrificial layer etched in one to one ratio HCl:H_2O. Membrane was not fully released due to the anisotropy of the etch. Small openings opened underneath the holes with the etch stopped along specific crystallographic planes.

membranes the openings underneath the holes need to connect [78]. This problem is especially severe for quadratic PhC [79].

Due to the high anisotropy this will require a very long etch time in which also the InGaAsP of the membrane will be attacked by the wet chemistry.

An easy way to avoid this is to etch deep enough into the sacrificial layer so that the etch in lateral direction at the top of the opening connects the holes and allows the membrane to be fully released. Unfortunately it was not possible to etch deep enough since the etch rate in the RIE was not high enough to do so.

So in order to guarantee that the membrane is fully released an additional layer of InAlAs was introduced. InAlAs etches more isotropic in HCl then InP [80] allowing a window to open above the second InP layer and below the first in order to fully release the membrane.
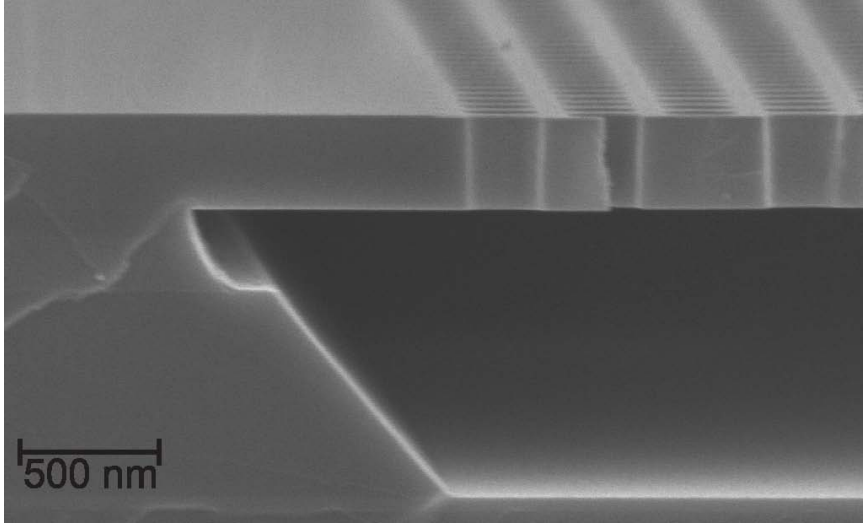
Figure 3.15: Cleaved side view of a fully released InGaAsP PhC membrane. Pattern was etched using the optimized MORIE recipe.

InAlAs in a MOVPE is usually grown at a higher temperature then InP. In order to avoid stopping the whole growth and changing the temperature before starting to grow the layers that will later become the PhC membrane a short intermediate InP is introduced between the InAlAs layer and the first InGaAsP layer. This is strictly speaking not necessary but easier to grow.

Theoretically a good idea, first etch test using only HCl proved unsuccessful as can be sen in figure 3.16. The etch stopped at the interface between the InAlAs and the second InP layer. Likely cause is a byproduct created in the wet etch of the InAlAs layer. In order to remove this byproduct a short intermediate etch with HF was introduced. The reason for the necessity of this etch step is not completely clear but the effect can be seen when comparing the membranes in figure 3.16 with the released membrane in figure 3.15.

The membrane in figure 3.15 is released by etching it two times for
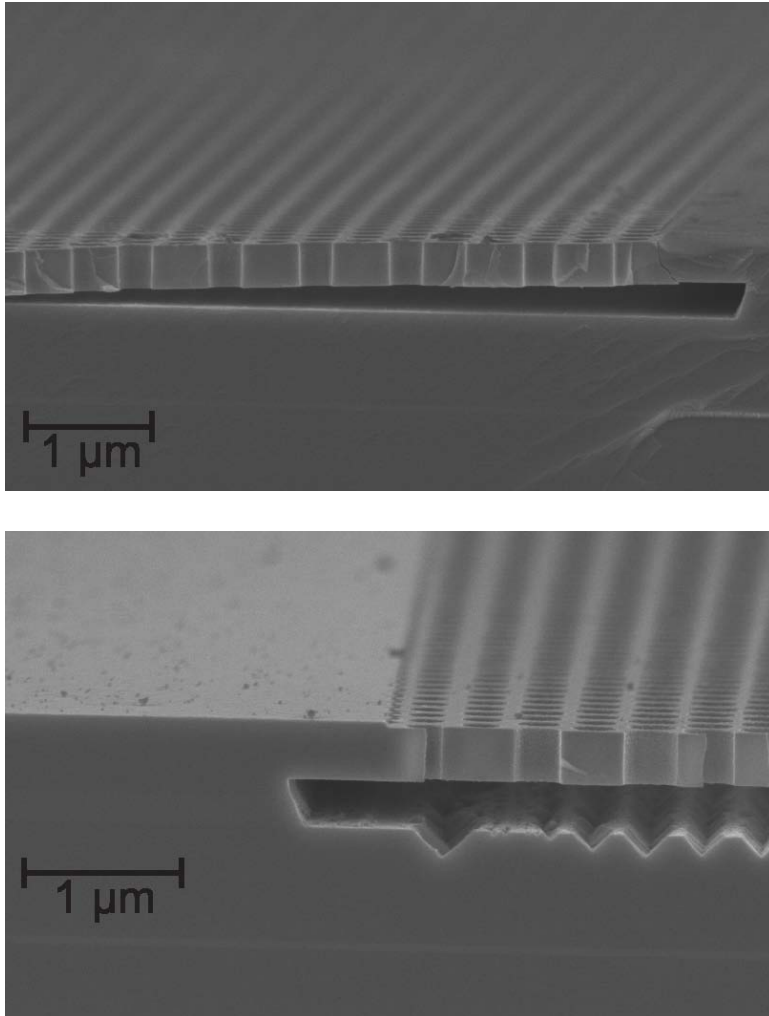
Figure 3.16: Top: 5 min HCl:H$_2$0 1:1 for 5 minutes - Bottom: 10 min HCl:H$_2$0 1:1 for 5 minutes

5 minutes in a one to one ratio mixture of HCl and water with a short two minute intermediate etch in 40 % HF. The sample was rinsed for 30 seconds in DI water after each etch step and carefully blow dried with N2 afterwards.

The same result cannot be reproduced by simply etching the sample for five minutes in HCl, blow drying it with N2 and etching it another five minutes. Due to the susceptibility of the unknown byproduct with HF it is likely that it contains AlOx. A more detailed study, which would be necessary to identify the compound and reaction responsible for the effect, is outside the scope of this thesis.

As already mentioned the released membrane can be seen in figure 3.15. It should be noted though that the etch times for releasing the membrane are rather high. According to literature the etch rate of bulk InP in HCl mixed in a one to one ratio with H_20 is roughly 2.3 μm per minute [77]. The second etch step should therefor take less then one minute.

The etch times measured on the InP underneath PhC membranes is only a fraction of that ($\sim$200 - 300nm per minute) and the etch rate is not very reproducible. A possible reason for this might be that the diffusion of etchants is limited by the PhC membrane. In order to reach the surface etchants have to diffuse through the small holes of the PhC membrane. Introducing trenches next to the PhC is a possible solution to this problem although it might not always be possible to include them [79].

The etch rate of InAlAs was similarly estimated to be around 50 nm per min. Due to the long etch time necessary to release the membrane the InGaAsP is slightly attacked by the etch. The etch rate of InGaAsP ($\lambda = 1.15$) is measured to be $\sim$0.66 nm per minute.

To make sure that the samples were fully membranized samples were inspected from the top in the SEM and etched again for several minutes if the surface underneath the membranes didn't appear to be smoothly
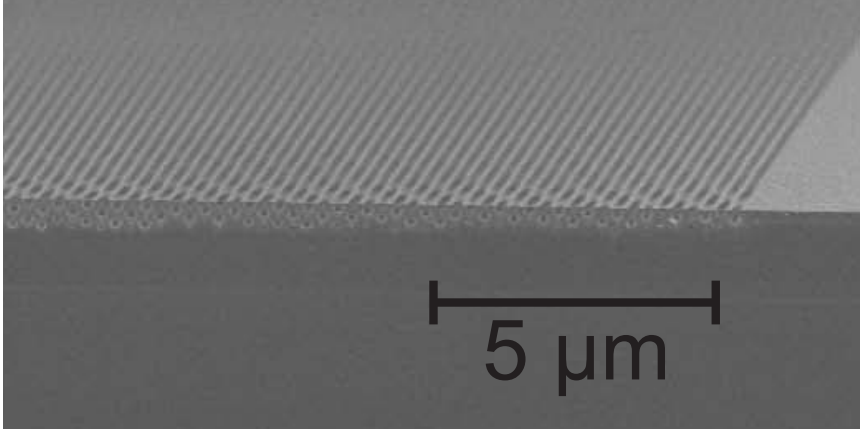
Figure 3.17: Not fully released InGaAsP membrane with 1 micron thick InP sacrificial layer etched for 2:30 minutes in a 1:4 ratio HCl:H3PO4 acid mixture

etched. They couldn't be inspected in the optical microscope like the 160 nm thick GaAs membrane because they are thicker (340 nm) and didn't show the same kind of bending under optical inspection.

Instead of using an InAlAs layer it is also possible to change the etch chemistry to obtain a more isotropic etch of InP. Mixtures of HCl and sulphuric acid (H3PO4) have been reported to etch InP more isotropic [77]. The results were not convincing as can be seen in figure 3.17.

Although the problems of not being able to deeply etch the PhC membrane are overcome by the introduction of a more complex structure of the sacrificial layer, it is generally advisable to etch deep enough when possible in order to avoid the problems outlined above [78].

Chapter 4

Measurements on non-lasing coupled photonic crystal cavities

"Physicist are people that need problems which are simple enough to be put into an equation" - Professor at DTU Fotonik

The measurements presented in this chapter will focus on PhC cavity structures with a square lattice fabricated in GaAs membranes using QD's as a gain medium. The cavities are formed by removing a single hole from the quadratic lattice, so called H1 cavities. The mode mainly investigated is the quadrupole mode in the quadratic lattice which is discussed in section 2.1.4. Unfortunately it was not possible to achieve lasing in these structures. The same type of structures fabricated in InGaAsP membranes using QWs as gain medium showed lasing. The fabrication process of these PhC membranes is explained in great detail in chapter 3 and the mode patterns are shown in chapter 2.

Although these structures could not be brought above threshold, studying them still yields useful information about the coupling of the

quadrupole modes. The setup used to measure the coupled cavity systems is described in section 4.1. In section 4.2 the coupling of two cavities along the Γ-X and the Γ-M directions for different number of holes between the cavities (intracavity hole distance) is investigated. Especially the difference in coupling strength between the two directions is shown and the effect of disorder on the structures is evaluated. The data is then compared to disorder-free FDTD simulations .

After investigating two coupled cavities, measurements on large coupled arrays are shown in section 4.3. Again the effect of different intracavity hole distances is investigated as well as the influence of using different total number of coupled cavities. The results of the measurement are in agreement with standard coupled-mode theory. QDs are especially useful in this context since they act as isolated emitters at a large number of different wavelength. The various modes in the structure are therefore excited independently from each other.

As outlined in section 2.3.1 lasing is achieved when the net losses are overcome by the net gain in a given structure. Losses and gain are specific to the optical modes in a structure and can differ greatly. In PhCs the losses of the optical mode are usually evaluated by measuring the Q of the mode as introduced in section 2.3.1.

There are several possible reasons why the GaAs membranes did not exhibit lasing. The quality of the PhCs in general, etched using the Plassys in GaAs, are not as good as in InGaAsP. Especially the verticality is much better in InP/InGaAsP as can be seen by comparing figure 3.15 with figure 3.13 in section 3.6.2 and 3.6.1, respectively.

Better verticality of the side walls should lead to a better Q [66] and thus lower the threshold gain needed to achieve lasing. A direct comparison between the InP and the GaAs cavities is difficult, though, because the "cold" Q factor for the InP cavities exhibiting lasing cannot be easily evaluated. This is discussed in detail in section 5.2. Although that being the case, the overall Q factors did not seem to differ greatly with

estimated Q's of around 1000 for the quadrupole mode in the quadratic lattice in both cases.

Assuming therefore that the Qs are comparable, the reason for the GaAs structure not achieving lasing must lie in the difference between the gain materials. Two different wafers with InAs QDs in a GaAs membrane were used to measure on (TUM01D & NBI187). The relevant wafer in this context is TUM01D since it contained three layers of high-density InAs QDs. It should be compared against D211 containing ten InGaAsP ($\lambda = 1.52$) QWs in an InGaAsP ($\lambda = 1.15$) membrane. The layer structure for the wafers D211, TUM01D and NBI187 can be found in section 3.3.

QWs exhibit a higher overall gain of around an order of magnitude compared to QDs in bulk structures [46]. While this is true, PhCs are very different from bulk structures. Usually the holes in PhCs are etched all the way through the membrane including the active layer.

The exposed surfaces at the edges of the hole will therefore increase the amount of non-radiative recombination especially in QWs where the carriers can freely diffuse along the membrane. In QDs on the other hand individual QDs close to the surface will loose carrier confinement without affecting the whole ensemble of dots. But QDs are also affected by the etched-through holes in more subtle ways.

The wetting layer that remains in the SK QD growth can be looked upon as a thin QW and plays a large role in the carrier capture process. Carriers are usually not directly captured to the dot but will first be captured to the wetting layer and then decay into an excited dot state. In InAs dots in GaAs this capture time has been measured to be around 5 ps [81]. Capture and further decay to the ground state is mostly mediated by phonons.

The radiative recombination time due to spontaneous emission is usually much longer than the capture time and is on the order of 1 ns. The Radiative decay can be strongly modified in a PhC due to a change

in the DOS as discussed in section 2.3 or by stimulated emission. Purcell enhancement is beneficial and will lower the threshold since it increases the radiative recombination rate.

Losses due to non-radiative recombination at the surfaces of the PhC holes below threshold are therefore more likely an issue in QW structures than in QD structures and do not explain the absence of lasing in the QD structures.

The explanation is most likely connected to the small size of the PhC cavities since it limits the amount of active material inside the cavity. This can especially be a problem with QDs at low temperatures. Individual QDs usually show narrow emission lines depending on temperature. In order for a dot to contribute to the gain of a given mode, the dot must not only overlap spatially with the mode but also the emission line must spectrally overlap. In PhC cavities usually only a fraction of the dots are actually contributing to a given high-Q mode.

For example, a simple way to evaluate the number of dots that participate in the gain of a given cavity mode to look at the spectral overlap between the cavity mode and the inhomogeneously broadened ensemble of QDs. The inhomogeneously broadened ensemble of QDs of TUM01D can be fitted with a Gaussian function with a full width half maximum (FWHM) of around 50 nm. The Q of the quadrupole mode below threshold is around 1000 which is equal to a linewidth of 0.95 nm at a resonance wavelength of 950 nm. Assuming that the linewidth of each individual QD is much narrower than the cavity linewidth at 4K, the percentage of dots contributing to the cavity mode can be approximated by:

$$\frac{\delta_{cavity}}{\delta_{dotensemble}} = \frac{0.95}{50} \approx 0.02 \qquad (4.1)$$

Only around 1% of the dots actually directly overlap with the cavity mode. This is only a rough approximation since the spatial overlap between the cavity mode and the dots is not taken into account. This is especially important if the dot density is low. Higher order states of the

QDs are also not taken into account although they might contribute to the cavity mode at higher pump powers.

Also QDs in PhC structures have been shown to couple to cavities although they are spectrally detuned from the cavity resonance [19]. Possible explanations for this behavior have been attributed to pure dephasing [82] or coupling mediated by multi-excitons [83].

Apart from the fact that only a fraction of dots can participate in the gain of the relevant mode, the InGaAsP structure has a much higher number of active layers (10 QWs in D211 compared to 3 layers of QDs in TUM01D). This was possible since the straincompensated InGaAsP QW structures can be stacked closer and they emit at longer wavelengths, which makes it possible to increase the thickness of the membrane and include more layers of gain material.

This indicates that the available gain provided by the QWs in the InGaAsP structures is much higher than that in similar structures provided by the InAs QDs in GaAs. Furthermore the non-radiative recombinations at surfaces is usually lower in the InP system than in the GaAs system.

Lasing in PhC cavities using InAs QDs has been reported also in the case of very few QDs used as gain material [19]. Strauf et al. estimated the Q factor of their cavities to be well above 5000 even with the most conservative guess, showing that lasing is generally possible but the requirements on the quality of the PhC cavity is rather high.

The quadrupole mode in the H1 cavity in the quadratic system has in general a rather low Q. Measurements by Altug et al. [2] using similar structures in InGaAsP have on the same mode reported Q factors of 1200 for uncoupled and 900 for coupled structures. In section 2.3.2 a simple approximation for the necessary threshold gain is made. A three-layer QD structure would need a Q of around 6500 in order to show lasing. It might therefore be difficult in general to achieve lasing for this particular type of mode.
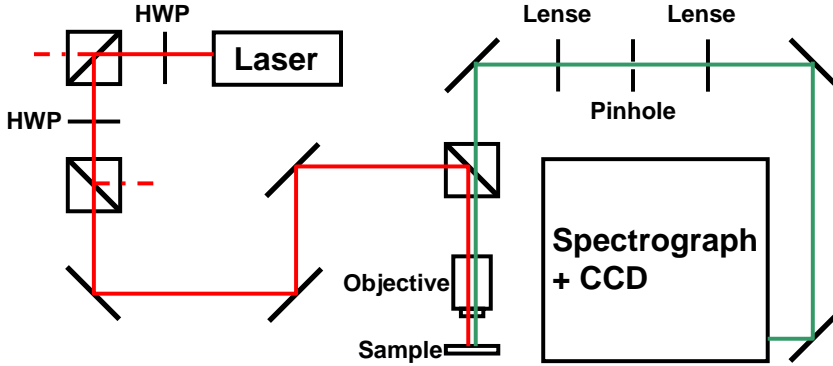
Figure 4.1: Confocal microscopy setup to characterize PhC structures

4.1   Experimental setup for characterization of structures at short wavelength in the near infrared ($\sim 1\mu$m)

Figure 4.1 shows a schematic drawing of the setup used to characterize the PhC described in this chapter. It is a standard confocal photoluminescence (PL) microscopy setup. The laser used for excitation was a Coherent MIRA 900 system in picosecond mode (pulse width ∼2ps). The pulse power used to excite the structures was high enough to saturate the QDs fully.

In order to move the sample, the entire cryostat with the samples mounted inside was moved parallel to the plane of the optical table. The objective to excite the structures and collect the emitted light was mounted perpendicular to the optical table. The stages were moved by a stepper motor and had a minimal reproducible step size of 200 nm.

The objective used to collect and excite structures was a high NA objective (NA=0.60) with a 40x magnification from Nikon. The nominal transmission of the objective was measured to be around 77% at 800 nm

and the spot size was around 2.4 μm (FWHM) [84]. The flow cryostat used for the measurements was an Oxford Hi-res-MKII system modified with an enlarged view port. The cryostat was cooled using mostly liquid nitrogen or helium if available.

A 670 mm grating spectrograph in Czerny-Turner configuration was used to spectrally resolve the collected light. All the measurements were carried out using a 600 lines/mm grating with a resolution of 0.08 nm. The light was detected by a silicon CCD connected to a PC. The quantum efficiency of the CCD is at around 34% a wavelength of 900nm and drops to around 14% at a wavelength of 1000nm.

4.2 Measurements of the quadrupole mode in two coupled cavities

In this section measurements of two coupled H1 cavities in the quadratic lattice are presented. The various modes found for this particular defect are described in section 2.1.4. Measurements presented will focus on the quadrupole mode. Also dipole modes were measured but characterizing them was difficult.

Due to fabrication tolerances the degeneracy of the dipole mode is lifted. A single cavity will therefore show two peaks at different resonant frequencies one for the x-polarized and one for the y-polarized dipole. Two coupled cavities will show then four peaks in close spectral proximity to each other. This combined with the low Q ($\sim$300) that was measured, makes it difficult to clearly distinguish all the peaks from each other. Nevertheless, it is helpful to measure the dipole modes in order to clearly identify the quadrupole modes.

Figure 4.2 shows the SEM images of two coupled PhC cavities in the quadratic lattice for intracavity distances of two, three and five holes. Figure 4.2a shows cavities coupled in Γ-X direction and figure 4.2b shows cavities coupled in Γ-M direction.
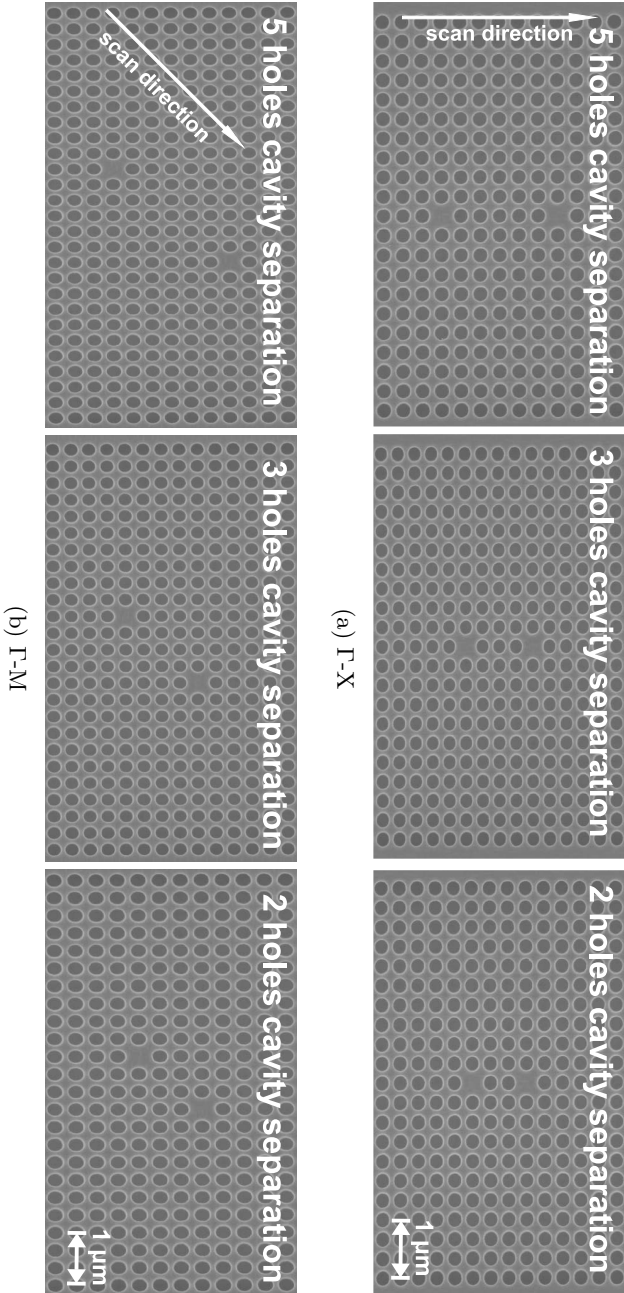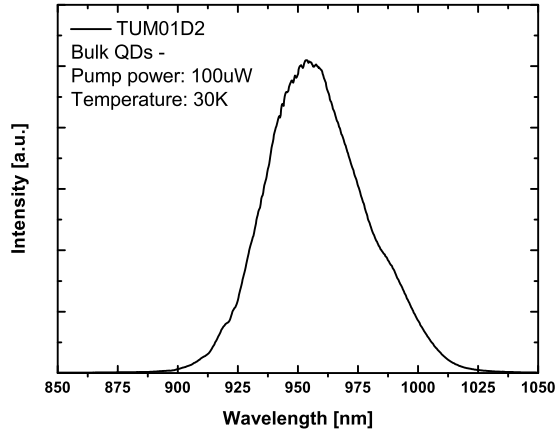
Figure 4.2: SEM of the coupled cavities structures for 5,3 and 2 holes intracavity distance in Γ-X and Γ-M direction

The cavities were characterized by PL spectroscopy using the setup described in section 4.1. The structures were realized in GaAs membranes using InAs QDs as optical gain medium. The PhC cavities have hole diameters of around 217 nm and a lattice pitch of 280 nm. The fabrication procedure is outlined in chapter 3. Bulk emission of the QDs measured at a temperature of around 10 K without any patterns can be seen in figure 4.3b (Wafer:NBI187).

Measurements on the coupled cavities were carried out at higher temperatures around 60 K. Points of main interest are the resonance frequencies of the coupled cavities. The slightly elevated temperature will shift the emission of the dot ensemble towards longer wavelengths. The PL peak energy though will only slightly change between 10 and 60 K [85].

The influence of the change of temperature on the resonance frequency of the cavities is smaller than the influence on the emission frequency of the dots. PhC cavities in GaAs membranes are fairly insensitive to temperature apart from a small shift in the resonance frequency due to the temperature dependence of the refractive index. At low temperatures the cavities will shift around 0.1 $\frac{nm}{K}$ [86]. The reason for measuring at slightly higher temperatures instead of at 10 K is that it is possible to use liquid nitrogen for cooling instead of liquid helium. Nitrogen is more readily available as well as cheaper than helium.

Coupled cavities in PhC have been extensively studied in the context of WGs, so called coupled optical resonator WGs (CROWs). CROWs have been first proposed by Yariv *et al.* [30]. The proposal is not specific to PhC cavities but general to all high Q resonator. In a CROW light is transmitted by exchange of photons between the resonators whose modes overlap. The higher the Q of the resonator the narrower the transmission band becomes. Due to the small group velocity which can be realized in CROWs they can be used to slow light down and act as delay lines [87]. The original coupled cavity structure by Altug *et al.* was proposed as a 2D equivalent of a CROW structure [3].

(a) TUM01D2
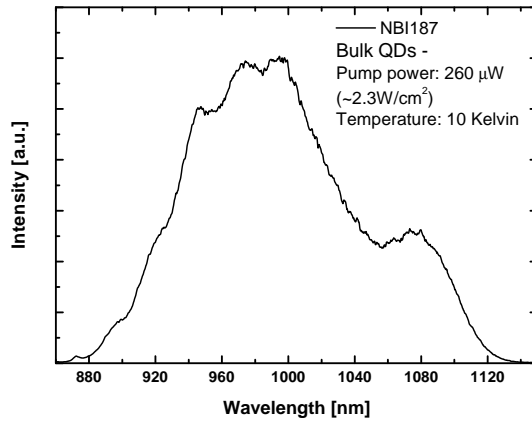
(b) NBI187

Figure 4.3: PL-spectra from the QDs in the wafers used for carrying out experiments to characterize the mode structures of the coupled cavity systems

Coupled cavities or also photonic molecules have been realized by several groups but mostly in the triangular lattice [32, 88, 89]. As was mentioned before the structures shown here are similar to the structures proposed and realized by Altug *et al.* [1]. Although lasing properties were extensively described, no detailed data were published on the mode structure of the coupled cavity arrays below threshold.

4.2.1   PL-measurements of coupled cavities below threshold

Figure 4.4 and figure 4.5 show the results of scanning the PhC coupled-cavity structures. The maps show several spectra taken in sequence along the coupling direction of the PhC structure. On the x axis the wavelength is plotted and the greyscale shows the intensity. Along the y axis the position of the stage during the scan is shown. The stage was moved in steps of around 200nm which was the smallest reproducible step size that the stages could be moved. The y-axis is shifted so that the cavity peaks are centered around position zero.

All of the cavity maps show two peaks which can be clearly identified. It is apparent that the spectral separation of the peaks are strongly dependant on the number of intracavity holes separating the cavities. This indicates that at least some of the peaks originate from two coupled modes instead of two separate modes. Structures coupled in the Γ-X direction show a spectral splitting of 7.4 nm, 3.4 nm and 1.4 nm for a separation of 2, 3 and 5 holes respectively. For the Γ-M direction the splitting is 3.3 nm , 0.5 nm and 0.5 nm again for a separation of 2, 3 and 5 holes, respectively.

In order to better analyze the peaks and compare them with each other they were fitted using Lorentzian functions. Depending on how well they were spectrally separated they were either fitted individually or fitted with a double Lorentzian. In both cases only a small fraction of the spectrum around the peaks was fitted. A parabolic function was used to fit and remove the background. The peak height of both modes without
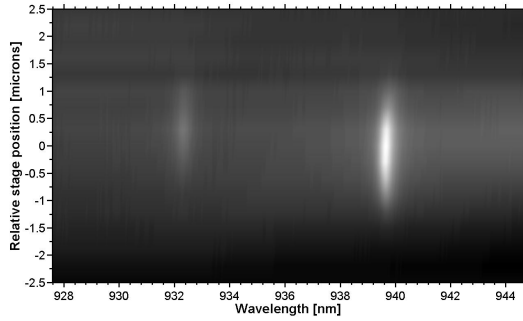
(a) 2 holes intracavity distance
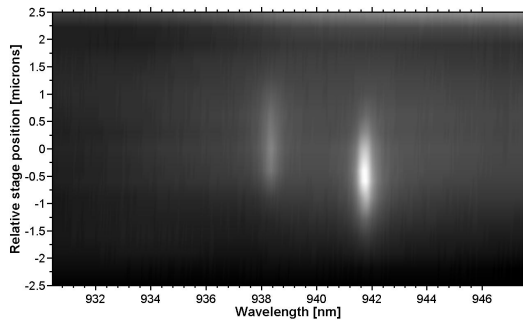
(b) 3 holes intracavity distance
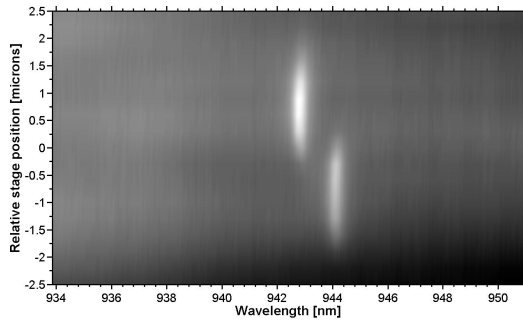
(c) 5 holes intracavity distance

Figure 4.4: Spectral intensity maps of two coupled PhC cavities Γ-X direction for intracavity distance 2, 3 and 5 holes. Each horizontal line represents a spectrum taken at a different position. The cavities were scanned along their coupling direction.
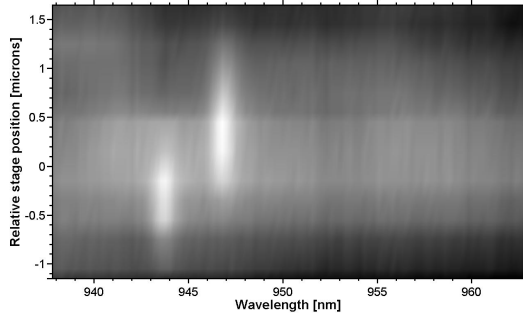
(a) 2 holes intracavity distance
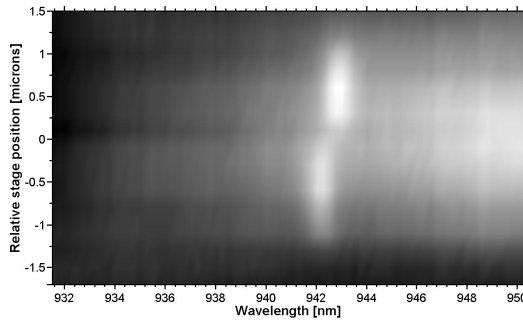
(b) 3 holes intracavity distance
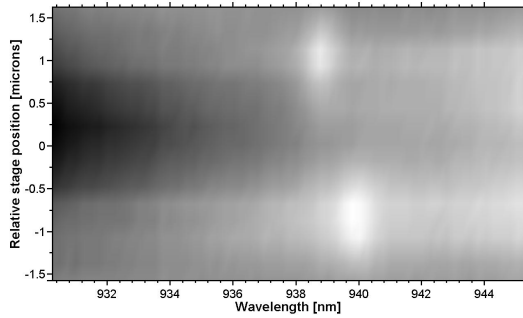
(c) 5 holes intracavity distance

Figure 4.5: Spectral intensity maps of two coupled PhC cavities Γ-M direction for intracavity distance 2, 3 and 5 holes. Each horizontal line represents a spectrum taken at a different position. The cavities were scanned along their coupling direction.

the background is plotted against the spatial position of the stage in figure 4.6 and figure 4.7 for the Γ-X and Γ-M structures, respectively.

The plots show that the peaks are spatially separated from each other which could indicate that the modes are actually uncoupled. Table 4.1 compares the distance between the maximum of the fitted modes with the actual distance taken from the structure. For short coupling distances in the Γ-X direction, as in the case for the 2 and 3 hole separation, the distance between the cavities according to the structure differs from the distance measured between the maxima of the fitted peaks. For 5 holes of intracavity separation the distances match.

The actual distance between the cavities is the geometric distance between the center of the cavities taken from the design of the structure while the distance between the fitted peaks is the difference between the two stage positions under which the maximum amount of light is collected for either mode. The light is collected in the far-field so the actual center of the cavity might not be the position under which most light is collected since the far-field emission from the PhC cavity is not necessarily peaked in the center.

But the structure is symmetric so that the collection efficiency for either cavity should be the same. Measuring a decoupled mode in either cavity should therefore result in seeing the same curve for either mode shifted relative to each other with the actual distance between the cavities. If the maxima of modes are closer to each other than the actual distance between the cavities than it can be assumed that light is emitted from both cavities and the modes are coupled modes.

This means that for 2 and 3 hole separations in the Γ-X direction, the cavities are coupled while at 5 hole separation the cavities are most likely uncoupled and act as individual cavities. The spectral difference of 1.4 nm between resonance frequencies for the cavities separated by 5 holes can be explained by fabrication tolerances. Small changes in the
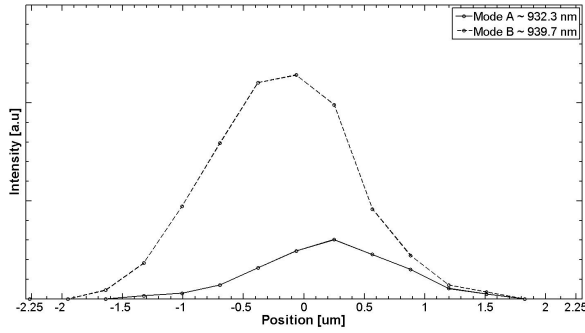
(a) 2 holes intracavity distance
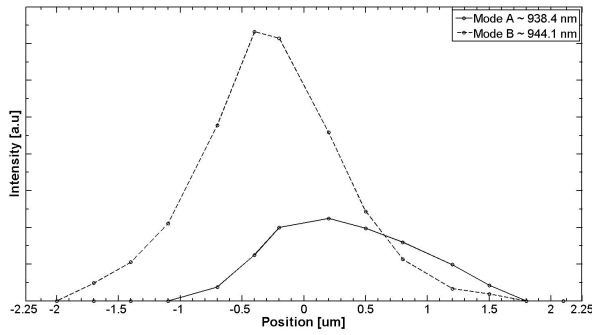
(b) 3 holes intracavity distance
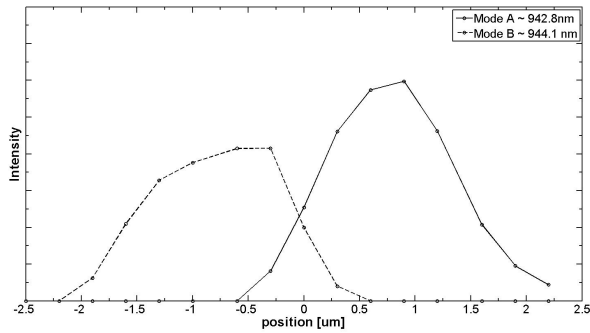
(c) 5 holes intracavity distance

Figure 4.6: Intensity of the fitted peaks for two coupled PhC cavities in Γ-X direction for intracavity distance of 2, 3 and 5 holes at different positions. Each position corresponds to a spectra which is fitted separately. The relative position at which the spectrum was taken is indicated on the x-axis. The cavities were scanned along their coupling direction,
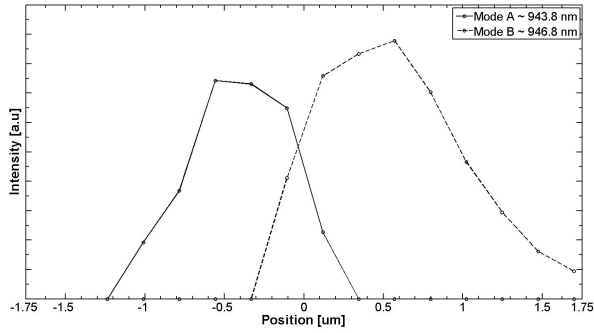
(a) 2 holes intracavity distance
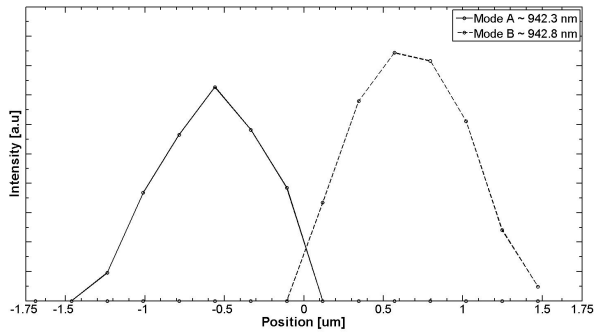
(b) 3 holes intracavity distance
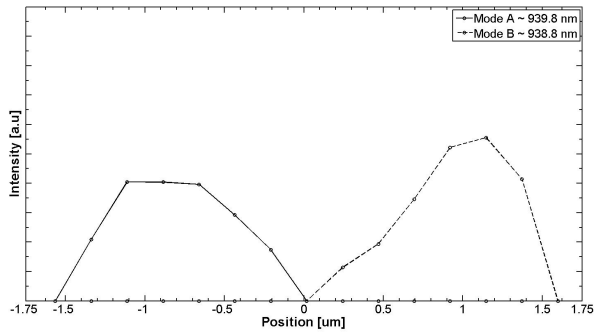
(c) 5 holes intracavity distance

Figure 4.7: Intensity of the fitted peaks for two coupled PhC cavities in
Γ-M direction for intracavity distance of 2, 3 and 5 holes. Each position
corresponds to a spectra which is fitted separately. The relative position
at which the spectrum was taken is indicated on the x-axis. The cavities
were scanned along their coupling direction,

Structure	Distance between cavities (center to center) [μm]	Distance between maxima of the fitted peaks[μm]
2 holes Γ-X	0.84	0.5
3 holes Γ-X	1.12	0.8
5 holes Γ-X	1.4	1.4
2 holes Γ-M	1.18	0.8
3 holes Γ-M	1.58	1.3
5 holes Γ-M	2.38	2.2

Table 4.1: Intracavity distance

size and/or the position of the holes surrounding the cavities can slightly change the resonance frequency.

Similar observations were made by Atlasov *et al.* for measuring on coupled L3 cavities in the triangular lattice [32]. L3 is a defect with three holes missing in a line. They measured for different distances between cavities and observed a reduction in the spectral splitting with increasing number of holes in between. Furthermore, they used SEM images to model the cavities they measured on, thereby taking disorder due to fabrication tolerances into account.

They showed by using a simple linear harmonic oscillator model that due to the disorder the coupled modes will stop being symmetric and be preferentially localized to one of the cavities. At even larger separations the modes stop being coupled and the cavities will act as two single cavities. The more disorder is present in the system the more the resonance frequencies of the individual cavities will differ from each other. In order for the cavities to couple efficiently the coupling coefficient needs to be larger then the difference between the resonance frequencies of the individual cavities.

The same type of behavior can be seen for the Γ-M direction except that the coupling is weaker than in the Γ-X direction as can be seen by

comparing the spectral splitting in figure 4.5 with figure 4.4. Comparing the actual distance with the measured distance between the maxima of the fitted peaks shows no clear distinction as in the case of the Γ-X direction, as can be seen in table 4.1.

The difference between actual distance and distance between the maxima of the fitted peaks is larger for the 2 hole separation then for 3 and 5 hole separations, but there is still a difference even in the 5 hole separation case. This is most likely due to measurement inaccuracies. The sample was aligned so that the Γ-X coupling direction was parallel to the axes of the x-stage. In order to measure in the Γ-X direction only one of the stages had to be moved while for measuring in Γ-M both stages had to be moved. The stages were operated at their minimum step size so that they probably did not move along a straight line in the Γ-M direction but wobbled along an imaginary line between the cavities. The stage position for the Γ-X direction given in figure 4.6 is therefore more accurate than the one given for the Γ-M direction in figure 4.7.

Altug *et al.* [3] have argued by examining the band diagram of the quadrupole mode that coupling in Γ-X and Γ-M directions should be very similar due to the small bending of the band. Due to the flatness they argued that the H1 defect in the quadratic lattice is especially well suited to allow for a uniform coupling of an array of cavities. The measurements here do not fully support this claim. It is clear that coupling in the Γ-X direction is preferred over the Γ-M direction.

A similar spectral splitting for the 2-hole separation in the Γ-M direction is measured as for 3-hole separation in the Γ-X direction. Although the number of holes between the cavities is different, the distance is almost identical, as can be seen from table 4.1. The fact that the amount of spectral splitting is similar for a similar distance between cavities in the Γ-X and Γ-M direction could indicate that the coupling strength is more strongly linked to the distance than the amount of holes between cavities.

This would explain why, even though the band is relatively flat, the coupling is still stronger in one direction. Unfortunately, in the quadratic lattice cavities, which are separated by the same number of holes, will always be closer to each other in terms of distance in Γ-X direction than in Γ-M.

Even though the cavities can couple despite of disorder, when they are close enough to each other they will still show some sort of preferred localization. This should be taken into consideration when building large coupled arrays because even though the cavities might all be coupled with each other the modes will probably not be spread uniformly throughout the structure.

In figure 4.8a and figure 4.8b the measured spectral splitting is compared with the spectral splitting obtained by simulating the same structures using a 3D FDTD solver [27]. The structures simulated are using nominally the same hole sizes, pitches and membrane thickness as the real structures but no actual SEM images of the fabricated structures were used, so the simulations are free of disorder. The modes will therefore couple even for very large separations, although with increasing distance longer calculation times are required to resolve the differences in resonance frequencies between modes.

The same trend as in the measurements can be observed in the simulations. Coupling in the Γ-X direction is stronger than in the Γ-M direction and the closer the cavities are the stronger the coupling becomes, as can be seen in figure 4.8. It should be noted that the spectral splitting in the simulations is smaller than in the experiment. A possible reason for this is that simulated cavities have a much higher Q than the fabricated structures. A higher Q means a better confinement of the mode to the cavity which would decrease the overlap between the individual cavity modes and therefor reduce the amount of coupling between the cavities.
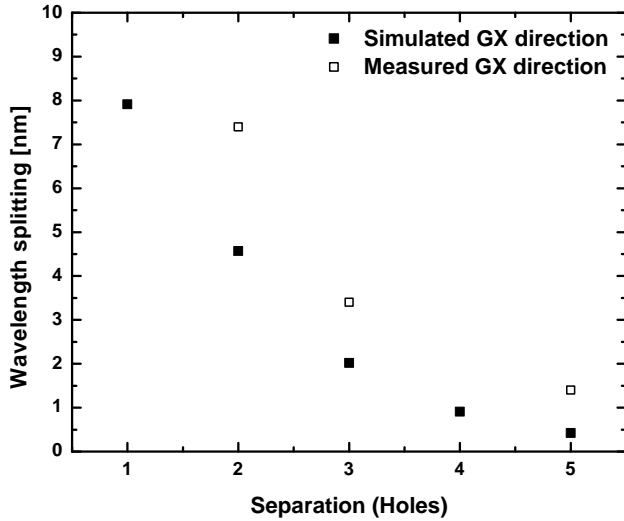
(a) Coupling in Γ-X direction
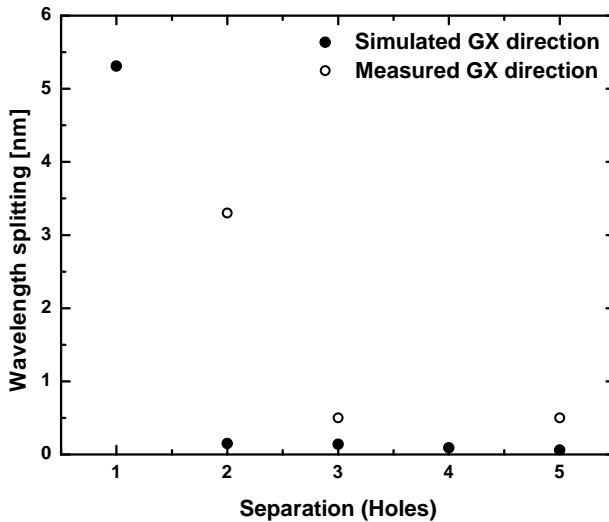
(b) Coupling in Γ-M direction

Figure 4.8: Comparison of the spectral splitting for 2 coupled cavities between measured and simulated structures.

4.3   Arrays of coupled cavities

The advantage of looking at only two coupled cavities is that the structures are small enough so that they can be efficiently simulated. Going to a large number of cavities does not only increase the size of the computational domain but also increases the number of modes that need to be identified. This is discussed in more detail in section 2.2.2.

The fabricated PhCs are again H1 defects in the quadratic lattice as in the previous section. The PhCs have a pitch of 300nm and a measured hole diameter of 273 nm. The diameter was measured by inspecting SEM images of the structures prior to removing them from the cleanroom for characterization. The setup used for optical characterization of the structures is the same as used to characterize the 2 coupled cavities which is described in section 4.1. All measurements were carried out at cryogenic temperatures of around 60 K.

The wafer in which the structures were fabricated is called NBI187. The wafer has one layer of low-density InAs QD's in a 160 nm thick GaAs membrane. The layer structure of the wafer can be found in section 3.3. The emission from the QD's without patterns is shown in figure 4.3b.

The structures are arrays of coupled cavities placed in a square pattern according to the symmetry imposed by the underlying PhC lattice. Both the number of coupled cavities as well as the coupling strength between cavities were varied.

Figure 4.9 shows a SEM image of arrays of coupled cavities with different number of holes between cavities. The cavities were characterized in a similar way as the coupled cavities by scanning across the membrane and recording spectra at different positions. The collection spot is around 2.4 μm and depending on the number of intracavity holes for a given structure, the number of cavities light is collected from will vary due the difference in distance between cavities.

For the smallest structure depicted in figure 4.9a almost all cavities can be measured by placing the collection spot in the center of the struc-
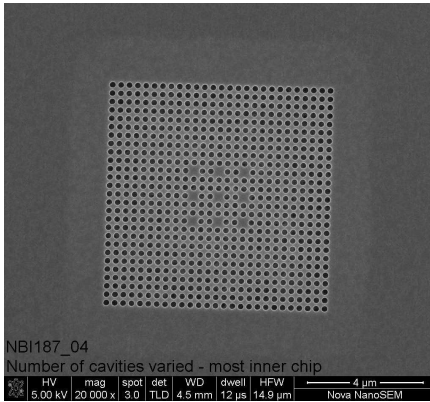
(a) 2 holes intracavity distance
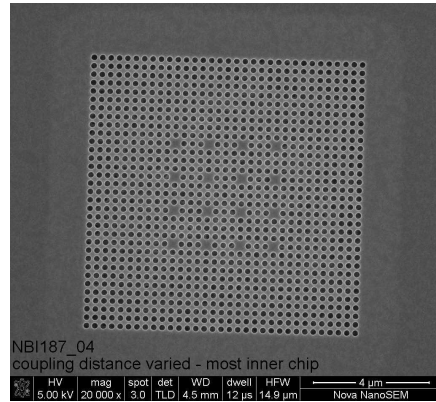
(b) 3 holes intracavity distance
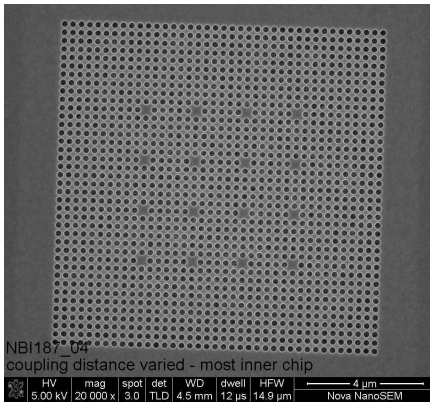
(c) 5 holes intracavity distance
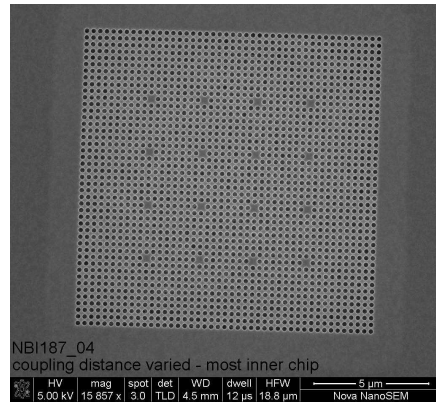
(d) 7 holes intracavity distance

Figure 4.9: CORAL structures fabricated on wafer NB187.

ture. The distance between the lower left and upper right cavity is 2.55 μm and therefore only slightly larger than the collection spot. For the largest structure depicted in figure 4.9d light can only be efficiently collected from a single cavity since the distance between two neighboring cavities in Γ-X direction is 2.4 μm.

In figure 4.10 spectra measured at different positions across the membrane are shown for the structures depicted in figure 4.9. As in the case for two coupled cavities, a spectral splitting can be observed. The modes are split by 21, 12.1, 8.5 and 4.4 nm for intracavity distances of 2, 3, 5 and 7 holes respectively.

Especially interesting is figure 4.10b, while the modes measured from the structure are clearly coupled due to the large spectral splitting, and based on the measurements done for the two coupled cavities, the emission from the array is not uniform. This indicates that as with the two coupled cavities, modes are most likely localized to different parts of the structure. This effect is probably enhanced due to the fact that QDs form an inhomogeneous gain medium and the coupling between the modes and the dots might depend on the resonance frequencies of the QDs in the individual cavities which are excited.

Comparing the splitting measured for the array of coupled cavities with the splitting measured for two coupled cavities shows a larger splitting for the arrays. In the array both coupling in the Γ-X as well as in Γ-M direction take place. Also cavities in the array can couple to all neighboring cavities. This increases the spectral splitting between the different modes.

Also, for the large arrays proximity effects in the e-beam writing might play a role. Holes surrounding the cavities at the edge of structure might therefore receive a significant lower dose than in the center. This would explain why the resonance frequencies for the array with 7 holes between cavities are more spread (4.4 nm) than for the two coupled cavities in the Γ-M direction with 5 holes in between (0.5 nm) although

(a) 2 holes intracavity distance

(b) 3 holes intracavity distance

(c) 5 holes intracavity distance

(d) 7 holes intracavity distance
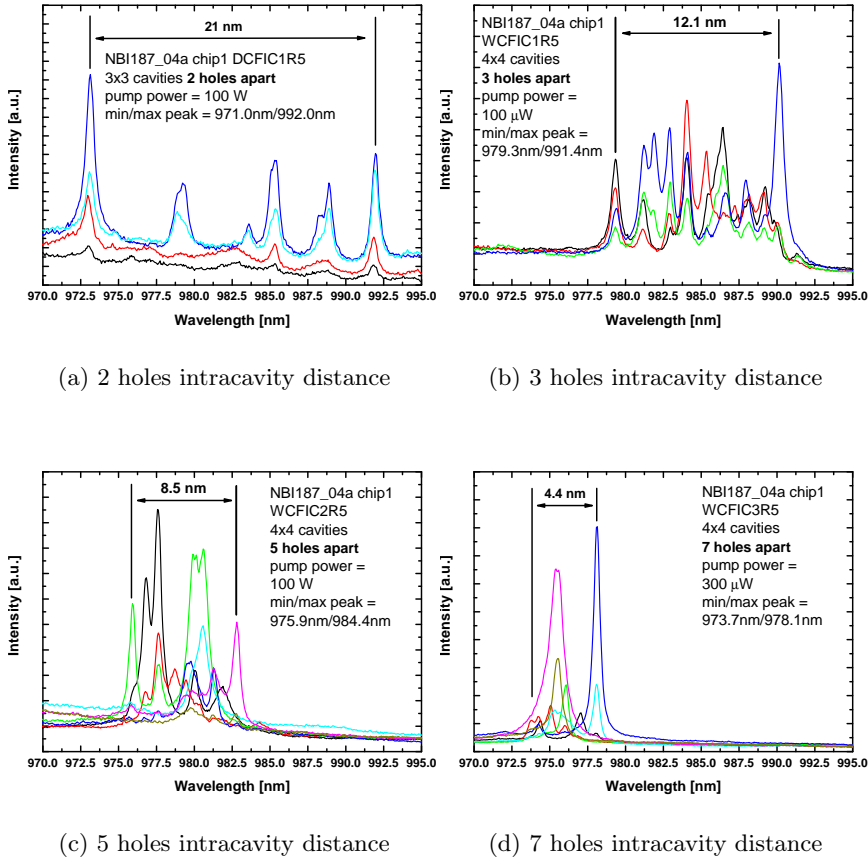
Figure 4.10: PL spectra measured on CORAL structures with different intracavity spacing. Different traces are measured at different positions of the structures. Diameter of the excitation/collection spot was around 2.5 microns. Samples were cryogenically cooled and measured at around 61.5 K.

the cavities should be decoupled in both cases and therefore show the same spread in frequency. There is always going to be some amount of spread present depending on the fabrication imperfections.

The reason why the array is more affected by proximity effects during exposure than the two coupled cavities can be explained by simple geometry. For the two coupled cavities the holes around both cavities will receive the same amount of proximity related additional exposure for symmetry. In the array, on the other hand, the amount of backscattering in the center will differ from the amount of backscattering on the edges. The larger the array and the more the cavities are apart, the more pronounced the effect will be. Since cavities are spread throughout the whole structure, cavities will have a slightly different resonance frequency than cavities on the edge due to changes in the hole sizes. Proximity effects in general are explained in greater detail in appendix B.

The two plots in figure 4.11 should be compared with figure 4.10a. All three plot show a different number of total cavities with two holes intracavity spacing. The spectral splitting is comparable in all three structures with the larger arrays having a slightly larger spread, again probably due to proximity effects. The different traces are different positions on the sample. As before, the emission from the structure is not uniform but depends on the position of excitation/collection spot.

The important difference between the different structures, though, is the total number of modes in each structure. As expected with increasing number of cavities, the number of modes increases and they become more closely spaced. Due to their finite Q they start to overlap and form a band-like structure as can be expected from coupled-mode theory.
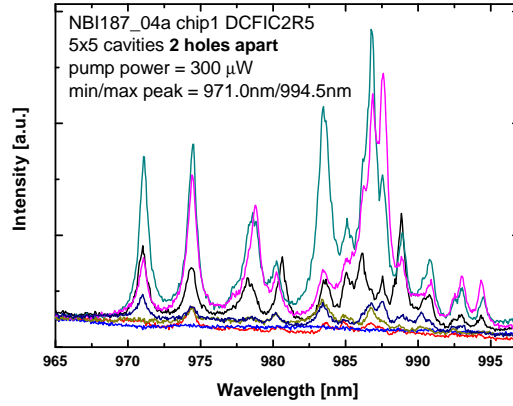
(a) 2 holes intracavity distance 5x5 cavities
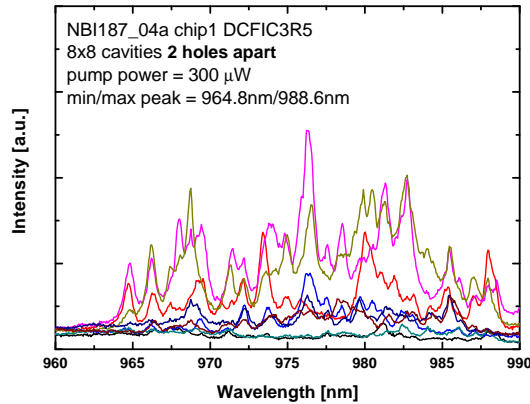
(b) 2 holes intracavity distance 8x8 cavities

Figure 4.11: PL spectra measured on CORAL structures with two holes intracavity spacing. Number of coupled cavities varied. Different traces are measured at different positions of the structures. Diameter of the excitation/collection spot was around 2.5 μm. Samples were cryogenically cooled and measured at around 61.4 K.

Chapter 5

Coupled photonic crystal array lasers

"If you pump it hard enough, you can get glass to lase." - Professor at DTU Fotonik

In the previous chapter 4 GaAs membranes with InAs QDs as active materials are characterized which do not exhibit lasing behavior. In this chapter PhC slabs in that exhibit lasing are presented. The PhC structures are similar as the ones shown previously but differ due to a change in the emission wavelength of the gain medium. They are fabricated in InGaAsP ($\lambda = 1.15$) lattice matched to InP with ten InGaAsP ($\lambda = 1.52$) QWs as gain material. Reasons for the difference in the lasing behavior between the InGaAsP PhC membranes and the GaAs membranes are discussed in the beginning of chapter 4.

Most of these structures presented in this chapter are based on the quadrupole mode in the quadratic lattice which is the same mode that was examined in detail in chapter 4 below thresholds. Section 5.2 will focus on lasing of a single cavity, section 5.3 shows lasing in two coupled cavities and section 5.4 show lasing for arrays of coupled cavities. At the

end of last section a conclusion will be drawn comparing the structures
with each other and with the results obtained by Altug *et. al.*.

All the structures presented in this chapter were fabricated on the
same wafer which is described in section 3.3. The layer defining the
membrane was 340 nm thick. All measurements presented in this chapter
are done at room temperatures.

Due to the difference in the lattice parameters between GaAs and
InP, structures grown lattice matched to InP emit usually at longer
wavelength. The QWs used for the structures in this chapter emit at
a wavelength of $\sim$1.52 μm. Because of this a new setup was required to
characterize the samples and had to be built from scratch. A descrip-
tion of the setup can be found in the following section 5.1. Changing
the wavelength to 1.5 μm is in any case a good choice since the main
interest for these structures lies in applications for telecommunication.

Apart from single hole defects in the quadratic lattice also another
single defect structure is investigated. In section 5.2.1 lasing from a
different type of PhC laser is presented called lambda-shifted PhC laser.

5.1   Experimental setup for characterization of structures at telecommunication wavelengths (1μm-1.6μm)

The setup depicted in figure 5.1 is a confocal PL microscopy setup similar
to the one shown in figure 4.1 in section 4.1. The green line shows the
beam path for the light used to excite the sample. The blue line shows
the path of the white light used to image the surface of the sample on
to a standard silicon CCD camera in order to inspect the structures
and position the sample for excitation. The path of the emitted light
is shown by the red line. The blue line is only drawn where it diverges
from the path of the pump light and the emitted light, not to overcrowd
the picture.
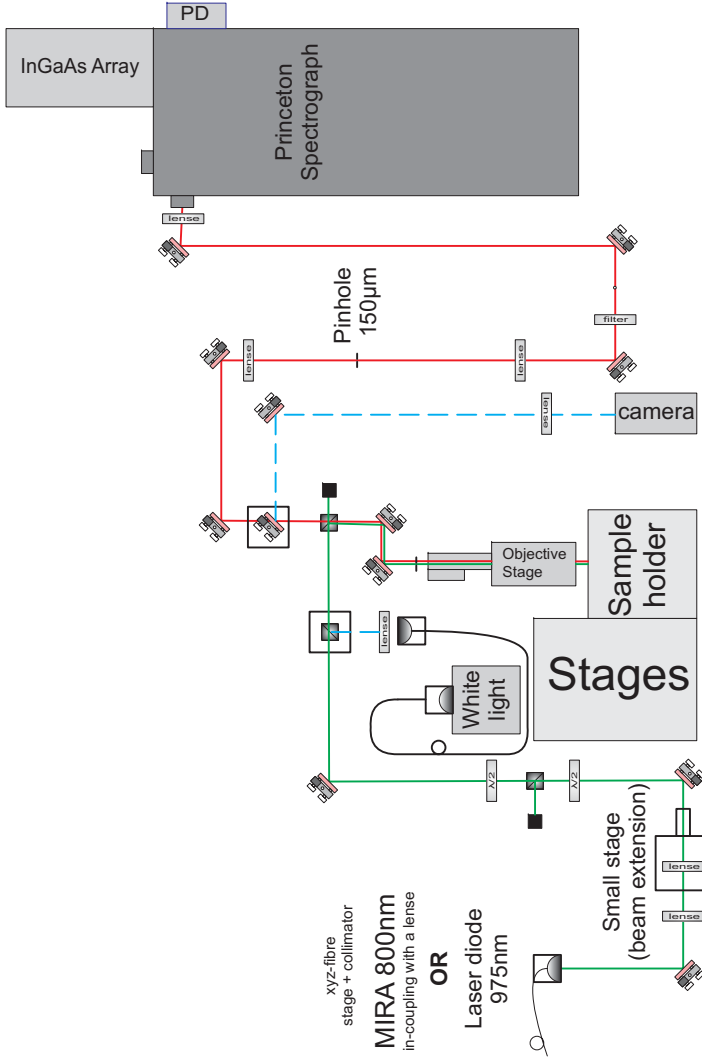
Figure 5.1: Micro-Pl setup to characterize InGaAsP PhC membrane structures. Green line indicates pump beam path, red line indicates beam path of the emitted light and blue line indicates beam path for optical inspection.

The setup described in section 4.1 was not suitable since it is optimized for wavelength between 900nm and 1 μm. The CCD detector after the spectrometer employed in this setup uses a silicon chip. Standard silicon chips are only sensitive to a wavelength of around 1 μm after which their quantum efficiency drops rapidly. Also, all of the optics (lenses and mirrors) are optimized for wavelength between 900nm and 1μm.

There are several differences between the two setups. The most important one is the detector. As already mentioned, the setup used to characterize the GaAs PhC membranes uses a silicon CCD. The setup used for the InGaAsP PhC membranes uses a cryogenically cooled In-GaAs linear array.

Apart from the fact that a linear array consists only of a single line of pixels and a CCD is 2D array of pixels the difference in detector material is important. InGaAs sensors are suited to detect at wavelengths between 0.8 μm and 1.7 μm. Unfortunately, InGaAs detectors are much more noisy than silicon (Si) detectors which are well known for extremely low dark counts.

In order to reduce the dark counts the InGaAs detector is cooled with liquid nitrogen. The detector can be cooled down to temperatures of 173 K. Increasing the temperature slightly by up to 40 K increases the sensitivity towards the long wavelength without drastically increasing the dark count compared to the deeply cooled state. Although deeply cooled, the dark counts are still orders of magnitude higher compared to cooled Si detectors.

The remaining components are described roughly in the order they appear along the beam path of the light in figure 5.1. Two different light sources are available for excitation of the sample. A laser diode for CW pumping at 975 nm and a Ti:sapphire laser with 800 nm center emission wavelength and a repetition rate of 80 MHz for pulsed pumping (pulse length: $\sim 1\,ps$). To easily switch between the two sources they are coupled by fibre into the setup.

The power of the diode laser can be directly controlled by changing the current that drives the laser. The light from the Ti:Sapphire laser can be partially blocked by neutral density (ND) filters before coupling it into the fibre that feeds the setup. A combination of a half wave plate and a polarizing beam splitter is used to fine tune the power. Light is coupled out of the fibre and collected by a small low NA objective. Two lenses and a small stage are used as Galilean beam expander to make sure the light completely fills out the input aperture of the microscope objective (5 mm FWHM beam diameter).

A pellicle beam splitter is used to separate the light used to excite the sample and the excited light emitted from the sample. The pellicle transmits around 95% of the light and reflects around 5% at an incident angle of 45 degrees. The fraction of light transmitted and reflected in a pellicle is largely independent of the wavelength. Only a small fraction of the excitation light is therefore used to excite the sample which also means that most of the emitted light is transmitted.

The objective is a 50X Mitutoyo Plan Apo NIR HR Infinity-Corrected Objective with a $NA = 0.65$, focal distance of 4 mm and a working distance of 1 cm. For easier control it is mounted on a small linear stepper stage to move it in focal direction. Despite being color corrected for wavelength from 480nm to 1.8 μm, the focal point needs to be slightly adjusted between white-light imaging to the camera and measuring at 1500 nm.

The stages used to move the samples are a combination of two types of stages. Large linear stages using a stepper motor for rough alignment (reliable step size ∼0.5 μm) with a long range of travel (50 mm) and mounted on those stages a set of smaller piezo stages with a short travel range (20 μm) and high accuracy for precise alignment (5 nm - closed loop operation). The linear stages can be moved in 100 nm steps but movement is not very reliable when taking such small steps.

The light is spatially filtered using two achromatic lenses and a small

lambda shift	pitch [nm]	radius [nm]	shift [nm]	target wavelength [nm]
1/4	472	185	112	1528
3/4	466	183	332	1549

Table 5.1: Structure parameters

pinhole of 150 μm to detect from an almost diffraction-limited spot on the surface of around 3 μm. The reflected light from the sources is filtered out with a long-pass filter before it is coupled into a 500 mm Czerny-Turner spectrograph. A low resolution grating with 300 lines/mm and blazed at 1000 nm was used to spectrally resolve the collected light and detect it with the aforementioned linear InGaAs array. The point detector on the other exit port of the spectrograph was used for alignment purposes.

5.2   Single photonic crystal cavity laser

5.2.1   Lambda-shifted PhC laser

An alternative type for PhC cavities, called lambda-shifted PhC cavities, is described in section 2.1.5. In this section photoluminescence measurements of lambda-shifted PhC lasers are shown. Measurements were taken in the setup described in section 5.1 under pulsed pump conditions using the Ti:Sapphire laser.

Two different lambda-shifted cavities with total shifts of 1/4 and 3/4 of their respective target wavelength in InGaAsP were investigated. Structures targeted at different wavelengths with different hole sizes, pitches and corresponding shifts were measured on, and the spectra shown in Fig. 5.2 were chosen so that the lasing mode is close to the maximum of the gain peak at $1520\,nm$ for both modes. Due to this, the parameters of the shown structures with the 1/4 and 3/4 shifts differ

lambda shift	calculated resonance frequency [nm]	calculated Q factor	calculated mode volume [$\frac{\lambda^3}{n}$]	measured resonance frequency [nm]
1/4	1526	1460	1.16	1526
3/4	1571	2500	2.48	1535

Table 5.2: MEEP calculation results

slightly from each other as can be seen in Table 5.1 where the values for the pitch of the undisturbed PhC lattice, hole radius, shift and target wavelength of both structures are summarized. The shown spectra are taken at powers around threshold and the peaks exhibiting lasing are marked.

In order to identify the measured resonances, the structures were simulated using the finite difference time domain solver MEEP[27]. A picture of the mode profile of the 1/4 and 3/4 lambda-shifted cavities can be found in Fig. 5.3a and 5.3b, respectively. The Q factors, mode volumes and calculated and measured resonances for both modes can be found in Table 5.2. Due to the complex nature of the PhC cavities, the underlying mode pattern of the cavities with a 1/4 and 3/4 shift differ from each other. There is an excellent agreement between the targeted, calculated and measured resonance wavelength for the 1/4 structure while for the 3/4 structure the agreement is rather poor. The mode identified for the 3/4 lambda-shifted cavity was the closest mode with an appropriate Q that was found in the simulations. The structures were simulated using perfect PhC patterns with hole sizes estimated from SEM images of the structures. The difference in resonance wavelength is mainly related to fabrication tolerances. Structures with a lambda shift of 5/4 were also fabricated but the calculations did not match with simulations sufficiently well to identify the dominant mode.

Figure 5.4 shows the linewidth as well as the shift in wavelength of the
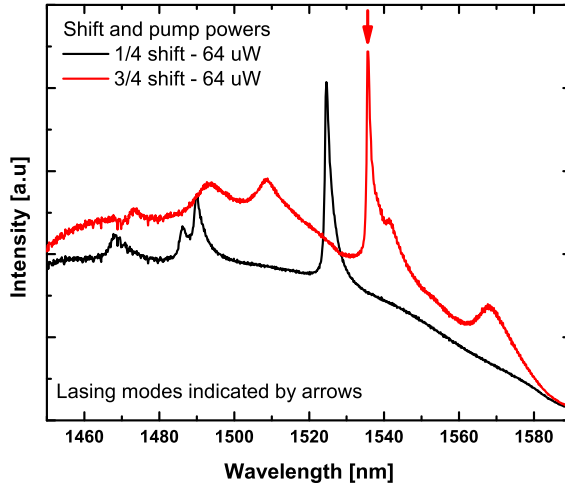
Figure 5.2: Spectrum for lambda shifted cavities with a shift of 1/4 and 3/4 lambda measured at the lasing threshold power.

peaks marked in Fig. 5.2 as a function of excitation power. The values are extracted by fitting Lorentzian functions to the peaks and correcting for the background. The power plotted in the top graph is the summed intensity of the fitted lines. The light-in-light-out (LL) curves clearly show lasing behavior of both peaks.

As can be seen from Fig. 5.4, the lines first narrow significantly towards threshold. Decreasing absorption loss with increasing pump power is causing the narrowing. At threshold the lines start to broaden again. It is expected in classical DFB lasers for the laser line to rebroaden at high powers due to effects caused by heating. This should be accompanied by a red shift of the cavity line. Although one of the lines does shift slightly towards the red at high pump powers, the rebroadening sets in at lower powers almost immediately after threshold. It is therefore likely
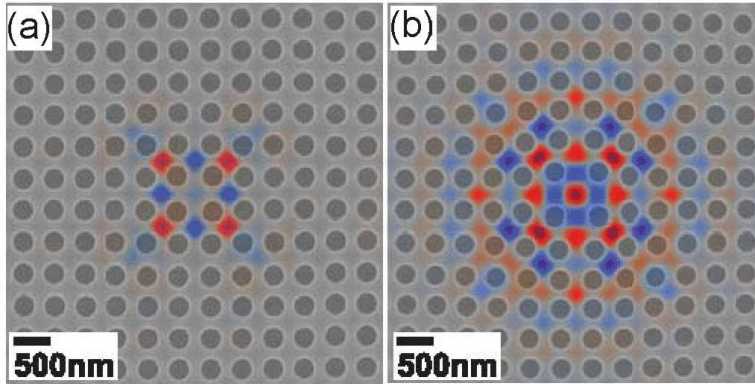
Figure 5.3: a&b) Lasing mode of the 1/4 and 3/4 lambda shifted cavity, respectively (real part of the magnetic field component perpendicular to the slab shown)

that a different mechanism is causing the rebroadening at these powers. Index fluctuations and non-equilibrium carrier distributions due to the pulsed pump schemes are possible causes. Recent results have shown that the emission from nanocavity lasers are chirped under pulsed pumping [90] and a similar mechanism has been shown to cause broadening in microdisk lasers [91]. Changes in the refractive index with increasing powers may also be responsible for the blue shift of the peaks.

Due to the changes in linewidth, it is difficult to determine a precise Q for our modes. At low powers, the line is broadened by reabsorption in the cavity, while at higher powers the cavity lifetime is modified due to stimulated emission [92]. The experimental Q value can therefore be estimated to be around 1000 at transparency. The large number of QWs used in the present demonstration results in a large free-carrier loss at threshold which masks the ultimately achievable Q of the present designs. Overall the measured Q factors of the cavities correspond to the calculated Q factors as can be seen in Table 5.1.

The cavities could be further improved by decreasing the mode vol-
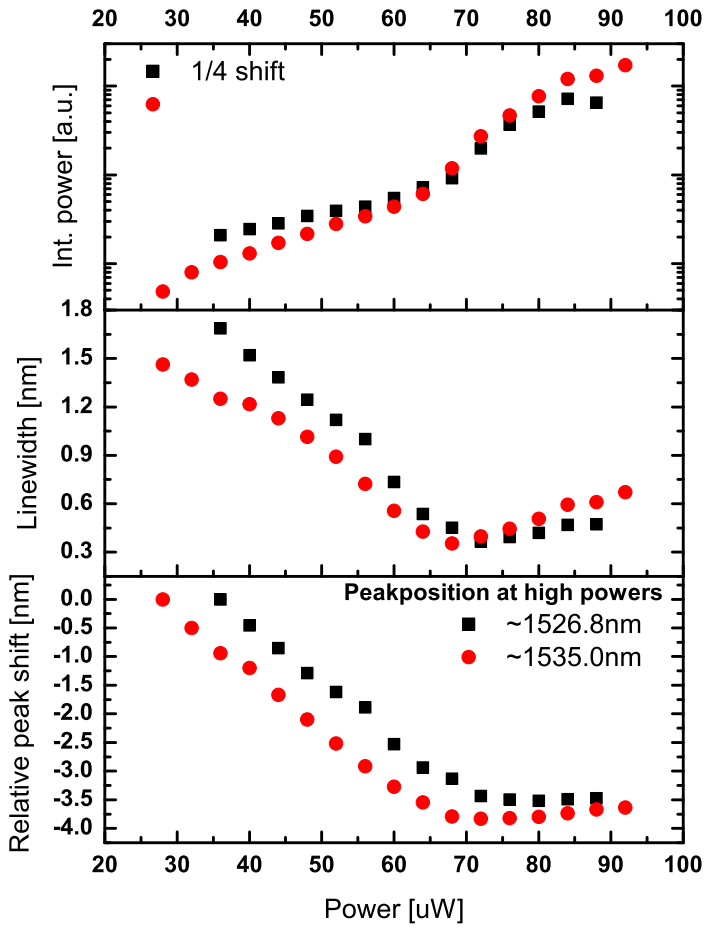
Figure 5.4: LL-curve, line width and peak position for different powers of the lasing modes of the lambda shifted cavities shown in figure 5.2.

ume. In order to do so it would be advantageous to target a monopole mode, but due to the symmetry in the quadratic lattice the structures seem to favor an octupole type of mode at the targeted wavelength. Calculations show that also a lower order monopole mode exists which has a different resonance wavelength than the target wavelength. By redesigning the structures it should be possible, though, to excite this mode.

5.2.2   Single defect H1 PhC laser in the quadratic lattice

In this section photoluminescence measurements from a quadratic lattice PhC with a single H1 defect are shown. The holes have a diameter of 361 nm and the lattice pitch is 453 nm. The structures were measured using the setup described in section 5.1 and the MIRA 900 was used for pulsed pumping. Spectra were taken at different pump powers and the main peak of the spectrum was fitted using a Lorentzian function and the background was corrected with a quadratic function.

Figure 5.5b shows the spectrum of the cavity emission at three different powers. Two modes are marked in the spectrum, a dipole mode at around 1575 nm and a quadrupole mode around 1530 nm. The modes can be distinguished by their relative position in the spectrum. The quadrupole mode has a very low intensity and is nearly indistinguishable from the noise. A smaller section of the spectrum for a pump power of 12 μW is therefor shown in figure 5.5b.

With increasing power the quadrupole mode disappears in the noise and the dipole mode increases in intensity. Figure 5.6a and figure 5.6b show the change in linewidth and the change in resonance wavelength of the dipole mode for different powers. Both plots also show the peak height of the fitted peak. It can be clearly seen that the cavity is lasing with a threshold around 20 μW.

Linewidth and peak position show a similar behavior as the lambda shifted cavities in section 5.2.1. The linewidth starts to broaden again
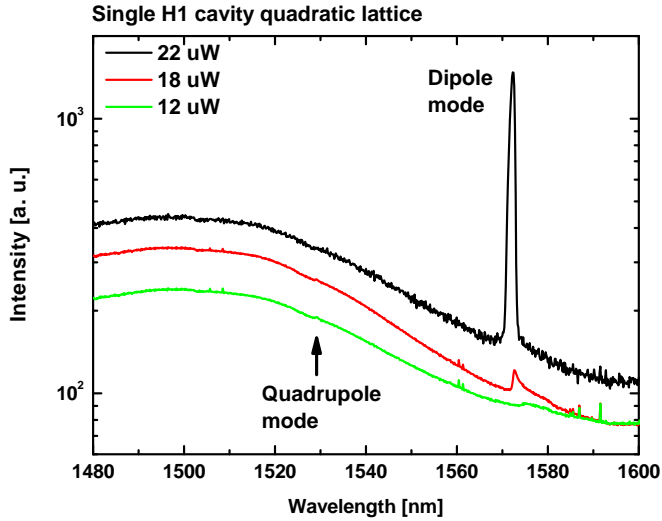
(a) Spectra of a single H1 cavity at different pump powers. Dipole and quadrupole mode are indicated.
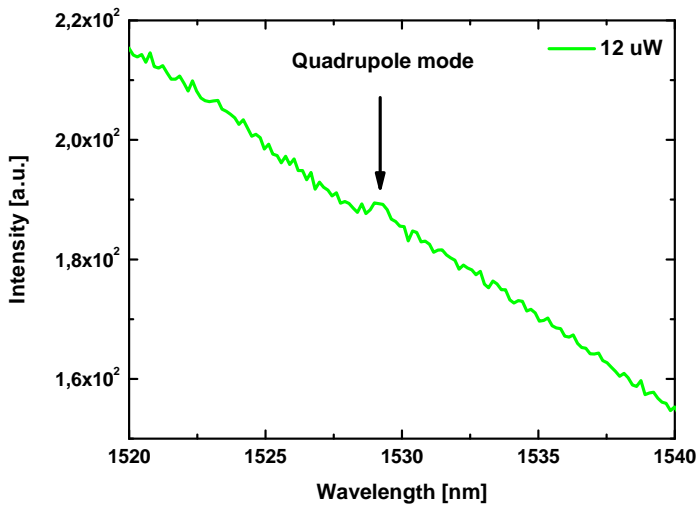
(b) Zoom in of the H1 cavity spectra at a pump power of 12 μW mode. Arrow indicates the quadrupole mode which is not visible in the spectra in figure 5.5a.

Figure 5.5
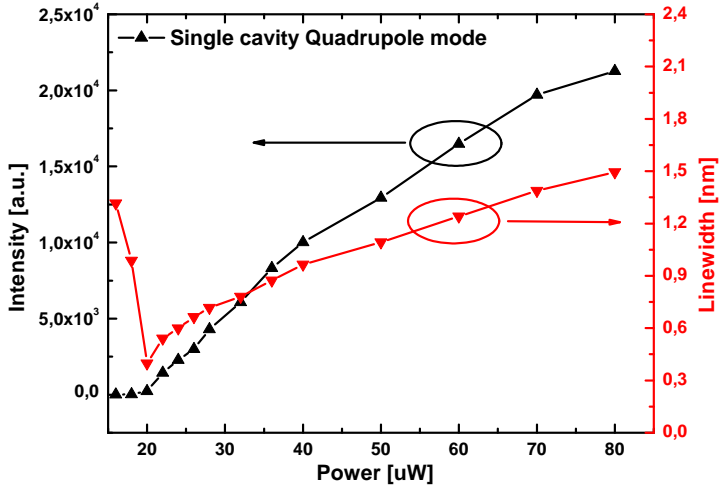
(a) Linewidth
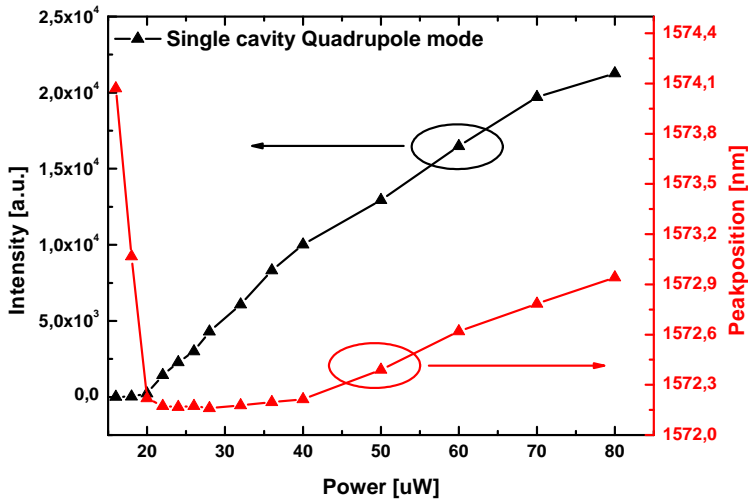
(b) Peak position

Figure 5.6: Changes in linewidth and peak position plotted together with the LL-curve of the dipole mode of the H1 cavity in the quadratic lattice shown in figure 5.5a.

above threshold due to chirping effects [90] and the cavity resonance
wavelength undergoes a blue shift until threshold and than red shifts at
higher powers probably due to heating effects.

It is unclear why the dipole mode starts to lase and the quadrupole
mode does not even at very high powers. The dipole mode in the
quadratic lattice has a very low theoretical Q as can be seen in chapter
2. Also the following measurements for the coupled cavities clearly show
the low Q of the dipole modes as can be seen in figures 5.7 and 5.9.
Furthermore, the dipole mode is far removed from the maximum of the
gain peak. The quadrupole mode has a higher theoretical Q as well as
the mode being better aligned with the gain peak.

The position of both modes is in good agreement with the position
of the modes in the coupled-cavity structures presented in sections 5.3
and 5.4 with similar hole sizes and pitches. The most likely, although
not very satisfying, explanation is therefore a fabrication error. It is
very unfortunate that the quadropole mode does not show lasing since
the dipole mode doesn't show lasing in any of the subsequent coupled
cavity structures. It will therefore not be possible to directly compare
the single cavity with the coupled cavity systems.

5.3   Lasing of two coupled photonic crystal cavities

Structures measured in this section are similar to the structures shown in
section 4.2 figure 4.2a. In this section measurements of two coupled H1
cavities in a quadratic PhC lattice with an intrahole spacing of two holes
in the Γ-X direction are presented. As for the single cavity structure,
the holes had a diameter of 361 nm and the lattice pitch was 453 nm.
Measurements were taken in the setup described in section 5.1 under the
same pulsed pumped conditions as the structures in section 5.2.2.

The spectra of the cavities presented in figure 5.7 are similar to the
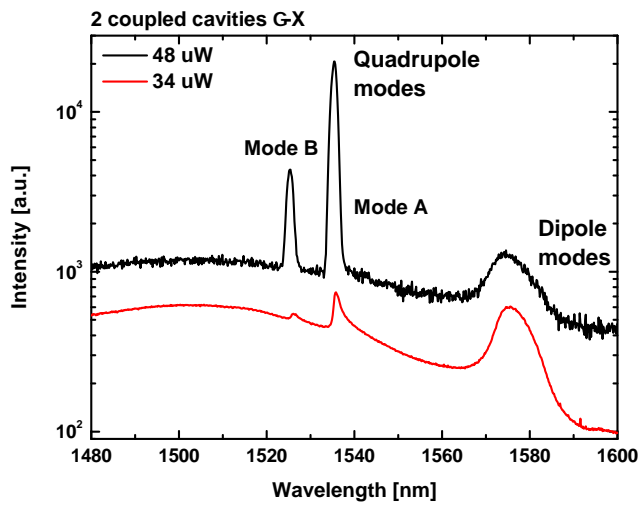
Figure 5.7: Spectra of two coupled H1 cavities in the Γ-X direction with an intracavity spacing of two holes for pump powers below and above threshold. Both quadrupole and dipole modes are visible.

spectra presented for two coupled cavities in section 4.2.1. Two coupled modes are measured. The spectral split, which can be seen in figure 5.8b, is slightly larger than for the structures presented in section 4.2.1 and can be evaluated to be ∼9.5 nm at low powers. Both lines are shifting with power slightly changing the amount of spectral splitting. The difference between the spectral splitting for these structures presented here and the structures presented in section 4.2.1 can probably be explained by fabrication tolerances.

By looking at the L-L curve presented in figure 5.8 it is clear that both cavities start to show threshold behavior at similar powers of around 40 μW. Both modes undergo the same behavior concerning changes in resonance wavelength and linewidth as other nanocavities presented in this chapter. The changes are shown in figure 5.8a and 5.8b respectively. The reason for this behavior can be assumed to be the same as presented before in section 5.2.1. To determine linewidth, peak intensity and resonance wavelength the peaks were fitted using a Lorentzian function and the background was corrected with a quadratic function.

Spectra for the cavities at powers slightly below and above threshold are shown in figure 5.7. Besides the two coupled quadrupole modes around 1530 nm also a large hump caused by coupled dipole modes can be seen around 1575 nm. The dipole mode does not exhibit threshold behavior even under high powers. It is important to note that both modes show lasing around the same threshold.

5.4   Large array photonic crystal cavity laser

In the two previous sections, section 5.2.2 and 5.3, single and two coupled H1 defects in quadratic lattice PhCs are examined. In this section measurements on larger arrays are presented. Two by two and eight by eight coupled cavities with an intrahole spacing of two holes are presented. SEM images of coupled cavity arrays can be found in section 4.3 figure
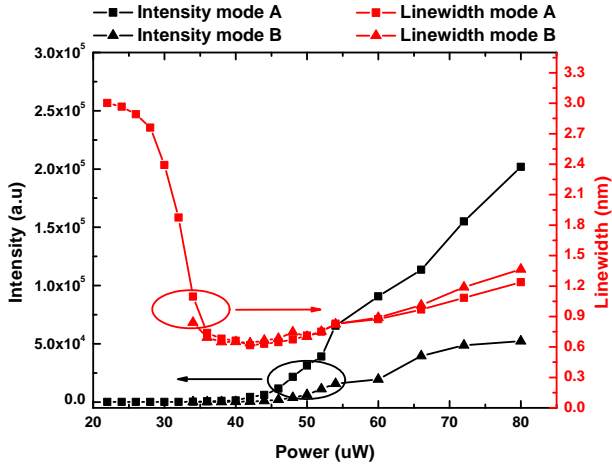
(a) Linewidth
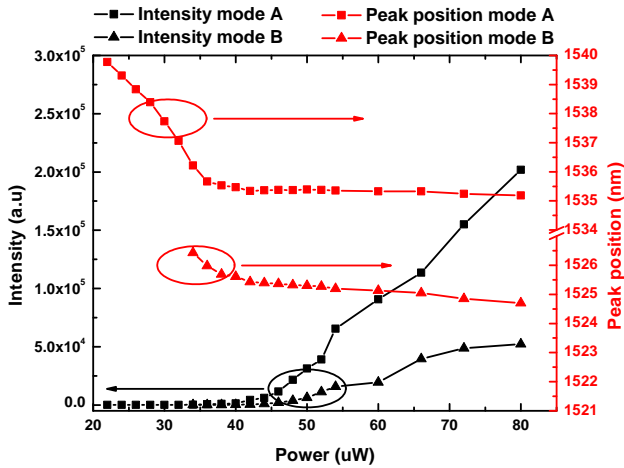
(b) Peak position

Figure 5.8: Changes in linewidth and peak position plotted together with the LL curve of the two coupled quadrupole modes shown in figure 5.7. Both modes seem to lase.
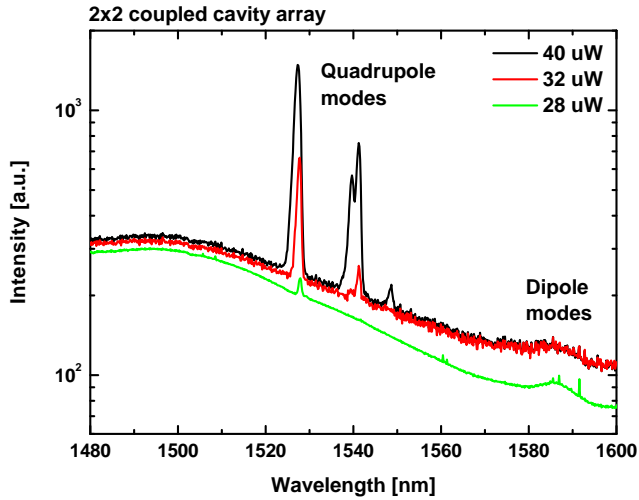
Figure 5.9: Spectra of two by two coupled H1 cavities at different powers. The four coupled quadrupole modes are visible as sharp peaks around 1530 nm. Small hump at 1590 nm indicates the position of the coupled dipole modes. At least three of the four quadrupole modes show lasing behavior.

4.9. The main question is how will the increase in cavities change the threshold behavior and how do the structures behave when they reach threshold.

Figure 5.9 shows the spectra emitted by an array of two by two coupled cavities. Like for the single cavity and two coupled cavities, the holes have a diameter of 361 nm and the lattice pitch is 453 nm. Two overlapping peaks around 1540 nm are flanked by two peaks to either side at around 1530 nm and 1550 nm. In theory, according to section 2.2.2 only three peaks, should be visible in the spectrum. Due to fabrication tolerances the degeneracy of the two center modes is lifted and four peaks are visible.

At low powers only the mode at the shortest wavelength is visible. With increasing power all four modes appear in the spectrum. A slight hump around 1585 nm indicates the position of the dipole modes in the spectrum. The relative height of the hump should not be compared to the quadrupole though since the detector sensitivity should drop off around the same wavelength and there should be very little gain at that wavelength.

Only the dominant peak is fitted to extract peak height, linewidth and peak position. As in the previous sections the line is fitted with a Lorentzian and the background is corrected with a quadratic function. As can be seen in figure 5.10, the cavity undergoes the same behavior as all the other lasing modes presented here so far. A detailed explanation for this is given in section 5.2.1. The threshold can be estimated to be around 28 μW.

Although the other modes are not fitted, it is clear from looking at the spectrum in figure 5.9 that they are also above threshold for higher powers. Before analyzing the large array with eight by eight cavities, some conclusions should be drawn from the comparison between the two coupled cavities and the array of in total four coupled cavities. In both cases more than one mode shows threshold behavior. While the peaks are distributed as can be expected from theory it is difficult to measure the peaks below threshold due to their low intensity.

This is very different from the behavior of the structures presented in chapter 4 and again points to a large free carrier loss due to the large number of QWs used in the membrane and the operation at room temperature. In chapter 4 the gain material used is QDs and the structures are measured at low temperatures. The dots will act as single emitters in this case and each mode will be pumped by a separate set of dots. Another problem is also due to the large number of wells a lot of emission is coming from the background which masks the modes unless they are strongly enhanced by for example stimulated emission.
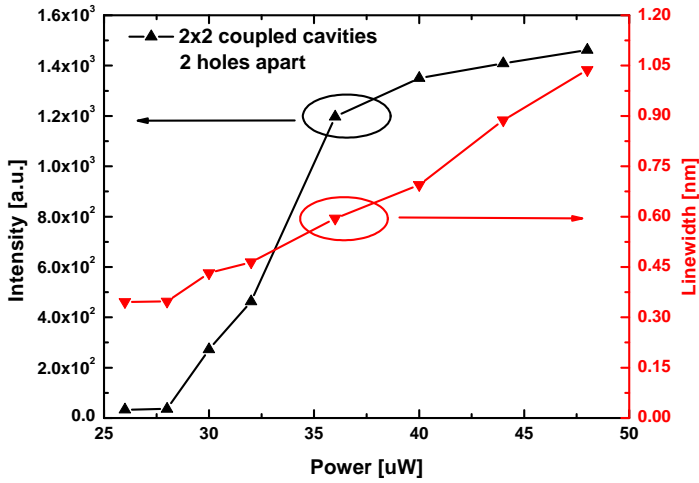
(a) Linewidth
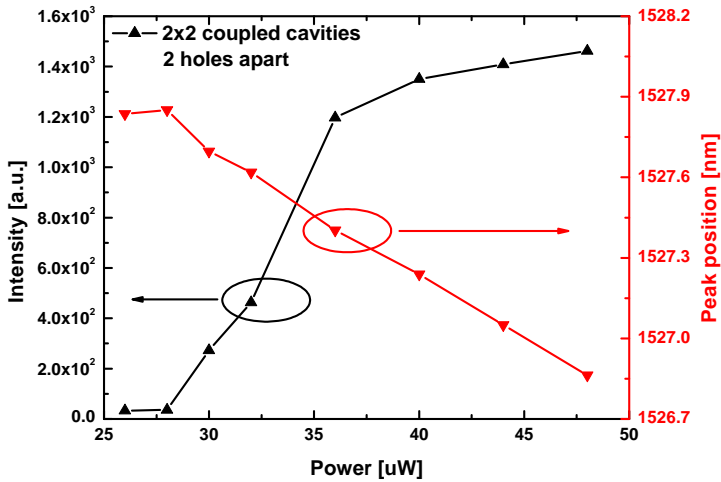
(b) Peak position

Figure 5.10: Changes in linewidth and peak position plotted together with the LL curve of the dominant coupled quadrupole mode at 1527 nm shown in figure 5.9.

Ishii *et al.* [88] measured on coupled cavities they dubbed photonic molecules. The coupled cavities in this case are shifted hole defects (H0) or one missing hole (H1) defects in the triangular lattice. In their structures there is a significant difference of a factor of two between the threshold of a single cavity and of two coupled cavities. They reasoned that this is caused by the fact that the gain is divided between two modes in the coupled structure and therefor a higher pump power is required to bring the structures above threshold.

Comparing the threshold between the two coupled cavities (40 μW) and the four coupled cavities (25 μW) for the structures presented here shows that the threshold for the main mode in the four coupled cavity structure is lower than for the two coupled cavities which differs from the results presented by Ishii *et al.* [88]. The conclusion made by Ishii *et al.* is also rather surprising since not only the number of modes increases with the number of cavities but so does the amount of gain material. The gain is not directly influenced by the total integrated power but by the power density of the pump spot which strongly depends on the spot size and the position of the spot. Differences in threshold are therefore more likely to be caused by the pump scheme used.

Fabrication tolerances influence the Q of the coupled modes which can change the threshold but the threshold itself should not be dependant on the number of cavities as long as the pumping is relatively uniform across the structure and the cavities are weakly coupled with each other. Altug *et al.* [1] reported that for their structures, which are similar to the ones presented here, the increase in threshold between a large number of coupled cavities (64) and a single cavity corresponded to the change in spot size which was enlarged to more uniformly pump the structures.

Figure 5.11 shows the spectrum of a large coupled PhC cavity array with eight by eight cavities for different powers. The diameter of the holes and the lattice pitch of the PhC are 388 nm and 486 nm, respectively. The sizes are estimated using SEM images of the structure. The inset of
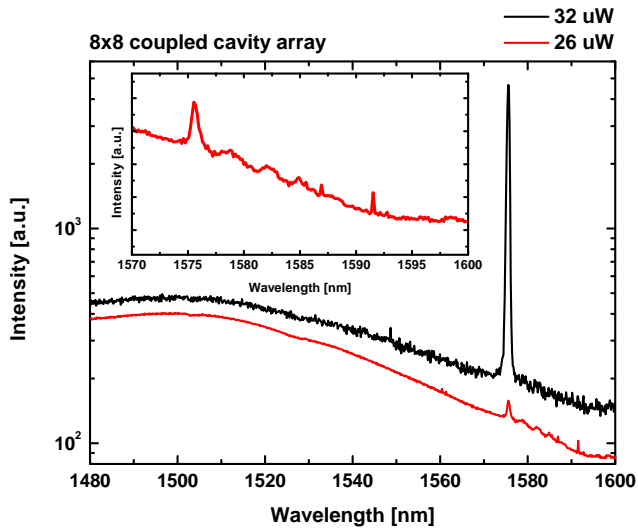
Figure 5.11: Spectra of eight by eight coupled H1 cavities taken in the center of the array for powers below and above threshold. Inset shows zoom in of the area close to the lasing mode at a power of 26 μW below threshold. Small peaks indicate other coupled modes close to the main peak. Above threshold other modes seem to be suppressed.

figure 5.11 shows a part of the spectrum close to the cavity at a power of 26 μW. There are clearly several modes which can be seen although the mode with lowest wavelength seems to be dominant. At higher powers only the dominant mode is visible.

The measured modes are quadrupoles. The reason that they are shifted in wavelength compared to the quadrupole mode for the single, two coupled and four coupled cavities is due to proximity effects which are explained in detail in appendix B. This shift warrants a bit of discussion because the reason cannot be explained solely by proximity effects, but also the specific way the sample is designed has to be taken into account. The discussion is important to clearly show that the modes are indeed quadrupole modes.

All the structures on the sample measured in this chapter are designed with ten holes surrounding the cavity/cavities. Since a different number of cavities are used in different structures, this causes the total size of the PhCs to differ. The single cavities are formed by 21 by 21 holes with the central hole obviously missing to form the defect. The two coupled cavities are 24 by 21 holes and the four coupled cavities are 24 by 24 holes with holes in the center missing to form the defects. All of them are similar in size and have therefor similar hole sizes.

The 8 by 8 cavities are formed by a PhC with a total of 42 by 42 holes. This means that the hole sizes, which were designed to be the same during e-beam writing, will be larger in the 8 by 8 PhC cavity structure. This seems straightforward but there is a catch. Larger hole sizes usually lead to shorter emission wavelength since the cavities becomes smaller. The emission wavelength of the quadrupole mode for a single cavity is around 1530 nm while the main mode in the 8 by 8 coupled cavities emits around a longer wavelength of 1575 nm.

Each structure, like the single cavities, are not only fabricated once on the sample, but with several different combinations of lattice pitches and hole sizes. For the single, two coupled, and four coupled cavities,

the same combination of hole radius and lattice pitch is measured on. For the 8x8 cavities, this was not possible since the hole size is changed so much for that particular lattice pitch that it does not show emission anymore. Instead, a completely different combination of radius and hole size is applied.

Comparing the r over a value of the single cavity ($\frac{r}{a} = \frac{180.5}{453} \sim 0.398$) with the eight by eight cavities ($\frac{r}{a} = \frac{194.5}{486} \sim 0.400$) shows that the emission of the cavity should shift towards the longer wavelength as can be seen in the measurements. Therefore, the modes measured are quadrupole modes and not dipole modes which should be shifted to even longer wavelength outside the sensitivity of the InGaAs array.

In figure 5.12 peak height, linewidth and peak position of the dominant quadrupole mode in the 8 by 8 coupled PhC cavity array are shown for different powers. Again, the parameters are extracted by fitting a Lorentzian to the mode for each spectrum and the background is corrected using a quadratic function.

The threshold is around 30 μW. Changes in the linewidth and peak position are similar to the ones exhibited by all the other lasing modes presented in this chapter which strongly indicate that these changes are indeed, as discussed in section 5.2.1, mostly connected to the gain material.

One of the important results published by Altug *et al.* [1] is the claim that there is an increase in emission per cavity by comparing the output from a single cavity with the output of a large number of coupled cavities. Unfortunately, the same comparison cannot be made with the data presented here for several reasons. First of all the single cavity showed only lasing for the dipole mode and not for the quadrupole mode. Secondly, in order to collect all the light from the whole array the collection spot needs to be large enough. The setup used for the measurements in this chapter works at the diffraction limit and spatially filters the light which is collected from the surface. The collection spot is around 3 μm
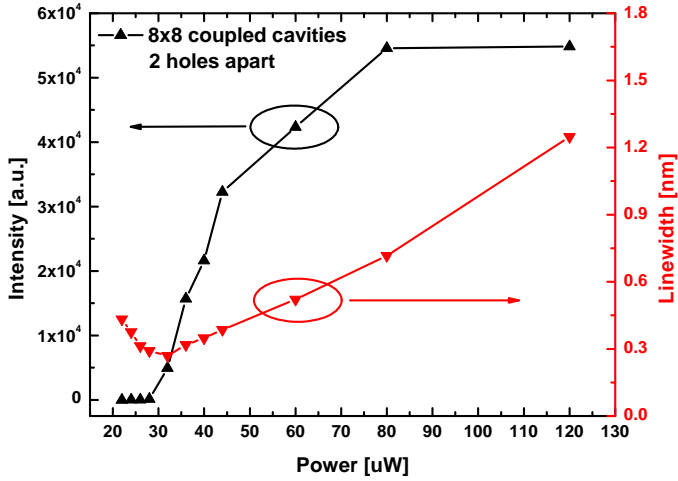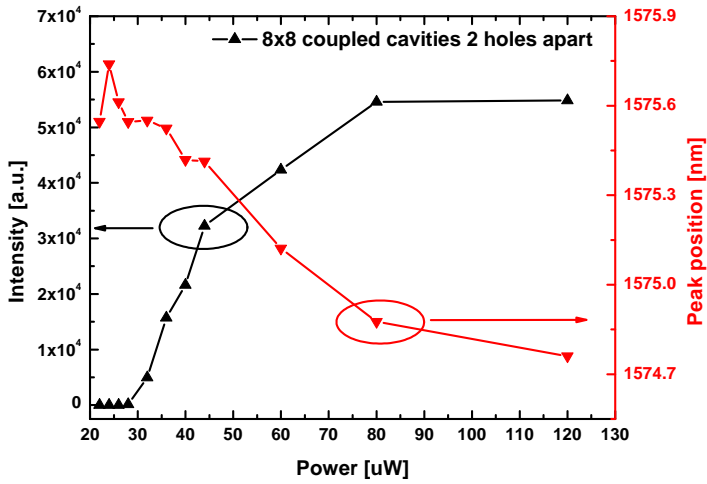
(a) Linewidth

(b) Peak position

Figure 5.12: Changes in linewidth and peak position plotted together with the LL curve of the dominant coupled quadrupole mode shown in figure 5.11

in diameter, while the cavities span over an area of around 10 by 10 μm, which means that only part of the light emitted from the array is collected assuming the emission from the array is uniform.

There is also an underlying issue which makes such comparisons difficult even when the collection spot is large enough. The emission profile of the large cavity structure might look different then that of a single cavity and therefore the collection efficiency of the optical system used to collect the light might differ strongly and depend on which supermode is emitting. To make that comparison either farfield calculations or measurements showing that most of the light emitted from either structure is collected are required.

There are three different structures that showed lasing for the quadrupole mode. The two coupled cavities, the two by two coupled cavity array and the large eight by eight coupled cavity array. In principle they can be compared but the problem with the collection spot mentioned above still makes it questionable to directly compare the large coupled structure with the few coupled cavities. Besides this there is also the issue mentioned earlier that the large coupled cavity array emits at a much longer wavelength further removed from the gain peak then the other two structures which makes a direct comparison even more questionable.

After excluding most possibilities of direct comparisons there is at least two structures which can be directly compared, the two and four coupled cavities emit roughly at the same wavelength and are both within the collection spot. There is more than one mode though that shows threshold behavior. Comparing both modes lasing at the lowest wavelength the two coupled cavities actually showed a larger amount of emission than the four coupled cavities. Obviously the gain is spread over all the modes which show lasing and not just a single mode which makes it difficult to judge whether the overall emission actually increases or not. In conclusion the data does not allow to verify or contradict the claims made by Altug *et al.* regarding the increase in emission power.

The fact that the structures do support multi-mode lasing for only a few coupled cavities is interesting in itself though. Altug et al. [1] reported that in their structures with eight by eight coupled cavities even at low powers no further modes could be found. The reason for this is the poor sensitivity of the optical spectrum analyzer they used compared to the cooled InGaAs array used for the measurements here. The inset in figure 5.11 clearly shows a few other modes close to the dominant mode at a power below threshold. This is also in agreement with the measurements done on the membranes with QDs as gain material in section 4.3 and should be expected from the simulations in section 2.2.2 as well as from coupled mode theory.

The coupled cavity structures presented here are inherently multi mode and the reason they can show single mode behavior above threshold is due to gain quenching effects. The question though is why do the modes for the few coupled cavities do not show the same amount of gain quenching. It seems as if with an increasing number of coupled modes the gain quenching effects become stronger. For the two coupled cavity structure both modes show lasing around the same threshold as can be seen from figure 5.8 while in the four coupled cavity structure the threshold for the modes differ as can be seen from figure 5.10. The large coupled array is single mode above threshold.

The main difference between the structure is the increased overlap of the modes as was shown in section 4.3. Due to the overlap a band is formed and lasing is favored to occur at the lower band edge similar as in defect-free PhC band-edge lasers [93, 94]. This does not explain the reason though why a few coupled cavities show multi mode lasing except that it must be connected somehow to the difference in the mode structure.

As a last remark, a qualitative comparison of the beta factor between the two coupled cavities, two by two coupled and eight by eight coupled cavities can be made. The more cavities are coupled, the more

pronounced the kink in the lasing threshold becomes indicating that the beta factor decreases [19]. This can be seen by comparing figures 5.8a, 5.10a and 5.12a. The reason for this is that the mode volume increases with an increased number of cavities. It can therefore be expected that this trend continues with an increasing number of cavities which effectively limits the number of cavities that can be coupled before the laser looses its high beta factor.

Chapter 6

Conclusion

"Now we just have to find the journal of reproducible results and publish it." - Professor at DTU Fotonik

In this chapter the main conclusions of the thesis will be summarized. The conclusion drawn from the fabrication process and the optical characterization of the structures are presented separately.

Fabrication of PhC structures

Despite being difficult to work with, mixtures of CH_4 and H_2 can be used to fabricate PhC lasers in InGaAsP and GaAs using a conventional RIE. The main limitation in the etching process is neutral shadowing which limits the smallest hole diameter that can be etched to around 150 nm and causes the etch rate to be largely dependant on the feature size. Holes of roughly 250 nm diameter were fabricated with sidewall inclinations of around 92 degrees in GaAs and 90 degrees in InGaAsP.

The etch rate this process can be increased by almost 20 % by using an InP carrier with an appropriate size. In this case small pieces of roughly 1 cm^2 patterned with PhCs were etched with a quarter of an full 2 inch InP wafer as carrier. This is also the case when etching a material that differs from the carrier like GaAs. Etching directly on the quartz

plate or using a 2 inch GaAs carrier wafer yields an even smaller etch rate then when using a full 2 inch InP wafer. The reason for the increase in etch rate is a change between the ratio of ions and CH$_3$ radicals during the etch process.

A hard mask of Si$_3$N$_4$ was used to etch the PhCs. The mask was defined using ZEP as e-beam mask on top of the Si$_3$N$_4$ and etched with a CHF$_3$/O$_2$ plasma. During the etch a chemically inert film forms on top of the ZEP resist that can't be removed using an oxygen plasma or heated microposit remover 1165 with ultrasound. The film is non-uniform and distorts the pattern that is etched and thereby degrades the quality of the PhC. Thickness and non-uniformity of the film increase at higher powers and oxygen ratios. The quality of the etch can therefore be improved by lowering the oxygen ratio and power. To remove the film it is necessary to place the sample vertical in the remover in order to avoid it from clinging to the surface.

Characterization of PhC structures

PhC cavities using QDs or QWs as gain medium were fabricated and mainly the quadrupole mode of the H1 cavity in the quadratic lattice was investigated. Due to the inherent low Q of around 1000 of the mode it is not possible to achieve lasing in the QD structures but lasing is seen for the QW structures.

It is shown that the spectra of coupled H1 cavities in the quadratic spectra behave as can be expected from coupled mode theory and agree with calculations. The difference in distance between coupled cavities in the Γ-X and Γ-M direction causes the modes to preferentially couple in Γ-X direction. This is shown both in theory and experiment through the spectral splitting between the coupled modes from two coupled cavities. The splitting is more than two times larger in the Γ-X direction than in the Γ-M direction for the same number of intracavity holes.

The two coupled cavities and the small array of two by two cavities show multi mode lasing while the large coupled array of eight by eight

cavities is single mode. The reason for this is not entirely clear but is somehow connected to the formation of an optical band for the large coupled structure. It was not possible to verify or contradict the claims made by Altug *et al.* whether there is an increase in output power per cavity when coupling more cavities with each other due to various reasons but foremost because of the multi mode behavior of the few coupled cavity structures.

The super modes that form in the coupled cavity structures though will increase in mode volume when the number of cavities is increased. Coupling more and more cavities in order to increase the output power will therefore result in a laser that has the same properties as a conventional diode laser but a much more complicated structure.

The structures are inherently multi mode and this makes uniform pumping very important. Electrically pumping a single cavity PhC laser is already very challenging due to problems with the current injection. Doing the same in a uniform manner in a coupled cavity structure seems unfeasible at the moment. On top of this because of the short optical pulses used to pump the structures, some serious questions were raised by other research groups concerning the high speed modulation shown by Altug *et al.*.

In conclusion to the question raised in the introduction of the thesis, PhC cavity lasers are not likely to become the next step in the evolution of high speed semiconductor lasers for telecommunication applications. It is possible though to reach ultra-low thresholds in these structures but there seems to be an inherent trade off regarding the output power and the mode volume. It is not apparent why there should be some sort of sweet spot that makes these structures inherently better then other PhC structures with a similar mode volume. In fact it would be very interesting to see if a not-coupled PhC cavity laser with a large defect and a similar total mode volume would show the same properties as a large coupled cavity array.

Despite this a possible application of PhC cavities are still optical circuits. The lambda shifted cavities presented in the thesis are an attempt to create a cavity that could be used for such a kind of application.

Appendix A

Hole widening

An important issue in the fabrication is to control the size of the holes of the PhC. Ideally the holes should be the same size as specified in the design file for the e-beam writer. This is usually not the case. Almost all subsequent steps in the process tend to widen the holes. Effectively there will be a hole widening that has to be taken into account when creating the design files. The sources of hole widening are listed below and then discussed in detail for the fabrication of PhCs in GaAs. The effective hole widening for the PhC in the InGaAsP membranes was around 40 nm in total when using a dose of 200 μC in the e-beam and around 50 nm for GaAs using optimized process described in chapter 3.

1. Development of the resist

2. Proximity effects during exposure

3. Etching of the hard mask

4. Etching of the membrane

Both for the definition of PhC patterns in GaAs and in InGaAsP ZEP 520A is used as an e-beam resist. The developer used to develop the resist is ZED-N50. Since both etch steps will widen the hole it is
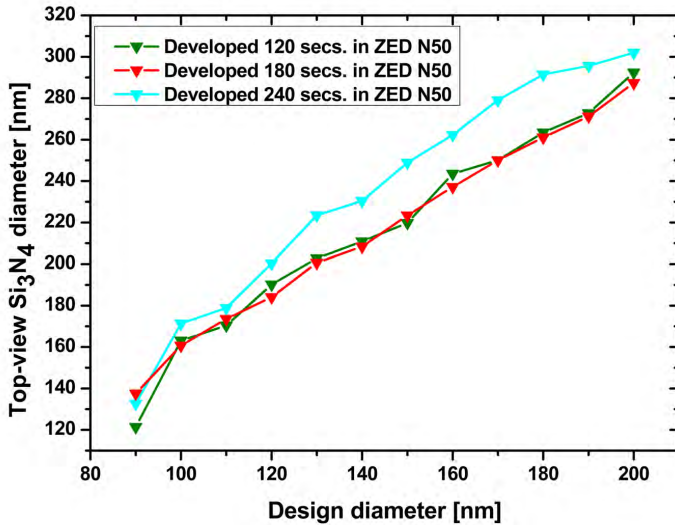
Figure A.1: Changes in the hole size after the development process. Hole sizes were measured in the Si3N4 mask after all samples were etched for 16 minutes with the Si3N4std program.

more important to make sure that the development process is stable and that small changes in the development time do not drastically change the size of the holes then to make sure that they are exactly the same size as in the design.

Although the holes widen after four minutes further for the used development time of two minutes the process is stable as can be seen in figure A.1. Because it is difficult to accurately measure the hole sizes in the resist the holes are etched first into the Si_3N_4 and then measured. The problem in measuring arises due to fact that the mask charges up in the SEM.

After making sure the development is stable the widening due to the subsequent etch steps can be measured. The reason that the hole size
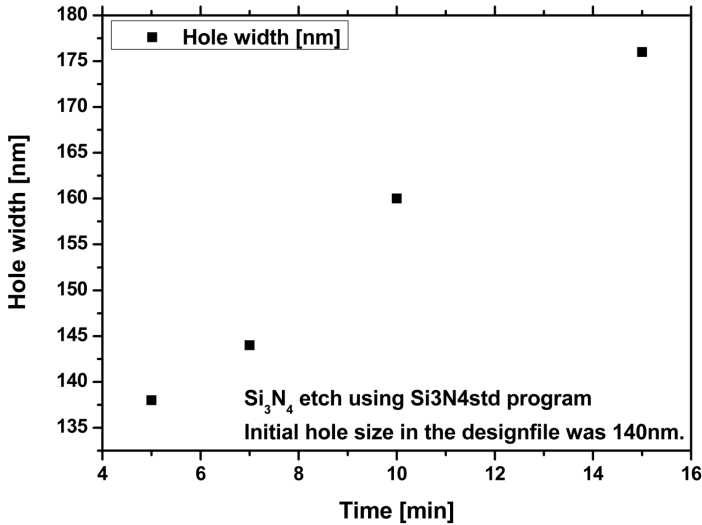
Figure A.2: Widening of the hole in the glass etch during the optimized process using the "Si3N4std" recipe.

increases during the etch is related to the fact that in the RIE also the mask is etched with a finite rate. During the etch the mask erodes at the holes edges and widens.

When the mask widens the underlying material is also etched and the hole becomes larger. This is the case for the Si3N4 etch as well as the GaAs and InGaAsP etch. Figure A.2 shows the widening of the hole in the Si_3N_4 mask during the CHF_3/O_2 etch. and figure A.3 the widening after the GaAs etch for several different hole sizes.

The etch has only been described here in terms of what happens to size of the hole. Of course also the profile of the hole changes with different etch times. It can sometimes be advantageous to slightly overetch a sample as it is the case with the Si_3N_4 etch in order to get a better profile. If this results in a hole widening it is just a question to adapt the
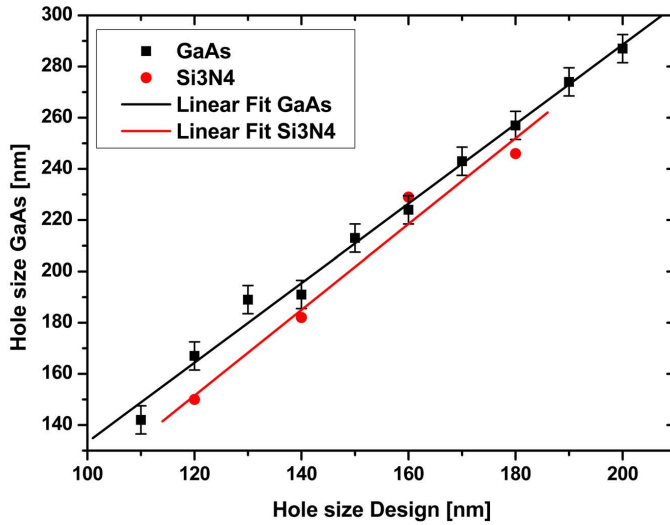
Figure A.3: Widening of the hole in the III-V etch during the optimized process using the "cyc8" recipe.

design according to the measured hole sizes. Hole widening is therefor not necessarily something bad in the process but it needs to taken into account.

Appendix B

Proximity effects in ebeam writing

In e-beam writing proximity effects are well known [95]. Due to these effects areas close to exposed structures receive a dose high enough to become developed even though they weren't directly exposed. This causes the pattern to become washed out because structures become enlarged and small gaps between structures close.

The e-beam writer used at Danchip is a JEOL JBX-9300FS electron lithography system with an acceleration voltage of up to 100kV. The writing field is 500 μm by 500 μm large and the stitching and field overlay accuracy is below 30 nm [61]. Patterns are written point by point.

The e-beam has a specialized hardware that converts a few basic shapes (trapezoids and triangles) into exposure patterns. These patterns are decomposed into different points to fill out the shape that needs to be exposed. Each point is assigned a specific dwell time depending on how many points and how high the dose is, that is used to expose the pattern.

The number of points per pattern is defined by the step size which can be as small as 1 nm. There is a limit to the number of points set by

the maximum speed that the beam can be moved with. The minimum dwell time is 40 ns [61]. The dwell time depends mainly on the specified dose. The dose is measured in μC per cm^2 and defines the energy density with which the e-beam nominately exposes the pattern. Unfortunately the e-beam itself does not take into account proximity. Therefore differs the energy density that the resist is actually exposed to in total from the one specified by the dose.

An example of proximity effects can be seen in figure B.1 for HSQ which is a negative tone e-beam resist. The holes of the PhC are only barely visible on the lower left hand side of the large blob in the picture although they should have been written throughout the structure.

Proximity effects are caused by two different mechanisms. The first is the forward scattering of the electrons when the e-beam hits the resist. For large acceleration voltages (100kV) this effect is usually quite small and has a range of less then 5 nm. This is only of concern when the feature sizes are extremely small and not relevant for the PhC structures described in this thesis.

The second is the backward scattering of electrons after they have passed through the resist and are scattered back into it. While the forward scattering is mainly dependant on the beam acceleration and the properties of the resist the backward scattering also strongly depends on the substrate. The effect can reach tens of microns in GaAs and InP. Values of roughly 20 microns were measured as well as simulated for the GaAs structures used in this thesis.

Proximity effects are automatically present when making a dose test. A dose test is done by exposing a small part of the pattern which contains the critical features with different doses. The samples are then developed and inspected to determine the best dose.

This method can be used to overcome proximity effects as long as the pattern is fairly uniform and the backscattering can be assumed to also be uniform throughout the structure. As soon as the pattern has
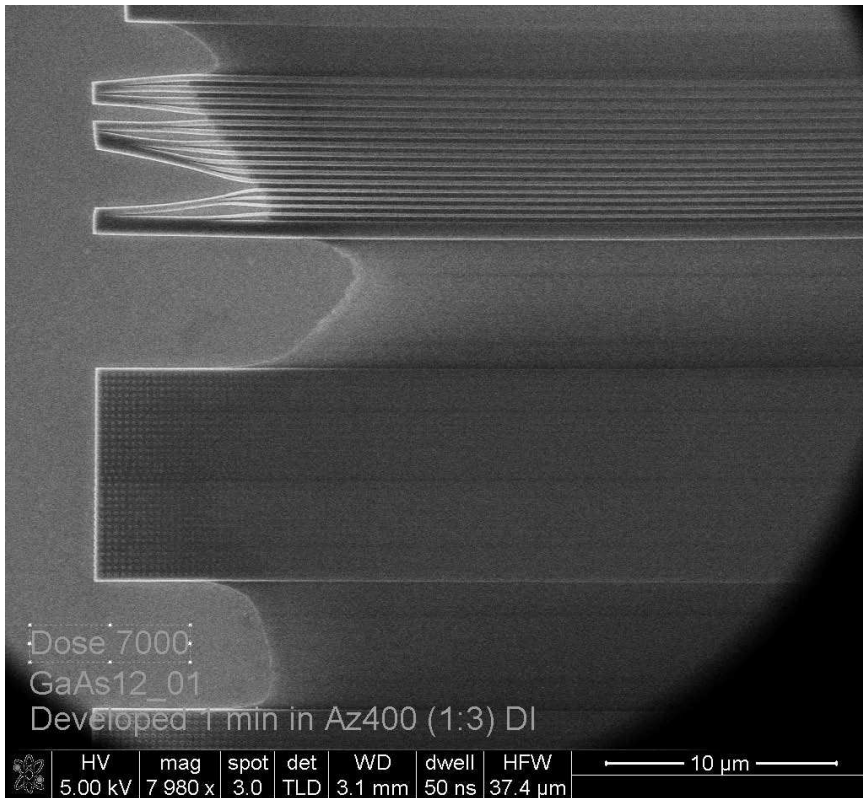
Figure B.1: Proximity effects shown on a pattern exposed in Fox12 (HSQ) with a dose of 7000 uC/cm^2 an developed for 1 min in 1:3 AZ400:DI. Fox 12 is a negative ebeam resist.

dense as well as isolated structure the dose cannot be globally adjusted in this way since either the isolated structures become underexposed or the dense structures overexposed.

Another problem is that without correction the edges of the structures will always be underexposed when using a dose that is correct for the center of the structure. PhCs are usually fairly uniform and since the reflections from the most outer rows of holes are usually negligible proximity is often ignored in PhC cavity fabrication. This is can be problem in CORALs though because there is more then a single defect in the center of the structure but also the defects at outer part of the array.

One way to correct for proximity is to assign different doses to different parts of the structure by taking into account the forward and backward scattering of the beam using a so called self consistent dose correction scheme [96]. A commercial program at DANCHIP called "Layout Beamer" is able to do this with any pattern but requires a point spread function (PSF) that shows the energy distribution of the scattered electron beam.

The PSF of the electron beam can be calculated with another program called "Sceleton" which is a Monte Carlo simulator that calculates the spread of the scattered electrons in an arbitrary layer structure defined by the user. It also has a library that contains most of the scattering coefficients for the materials needed. In order to take the PSF into account Layout Beamer needs to fit the curve calculated by Sceleton using a multiple Gaussian model. It has been actually been shown that the PSF can be approximated better by using a combination of an exponential function and two gaussian functions [97].

The need for proximity correction depends strongly on the device but it should always be taken into account when planning to do an exposure. For many applications a careful adjustment of the dose is sufficient but one should be careful when working with nanophotonic structures since

small changes in feature sizes can have large effects when it comes to guiding or confining light. None of the structures presented in this thesis used proximity correction when they were exposed and the dose used to expose most patterns was around 200 μC per cm^2. It is planned though to routinely use proximity correction in the near future since it showed to have a quite pronounced effect on the structures presented here.

Appendix C

Recipes

GaAs optimized process

1. Deposit 200 nm Si_3N_4 on top of the sample in the PECVD as a hard mask.

2. Spin 500 nm ZEP520A on top of the sample as e-beam resist.

3. Expose the structures using the e-beam (Current: 0.8 nA current / Dose: $\sim$ 200 μC / Step size: 4-8 nm).

4. Develop the sample for 2 minutes in ZED N50 and rinse afterwards for 30 seconds in IPA. While developing gently stir the liquid by shaking it to make sure the pattern is developed fully.

5. Dry etch the sample in the Plassys for 16 minutes using the "Si3N4std" program to transfer the pattern from the e-beam resist into the hard mask (Gases: 16 sccm CHF_3/ 1 sccm O_2 / Power: 50 W to strike the plasma for 5 seconds and then 13 W / Pressure: 20 mTorr) . Use a full 2 inch GaAs Wafer as carrier. Lift-Off/Remove the ZEP by putting the sample for 2 hours into heated Microposit Remover 1165 with 20% Ultrasound at a temperature of around 65 degree Celsius. Make sure the sample is placed in the remover

with an tilt of larger than 90 degrees and the top surface pointing towards the bottom.

6. After removing the sample from the developer it is cleaned by shortly rinsing it with Acetone, Ethanol and IPA. Afterwards it is put for 2 minutes into the plasma asher.

7. Dry etch the sample for 8 cycles using the "cyc8" program (see recipe list for parameters) to transfer the pattern from the hard mask to the GaAs. The chamber needs to be cleaned for 30 minutes and preconditioned for 10 minutes prior to the etch using the "vlclean" program (Gases: 50 sccm O_2 / Power: 50 W / Pressure: 60 mTorr) and the "precond" program (Gases: 10 sccm CH_4/ 1 sccm H_2 / Power: 40 W / Pressure: 60 mTorr). Use a quarter of a 2" InP wafer as carrier

8. Remove the Si_3N_4 by dry etching the sample for 2 min in the Plassys using the "Si3N4des" program (Gases: 16 sccm CHF_3/ 1 sccm O_2 / Power: 20 W / Pressure: 60 mTorr).

9. Put the sample for 10 sec in 40% HF to release the membrane. Inspect the sample in the optical microscope to make sure it is fully membranized. A slight circular discoloration can be observed indicating a slight bending of the membrane.

InGaAsP optimized recipe

1. Deposit 200 nm Si_3N_4 on top of the sample in the PECVD as a hard mask.

2. Spin 500 nm ZEP520A on top of the sample as e-beam resist.

3. Expose the structures using the e-beam system (Current: 0.8 nA current / Dose: ~ 200 μC / Step size: 4-8 nm).

4. Develop the sample for 2 minutes in ZED N50 and rinse afterwards for 30 seconds in IPA. While developing gently stir the liquid by shaking it to make sure the pattern is developed fully.

5. Dry etch the sample in the Plassys for 16 minutes using the "Si3N4std" program to transfer the pattern from the e-beam resist into the hard mask. Use a full 2 inch GaAs Wafer as carrier (Gases: 16 sccm CHF_3/ 1 sccm O_2 / Power: 50 W to strike the plasma for 5 seconds and then 13 W / Pressure: 20 mTorr). Lift-Off/Remove the ZEP by putting the sample for 2 hours into heated Microposit Remover 1165 with 20% Ultrasound at a temperature of around 65 degree Celsius. Make sure the sample is placed in the remover with an tilt of larger than 90 degrees and the top surface pointing towards the bottom.

6. After removing the sample from the developer it is cleaned by shortly rinsing it with Acetone, Ethanol and IPA. Afterwards it is put for 2 minutes into the plasma asher.

7. Dry etch the sample for up to 16 cycles using the "cyc8" program (see recipe list for parameters) to transfer the pattern from the hard mask to the InGaAsP. The chamber needs to be cleaned for 30 minutes and preconditioned for 10 minutes prior to the etch using the "vlclean" program (Gases: 50 sccm O_2 / Power: 50 W / Pressure: 60 mTorr) and the "precond" program (Gases: 10 sccm CH_4/ 1 sccm H_2 / Power: 40 W / Pressure: 60 mTorr). Use a quarter of a 2" InP wafer as carrier.

8. Remove the Si_3N_4 by dry etching the sample for 2 min in the Plassys using the "Si3N4des" program (Gases: 16 sccm CHF_3/ 1 sccm O_2 / Power: 20 W / Pressure: 60 mTorr).

9. Put the sample for up to four times for 5 minutes in 1:1 ratio mixture of HCL/H_2O to release the membrane. In between each

step rinse the sample in water and put it for 2 minutes in 40% HF. Rinse again in water before putting it back into the HCL/H_2O mixture. Inspect the sample in the SEM to make sure it is fully membranized.

Complete recipe list for the GaAs etches

Recipe	Nr. cycles	Cycle length [min]	O2-D RF [W]	O2-D Flow [sccm]	O2-D p [mTorr]	O2-D time [min]	H2 [sccm]	CH4 [sccm]	pressure [mTorr]	power [W]	total Flow [sccm]	bias [V]	CH4 [%] of total Flow	sidewall [degree]	etch rate [nm/min]	Hole width (mask) [nm]	Mask thickness[nm]	carrier
cyc_a	8	2,5	20	50	150	0,5	30	1,5	15	40	31,5	453	5	107	2,9	128,0	100,0	full 2" GaAs
cyc_a	8	2,5	20	50	150	0,5	30	1,5	15	40	31,5	453	5	114	2,0	128,0	100,0	full 2" InP
cyc_b	8	2,5	60	50	100	1	30	1,5	15	40	31,5	460	5	-	0,7	128,0	100,0	full 2" GaAs
cyc_c	4	5	40	10	75	5	60	3	50	100	63	590	5	-	-	128,0	100,0	full 2" GaAs
cyc_d	8	5	20	50	150	0,5	60	3	50	100	63	584	5	110	3,6	128,0	100,0	full 2" GaAs
cyc_e	6	5	20	10	50	0,5	30	1	20	40	31	450	3	111	1,4	128,0	100,0	no carrier
cyc_f	6	5	20	10	50	0,5	30	3	20	40	33	450	10	101	-	201,0	100,0	1/4 2" InP
cyc_g	6	5	20	10	50	0,33	30	3	20	30	33	387	10	102	4,1	201,0	100,0	1/4 2" InP
cyc_h	2	10	20	50	150	0,5	67,2	8,4	60	70	75,6	470	13	-	-	197-140	200,0	1/4 2" InP
cyc_i	3	5	20	10	50	0,5	30	2,2	20	60	32,2	550	7	109	-	201,0	100,0	1/4 2" InP
cyc_j	3	5	20	10	50	0,5	30	3,8	20	40	33,8	450	13	96	7,5	201,0	100,0	1/4 2" InP
cyc_k	3	5	20	10	50	0,5	30	4,5	20	40	34,5	450	15	97	8,3	201,0	100,0	1/4 2" InP
cyc_k	3	5	20	10	50	0,5	30	4,5	20	40	34,5	450	15	96	6,1	197-140	200,0	1/4 2" InP
cyc_l	6	2,5	20	10	50	0,5	30	4,5	20	40	34,5	450	15	96	5,1	197-140	200,0	1/4 2" InP
cyc_m	3	5	20	10	50	0,5	30	5,3	20	40	35,3	450	18	96	9,1	201,0	100,0	1/4 2" InP
cyc_n	3	5	20	10	50	0,5	30	6	20	40	36	450	20	96	9,3	201,0	100,0	1/4 2" InP
cyc_o	3	5	20	10	50	0,5	30	7,5	20	40	37,5	450	25	96	9,8	201,0	100,0	1/4 2" InP
cyc_p	3	5	20	10	50	0,5	30	2,2	20	40	32,2	450	7	98	5,2	201,0	100,0	1/4 2" InP
cyc12_u.prg	12	2,5	20	50	150	0,5	67,2	10	80	60	77,2	435	15	100	7,0	128,0	100,0	full 2" InP
cyc24_75.prg	24	1,25	20	50	150	0,5	67,2	8,4	80	60	75,6	435	13	104	3,5	128,0	100,0	full 2" InP
cyc7_lp.prg	7	2,5	20	50	150	0,5	33,6	4,2	20	60	37,8	555	13	102	6,6	128,0	100,0	full 2" InP
cyc7_lrf.prg	7	2,5	20	50	150	0,5	67,2	8,4	80	40	75,6	349	13	93	8,7	197-140	200,0	1/4 2" InP
cyc7_lrf.prg	7	2,5	20	50	150	0,5	67,2	8,4	80	40	75,6	350	13	98	4,7	128,0	100,0	full 2" InP
cyc7a	6	3	20	50	150	0,5	67,2	8,4	80	60	75,6	430	13	97	8,8	197-140	200,0	1/4 2" InP
cyc7b	9	2	20	50	150	0,5	67,2	8,4	80	60	75,6	430	13		7,2	197-140	200,0	1/4 2" InP
cyc8.prg	8	2,5	20	50	150	0,5	67,2	8,4	80	60	75,6	437	13	95	8,9	128,0	100,0	1/4 2" InP
cyc8.prg	8	2,5	20	50	150	0,5	67,2	8,4	80	60	75,6	430	13	92	-	197-140	200,0	1/4 2" InP
cyc8.prg	8	2,5	20	50	150	0,5	67,2	8,4	80	60	75,6	440	13	100	7,5	128,0	100,0	full 2" InP

Figure C.1: Etch results were measured by SEM inspection. Samples were cleaved prior to inspection. All patterns inspected were bulk PhCs.

Appendix D

Abbreviation

Abbreviation	Explanation
AlGaAs	aluminum gallium arsenide
Ar	argon
BCl_3	boron trichlorine
CAIBE	chemical assisted ion beam etching
CH_4	methane
CHF_3	freon
CH_3	methyl
Cl_2	chlorine
CORAL	coupled photonic crystal array laser
CROW	coupled optical resonator waveguide
DI	deionized water
DFB	distributed feedback
ECR	electron cyclotron resonance
F	Purcell enhancement factor
fcc	face centered cubic
FTDT	finite difference time domain
H_2	hydrogen
HCl	hydrochloric acid

IAD	angular distribution of the ions
ICP	inductively coupled plasma
IED	energy distribution of the ions
InAlAs	indium aluminum arsenide
InP	indium phosphide
GaAs	gallium arsenide
H_2	Hydrogen
InGaAs	indium gallium arsenide
InGaAsP	indium gallium arsenide phosphide
LL	light-in-light-out
MEEP	MIT Electromagnetic Equation Propagation
MPB	Massachusetts Institute of Technology bandgap package
MBE	molecular beam epitaxy
MOVPE	metal organic phase vapor epitaxy
MORIE	metal organic reactive ion etch
NATEC	Nanophotonics for Terabit Communications
O_2	Oxgyen
PhC	photonic crystal
PSF	point spread function
Q	Quality factor
QD	quantum dot
QW	quantum well
RIBE	reactive ion beam etcher
RIE	reactive ion etch or reactive ion etcher
scc	simple cubic lattic
Si	silicon
Si_3N_4	silicon nitride
SiO_2	silicon dioxide
SK	Stranski-Krastanov
TE	transverse electric
TIR	total internal reflection

| TM | transverse magnetic |
| VCSEL | vertical cavity surface emitting lasers |

Bibliography

[1] H. Altug and J. Vuckovic, "Photonic crystal nanocavity array laser," *Opt. Express*, vol. 13, no. 22, pp. 8819–8828, 2005.

[2] H. Altug, D. Englund, and J. Vuckovic, "Ultrafast photonic crystal nanocavity laser," *Nat Phys*, vol. 2, pp. 484–488, July 2006.

[3] H. Altug and J. Vuckovic, "Two-dimensional coupled photonic crystal resonator arrays," *Applied Physics Letters*, vol. 84, no. 2, pp. 161–163, 2004.

[4] E. Yablonovitch, "Inhibited spontaneous emission in solid-state physics and electronics," *Phys. Rev. Lett.*, vol. 58, pp. 2059–2062, May 1987.

[5] S. John, "Strong localization of photons in certain disordered dielectric superlattices," *Phys. Rev. Lett.*, vol. 58, pp. 2486–2489, Jun 1987.

[6] J. D. Joannopoulos, S. G. Johnson, J. N. Winn, and R. D. Meade, *Molding the flow of light (2nd edition)*. Princeton University Press, 2008.

[7] E. Yablonovitch, T. J. Gmitter, and K. M. Leung, "Photonic band structure: The face-centered-cubic case employing nonspherical atoms," *Phys. Rev. Lett.*, vol. 67, pp. 2295–2298, Oct 1991.

[8] T. F. Krauss, R. M. D. L. Rue, and S. Brand, "Two-dimensional photonic-bandgap structures operating at near-infrared wavelengths," *Nature*, vol. 383, pp. 699–702, Oct. 1996.

[9] S. G. Johnson, S. Fan, P. R. Villeneuve, J. D. Joannopoulos, and L. A. Kolodziejski, "Guided modes in photonic crystal slabs," *Phys. Rev. B*, vol. 60, pp. 5751–5758, Aug 1999.

[10] P. R. Villeneuve, S. Fan, and J. D. Joannopoulos, "Microcavities in photonic crystals: Mode symmetry, tunability, and coupling efficiency," *Phys. Rev. B*, vol. 54, pp. 7837–7842, Sep 1996.

[11] S. Noda, M. Fujita, and T. Asano, "Spontaneous-emission control by photonic crystals and nanocavities," *Nat Photon*, vol. 1, pp. 449–458, Aug. 2007.

[12] P. Lodahl, A. Floris van Driel, I. S. Nikolaev, A. Irman, K. Overgaag, D. Vanmaekelbergh, and W. L. Vos, "Controlling the dynamics of spontaneous emission from quantum dots by photonic crystals," *Nature*, vol. 430, pp. 654–657, Aug. 2004.

[13] E. Purcell, "Spontaneous emission probabilities at radio frequencies," *Physical Review*, vol. 69, no. 11-1, p. 681, 1946.

[14] M. Lipson, "Guiding, modulating, and emitting light on silicon-challenges and opportunities," *J. Lightwave Technol.*, vol. 23, no. 12, p. 4222, 2005.

[15] H.-G. Park, S.-H. Kim, S.-H. Kwon, Y.-G. Ju, J.-K. Yang, J.-H. Baek, S.-B. Kim, and Y.-H. Lee, "Electrically driven single-cell photonic crystal laser," *Science*, vol. 305, no. 5689, pp. 1444–1447, 2004.

[16] A. Berrier, M. Mulot, G. Malm, M. Ostling, and S. Anand, "Carrier transport through a dry-etched inp-based two-dimensional photonic crystal," *Journal of Applied Physics*, vol. 101, no. 12, p. 123101, 2007.

[17] B. Ellis, T. Sarmiento, M. Mayer, B. Zhang, J. Harris, E. Haller, and J. Vuckovic, "Electrically pumped photonic crystal nanocavity light sources using a laterally doped p-i-n junction," *Applied Physics Letters*, vol. 96, no. 18, p. 181103, 2010.

[18] T. Asano, B.-S. Song, and S. Noda, "Analysis of the experimental q factors (1 million) of photonic crystal nanocavities," *Opt. Express*, vol. 14, no. 5, pp. 1996–2002, 2006.

[19] S. Strauf, K. Hennessy, M. T. Rakher, Y.-S. Choi, A. Badolato, L. C. Andreani, E. L. Hu, P. M. Petroff, and D. Bouwmeester, "Self-tuned quantum dot gain in photonic crystal lasers," *Physical Review Letters*, vol. 96, p. 127404, Mar 2006.

[20] R. Herrmann, T. Sünner, T. Hein, A. Löffler, M. Kamp, and A. Forchel, "Ultrahigh-quality photonic crystal cavity in gaas," *Opt. Lett.*, vol. 31, no. 9, pp. 1229–1231, 2006.

[21] C. Kittel, *Introduction to Solid State Physics (8th edition)*. John Wiley & Sons;, 2004.

[22] S. G. Johnson and J. D. Joannopoulos, "Block-iterative frequency-domain methods for maxwell's equations in a planewave basis," *Opt. Express*, vol. 8, no. 3, pp. 173–190, 2001.

[23] J. D. Jackson, *Classical Electrodynamics*. Wiley, 1998.

[24] J. Vukovic, M. Loncar, H. Mabuchi, and A. Scherer, "Design of photonic crystal microcavities for cavity qed," *Phys. Rev. E*, vol. 65, p. 016608, Dec 2001.

[25] A. D. Bristow, J.-P. R. Wells, W. H. Fan, A. M. Fox, M. S. Skolnick, D. M. Whittaker, A. Tahraoui, T. F. Krauss, and J. S. Roberts, "Ultrafast nonlinear response of algaas two-dimensional photonic crystal waveguides," *Applied Physics Letters*, vol. 83, no. 5, pp. 851–853, 2003.

[26] Y. Akahane, T. Asano, B.-S. Song, and S. Noda, "High-q photonic nanocavity in a two-dimensional photonic crystal," *Nature*, vol. 425, pp. 944–947, Oct. 2003.

[27] A. F. Oskooi, D. Roundy, M. Ibanescu, P. Bermel, J. D. Joannopoulos, and S. G. Johnson, "Meep: A flexible free-software package for electromagnetic simulations by the FDTD method," *Computer Physics Communications*, vol. 181, pp. 687–702, January 2010.

[28] J. Scheuer, W. M. J. Green, G. A. DeRose, and A. Yariv, "Lasing from a circular bragg nanocavity with an ultrasmall modal volume," *Applied Physics Letters*, vol. 86, no. 25, p. 251101, 2005.

[29] C. Husko, A. D. Rossi, S. Combrie, Q. V. Tran, F. Raineri, and C. W. Wong, "Ultrafast all-optical modulation in gaas photonic crystal cavities," *Applied Physics Letters*, vol. 94, no. 2, p. 021111, 2009.

[30] A. Yariv, Y. Xu, R. K. Lee, and A. Scherer, "Coupled-resonator optical waveguide: a proposal and analysis," *Opt. Lett.*, vol. 24, no. 11, pp. 711–713, 1999.

[31] J. K. S. Poon, J. Scheuer, Y. Xu, and A. Yariv, "Designing coupled-resonator optical waveguide delay lines," *J. Opt. Soc. Am. B*, vol. 21, no. 9, pp. 1665–1673, 2004.

[32] K. A. Atlasov, K. F. Karlsson, A. Rudra, B. Dwir, and E. Kapon, "Wavelength and loss splitting in directly coupled photonic-crystal defect microcavities," *Opt. Express*, vol. 16, no. 20, pp. 16255–16264, 2008.

[33] H. Altug, *Physics and Applications of Photonic Crystal nanocavities*. PhD thesis, Stanford University, 2006.

[34] L. A. Coldren and S. Corzine, *Diode Lasers and Photonic Integrated Circuitsff*. Wiley-Interscience, 1995.

[35] A. Adams, G. Björk, H. J. E. Bowers, I. Heitmann, J. Inoue, E. Kapon, F. Matinga, R. Nagarajan, E. P. O'Reilly, M. Silver, A. Yariv, Y. Yumamoto, and B. Zhao, *Semiconductor Lasers I.* Academic Press, 1999.

[36] V. M. Ustinov, *Qunatum Dot Lasers.* Oxford University Press, 2003.

[37] O. Painter, R. K. Lee, A. Scherer, A. Yariv, J. D. O'Brien, P. D. Dapkus, and I. Kim, "Two-dimensional photonic band-gap defect mode laser," *Science*, vol. 284, no. 5421, pp. 1819–1821, 1999.

[38] M. Loncar, T. Yoshie, A. Scherer, P. Gogna, and Y. Qiu, "Low-threshold photonic crystal laser," *Applied Physics Letters*, vol. 81, no. 15, pp. 2680–2682, 2002.

[39] H. G. Park, J. K. Hwang, J. Huh, H. Y. Ryu, S. H. Kim, J. S. Kim, and Y. H. Lee, "Characteristics of modified single-defect two-dimensional photonic crystal lasers," *IEEE Journal of Quantum Electronics*, vol. 38, pp. 1353–1365, oct 2002.

[40] K. Nozaki and T. Baba, "Laser characteristics with ultimate-small modal volume in photonic crystal slab point-shift nanolasers," *Applied Physics Letters*, vol. 88, no. 21, p. 211101, 2006.

[41] M. Nomura, K. Tanabe, S. Iwamoto, and Y. Arakawa, "High-q design of semiconductor-based ultrasmall photonic crystal nanocavity," *Optics Express*, vol. 18, no. 8, pp. 8144–8150, 2010.

[42] C. Gies, J. Wiersig, and F. Jahnke, "Output characteristics of pulsed and continuous-wave-excited quantum-dot microcavity lasers," *Phys. Rev. Lett.*, vol. 101, p. 067401, Aug 2008.

[43] T. Suhr, N. Gregersen, K. Yvind, and J. Mørk, "Modulation response of nanoleds and nanolasers exploiting purcell enhanced spontaneous emission," *Opt. Express*, vol. 18, no. 11, pp. 11230–11241, 2010.

[44] E. K. Lau, A. Lakhani, R. S. Tucker, and M. C. Wu, "Enhanced modulation bandwidth of nanocavity light emitting devices," *Opt. Express*, vol. 17, no. 10, pp. 7790–7799, 2009.

[45] T. Yoshie, M. Loncar, A. Scherer, and Y. Qiu, "High frequency oscillation in photonic crystal nanolasers," *Applied Physics Letters*, vol. 84, no. 18, pp. 3543–3545, 2004.

[46] P. Blood, "On the dimensionality of optical absorption, gain, and recombination in quantum-confined structures," *Quantum Electronics, IEEE Journal of*, vol. 36, pp. 354 –362, mar. 2000.

[47] A. Matsutani, H. Ohtsuki, F. Koyama, and K. Iga, "Vertical and smooth etching of inp by cl-2/xe inductively coupled plasma," *Japanese Journal of Applied Physics Part 1-Regular Papers Short Notes & Review Papers*, vol. 38, pp. 4260–4261, JUL 1999.

[48] F. Pommereau, L. Legouezigou, S. Hubert, S. Sainson, J. P. Chandouineau, S. Fabre, G. H. Duan, B. Lombardet, R. Ferrini, and R. Houdre, "Fabrication of low loss two-dimensional inp photonic crystals by inductively coupled plasma etching," *Journal of Applied Physics*, vol. 95, pp. 2242–2245, Mar. 2004.

[49] P. Strasser, R. Wuest, F. Robin, D. Erni, and H. Jackel, "Detailed analysis of the influence of an inductively coupled plasma reactive-ion etching process on the hole depth and shape of photonic crystals in inp/ingaasp," *Journal of Vacuum Science Technology B: Microelectronics and Nanometer Structures*, vol. 25, pp. 387 –393, mar 2007.

[50] D. L. Flamm, V. M. Donnelly, and D. E. Ibbotson, "Basic chemistry and mechanisms of plasma etching," *Journal of Vacuum Science & Technology B: Microelectronics and Nanometer Structures*, vol. 1, no. 1, pp. 23–30, 1983.

[51] T. R. Hayes, M. A. Dreisbach, P. M. Thomas, W. C. Dautremont-Smith, and L. A. Heimbrook, "Reactive ion etching of inp using ch[sub 4]/h[sub 2] mixtures: Mechanisms of etching and anisotropy," *Journal of Vacuum Science & Technology B: Microelectronics and Nanometer Structures*, vol. 7, no. 5, pp. 1130–1140, 1989.

[52] J. Liu, G. L. Huppert, and H. H. Sawin, "Ion bombardment in rf plasmas," *Journal of Applied Physics*, vol. 68, pp. 3916 –3934, oct 1990.

[53] S. C. McNevin, "Chemical etching of gaas and inp by chlorine: The thermodynamically predicted dependence on cl[sub 2] pressure and temperature," *Journal of Vacuum Science & Technology B: Microelectronics and Nanometer Structures*, vol. 4, no. 5, pp. 1216–1226, 1986.

[54] N. Ikeda, Y. Sugimoto, Y. Tanaka, K. Inoue, H. Oda, Y. Watanabe, and K. Asakawa, "Studies on key nano-fabrication processes for gaas-based air-bridge-type two-dimensional photonic-crystal slab waveguides," *Semiconductor Science and Technology*, vol. 22, pp. 149–157, Feb. 2007.

[55] M. Mulot, S. Anand, C. F. Carlström, M. Swillo, and A. Talneau, "Dry etching of photonic crystals in inp based materials," *Physica Scripta*, vol. 2002, no. T101, p. 106, 2002.

[56] U. Niggebrugge, M. Klug, and G. Garus, "A novel process for reactive ion etching on inp, using ch4/h2," in *Gallium arsenide and related compounds 1985. Proceedings*, no. 79, pp. 367–372, International Symposium on Gallium Arsenide and Related Compounds 12, 1985, Karuizawa, Institute of Physics - Conference Series, 1985.

[57] Y. Feurprier, C. Cardinaud, and G. Turban, "Surface modification and etch product detection during reactive ion etching of inp in

ch[sub 4]-h[sub 2] plasma," *Plasma Sources Science and Technology*, vol. 6, no. 3, p. 334, 1997.

[58] Y. Feurprier, C. Cardinaud, B. Grolleau, and G. Turban, "Proposal for an etching mechanism of inp in ch[sub 4]-h[sub 2] mixtures based on plasma diagnostics and surface analysis," *Journal of Vacuum Science & Technology A*, vol. 16, no. 3, pp. 1552–1559, 1998.

[59] A. Carter, B. Thomas, D. Morgan, J. Bhardwaj, A. McQuarrie, and M. Stephens, "Dry etching of gaas and inp for optoelectronic devices," *Optoelectronics, IEE Proceedings J*, vol. 136, pp. 2 –5, feb 1989.

[60] R. Cheung, S. Thoms, S. Beamont, G. Doughty, V. Law, and C. Wilkinson, "Reactive ion etching of gaas using a mixture of methane and hydrogen," *Electronics Letters*, vol. 23, no. 16, pp. 857–859, 1987.

[61] D. Larsson, *Fabrication and Characterisation of Low-noise Monolithic Mode-locked Lasers.* PhD thesis, Technical University of Denmark COM DTU, 2007.

[62] N. A. Morrison, C. William, and W. I. Milne, "Methane chemistry involved in a low-pressure electron cyclotron wave resonant plasma discharge," *Journal of Applied Physics*, vol. 94, no. 11, pp. 7031–7043, 2003.

[63] L. Henry and P. Granjoux, "Novel process for integration of optoelectronic devices using reactive ion etching without chlorinated gas," *Electronics Letters*, vol. 23, no. 24, pp. 1253–1253, 1987.

[64] D. Gerace and L. C. Andreani, "Disorder-induced losses in photonic crystal waveguides with line defects," *Opt. Lett.*, vol. 29, no. 16, pp. 1897–1899, 2004.

[65] A. Xing, M. Davanco, D. J. Blumenthal, and E. L. Hu, "Fabrication of inp-based two-dimensional photonic crystal membrane," *Journal of Vacuum Science & Technology B: Microelectronics and Nanometer Structures*, vol. 22, no. 1, pp. 70–73, 2004.

[66] Y. Tanaka, T. Asano, Y. Akahane, B.-S. Song, and S. Noda, "Theoretical investigation of a two-dimensional photonic crystal slab with truncated cone air holes," *Applied Physics Letters*, vol. 82, no. 11, pp. 1661–1663, 2003.

[67] D. Keil and E. Anderson, "Characterization of reactive ion etch lag scaling," *Journal of Vacuum Science & Technology B: Microelectronics and Nanometer Structures*, vol. 19, no. 6, pp. 2082–2088, 2001.

[68] A. Berrier, M. Mulot, S. Anand, A. Talneau, R. Ferrini, and R. Houdre, "Characterization of the feature-size dependence in ar/cl[sub 2] chemically assisted ion beam etching of inp-based photonic crystal devices," *Journal of Vacuum Science & Technology B: Microelectronics and Nanometer Structures*, vol. 25, no. 1, pp. 1–10, 2007.

[69] S. Anantathanasarn, Y. Barbarin, N. I. Cade, P. J. van Veldhoven, E. A. J. M. Bente, Y. S. Oei, H. Kamada, M. K. Smit, and R. Notzel, "Wavelength tunable inas/inp(100) quantum dots in 1.55-mu m telecom devices," *MATERIALS SCIENCE AND ENGINEERING B-SOLID STATE MATERIALS FOR ADVANCED TECHNOLOGY*, vol. 147, no. 2-3, month = FEB 15, note = Symposium on Semiconductor Nanostructures towards Electronic and Optoelectronic Device Applications held at the 2007 EMRS Spring Meeting, Strasbourg, FRANCE, MAY 28-JUN 01, 2007, pp. 124–130, 2008.

[70] K. Kawaguchi, M. Ekawa, A. Kuramata, T. Akiyama, H. Ebe, M. Sugawara, and Y. Arakawa, "Fabrication of inas quantum dots

on inp(100) by metalorganic vapor-phase epitaxy for 1.55 mu m optical device applications," *Applied Physics Letters*, vol. 85, no. 19, pp. 4331–4333, 2004.

[71] S. Stobbe, J. Johansen, P. T. Kristensen, J. M. Hvam, and P. Lodahl, "Frequency dependence of the radiative decay rate of excitons in self-assembled quantum dots: Experiment and theory," *Phys. Rev. B*, vol. 80, p. 155307, Oct 2009.

[72] C. Gatzert, A. W. Blakers, P. N. K. Deenapanray, D. Macdonald, and F. D. Auret, "Investigation of reactive ion etching of dielectrics and si in chf[sub 3]/o[sub 2] or chf[sub 3]/ar for photovoltaic applications," *Journal of Vacuum Science & Technology A: Vacuum, Surfaces, and Films*, vol. 24, no. 5, pp. 1857–1865, 2006.

[73] L. H. Frandsen, *Fabrication and Characterization of Photonic Bandgap Components*. PhD thesis, Technical University of Denmark COM DTU, 2007.

[74] E. Yablonovitch, T. Gmitter, J. P. Harbison, and R. Bhat, "Extreme selectivity in the lift-off of epitaxial gaas films," *Applied Physics Letters*, vol. 51, no. 26, pp. 2222–2224, 1987.

[75] U. K. Khankhoje, S.-H. Kim, B. C. Richards, J. Hendrickson, J. Sweet, J. D. Olitzky, G. Khitrova, H. M. Gibbs, and A. Scherer, "Modelling and fabrication of gaas photonic-crystal cavities for cavity quantum electrodynamics," *Nanotechnology*, vol. 21, no. 6, p. 065202, 2010.

[76] J.-K. Hwang, H.-Y. Ryu, D.-S. Song, I.-Y. Han, H.-W. Song, H.-K. Park, Y.-H. Lee, and D.-H. Jang, "Room-temperature triangular-lattice two-dimensional photonic band gap lasers operating at 1.54 mu m," *Applied Physics Letters*, vol. 76, no. 21, pp. 2982–2984, 2000.

[77] S. Adachi and H. Kawaguchi, "Chemical etching characteristics of (001)inp," *Journal of The Electrochemical Society*, vol. 128, no. 6, pp. 1342–1349, 1981.

[78] K. Srinivasan, P. E. Barclay, O. Painter, J. X. Chen, and A. Y. Cho, "Fabrication of high-quality-factor photonic crystal microcavities in inasp/ingaasp membranes," *Journal of Vacuum Science & Technology B*, vol. 22, pp. 875–879, May 2004.

[79] J. R. Cao, P.-T. Lee, S.-J. Choi, R. Shafiiha, S.-J. Choi, J. D. O'Brien, and P. D. Dapkus, "Nanofabrication of photonic crystal membrane lasers," *Journal of Vacuum Science & Technology B: Microelectronics and Nanometer Structures*, vol. 20, no. 2, pp. 618–621, 2002.

[80] C. Seassal, J. L. Leclercq, and P. Viktorovitch, "Fabrication of inp-based freestanding microstructures by selective surface micromachining," *Journal of Micromechanics and Microengineering*, vol. 6, no. 2, p. 261, 1996.

[81] R. Heitz, M. Veit, N. N. Ledentsov, A. Hoffmann, D. Bimberg, V. M. Ustinov, P. S. Kop'ev, and Z. I. Alferov, "Energy relaxation by multiphonon processes in inas/gaas quantum dots," *Phys. Rev. B*, vol. 56, pp. 10435–10445, Oct 1997.

[82] A. Naesby, T. Suhr, P. T. Kristensen, and J. Mork, "Influence of pure dephasing on emission spectra from single photon sources," *Physical Review A*, vol. 78, p. 045802, Oct. 2008.

[83] M. Winger, T. Volz, G. Tarel, S. Portolan, A. Badolato, K. J. Hennessy, E. L. Hu, A. Beveratos, J. Finley, V. Savona, and A. m. c. Imamoğlu, "Explanation of photon correlations in the far-off-resonance optical emission from a quantum-dot–cavity system," *Phys. Rev. Lett.*, vol. 103, p. 207403, Nov 2009.

[84] T. L. Hansen, *Time-Resolved Spectroscopy of Qunatum Dot Single-Photon sources.* PhD thesis, Technical University of Denmark DTU FOTONIK, 2009.

[85] Z. Y. Xu, Z. D. Lu, X. P. Yang, Z. L. Yuan, B. Z. Zheng, J. Z. Xu, W. K. Ge, Y. Wang, J. Wang, and L. L. Chang, "Carrier relaxation and thermal activation of localized excitons in self-organized inas multilayers grown on gaas substrates," *Phys. Rev. B*, vol. 54, pp. 11528–11531, Oct 1996.

[86] B. Wild, R. Ferrini, R. Houdre, M. Mulot, S. Anand, and C. J. M. Smith, "Temperature tuning of the optical properties of planar photonic crystal microcavities," *Applied Physics Letters*, vol. 84, no. 6, pp. 846–848, 2004.

[87] M. Notomi, E. Kuramochi, and T. Tanabe, "Large-scale arrays of ultrahigh-q coupled nanocavities," *Nat Photon*, vol. 2, pp. 741–747, Dec. 2008.

[88] S. Ishii, K. Nozaki, and T. Baba, "Photonic molecules in photonic crystals," *Japanese Journal of Applied Physics*, vol. 45, no. 8A, pp. 6108–6111, 2006.

[89] M. Bayer, T. Gutbrod, J. P. Reithmaier, A. Forchel, T. L. Reinecke, P. A. Knipp, A. A. Dremin, and V. D. Kulakovskii, "Optical modes in photonic molecules," *Phys. Rev. Lett.*, vol. 81, pp. 2582–2585, Sep 1998.

[90] R. Braive, S. Barbay, I. Sagnes, A. Miard, I. Robert-Philip, and A. Beveratos, "Transient chirp in high-speed photonic-crystal quantum-dot lasers with controlled spontaneous emission," *Opt. Lett.*, vol. 34, no. 5, pp. 554–556, 2009.

[91] U. Mohideen, R. E. Slusher, F. Jahnke, and S. W. Koch, "Semi-

conductor microlaser linewidths," *Physical Review Letters*, vol. 73, pp. 1785–1788, Sept. 1994.

[92] J. Hendrickson, B. C. Richards, J. Sweet, S. Mosor, C. Christenson, D. Lam, G. Khitrova, H. M. Gibbs, T. Yoshie, A. Scherer, O. B. Shchekin, and D. G. Deppe, "Quantum dot photonic-crystal-slab nanocavities: Quality factors and lasing," *Physical Review B*, vol. 72, p. 193303, nov 2005.

[93] S.-H. Kwon, H.-Y. Ryu, G.-H. Kim, Y.-H. Lee, and S.-B. Kim, "Photonic bandedge lasers in two-dimensional square-lattice photonic crystal slabs," *Applied Physics Letters*, vol. 83, no. 19, pp. 3870–3872, 2003.

[94] M. Nomura, S. Iwamoto, A. Tandaechanurat, Y. Ota, N. Kumagai, and Y. Arakawa, "Photonic band-edge micro lasers with quantum dot gain," *Opt. Express*, vol. 17, no. 2, pp. 640–648, 2009.

[95] T. H. P. Chang, "Proximity effect in electron-beam lithography," *Journal of Vacuum Science and Technology*, vol. 12, no. 6, pp. 1271–1275, 1975.

[96] S.-Y. Lee and B. Cook, "Pyramid-a hierarchical, rule-based approach toward proximity effect correction. i. exposure estimation," *Semiconductor Manufacturing, IEEE Transactions on*, vol. 11, pp. 108 –116, feb. 1998.

[97] F. Koba, H. Yamashita, and H. Arimoto, "Highly accurate proximity effect correction for 100 kv electron projection lithography," *Japanese Journal of Applied Physics*, vol. 44, no. 7B, pp. 5590–5594, 2005.